DEFORMATION AND FAILURE OF ROCK

Kelvis del Carmen Pérez Hidalgo

DEFORMATION AND FAILURE OF ROCK

Deformations- och brottsprocessen i berg

Kelvis del Carmen Pérez Hidalgo,
Luleå University of Technology

FÖRORD

I samband med dimensionering och utförande av berganläggningar i såväl gruvor som infrastrukturprojekt är stabiliteten central. I de stabilitetsanalyser som utförs är det av avgörande betydelse att förstå brottmekanismer och olika stadier i brottsprocessen, d v s initiering av brott, uppsprickning och slutligen utfall. Vid användning av numeriska analyser behöver deformationer för de olika stadierna kvantifieras. Det gäller också vid tillämpning av Eurokoden och observationsmetoden eftersom den baseras på att mäta bergkonstruktionens beteende, vilket enklast sker med deformationsmätningar.

I föreliggande arbete studeras förhållandet mellan bergmassans deformation och initieringen av brott på randen av en underjordsöppning. Som underlag till forskningen har information från laboratorietester, bergkonstruktioner under jord och numeriska analyser använts. Fältdata har hämtats från olika brottfall i gruvor, nämligen spjälkbrott i Garpenbergsgruvan och Zinkgruvan, böj- och skjuvbrott i Kristinebergsgruvan, samt kilbrott i Kiirunavaaragruvan. Resultatet av forskningen visar på skillnader i hur brottsprocesserna för de olika fallen utvecklas. Avslutningsvis redovisas olika metoder för att detektera brott och identifiera de olika brottstyperna; spjälk-, böj-, skjuv- och kilbrott.

Detta doktorsarbete är en fortsättning på ett forskningsarbete som resulterade i en licentiatexamen. Forskningsprojektet är ett av tre inom området "Dimensionering av samverkanskonstruktioner", där de två övriga projekten studerat karaktärisering av berg och tillförlitlighet i undersökningar av bergegenskaper respektive analys av blockstabilitet med deterministiska och probabilistiska metoder.

Doktorandarbetet utfördes av Kelvis de Carmen Pérez Hidalgo vid Luleå Tekniska Universitet under ledning av professor Erling Nordlund och adj. professor Johnny Sjöberg. Den referensgrupp som bistått utredarna och bidragit med värdefullt stöd har bestått av Beatrice Lindström (f d Golder Associates nu Trafikverket), Mats Holmberg (Tunnel Engineering), Rolf Christiansson (SKB), Anders Fredriksson (Golder Associates nu Sweco/egen konsult), Olle Olofsson och Thomas Dalmalm (Trafikverket), Jimmy Töyrä (f d Trafikverket nu LKAB), Mehdi Bagheri (f d KTH nu Golder Associates), Lars O Ericsson och Miriam Zetterlund (Chalmers), och Tomas Franzén och Mikael Hellsten (BeFo). Doktorsarbetet finansierades av Stiftelsen Bergteknisk Forskning, BeFo, tillsammans med Trafikverket, SKB, Vinnova och CAMM (the Centre of Advanced Mining & Metallurgy vid LTU).

Stockholm i december 2013
Per Tengborg

PREFACE

When designing and constructing facilities in rock, both in mines and for infrastructural projects, the stability is vital. For stability analyses it is important to understand the failure mechanisms and different phases in the process of failure, i.e failure initiation, fracturing and finally fallout. When utilizing numerical analyses the different phases need to be quantified. This is also the case when applying Eurocode and the observational method since it is based on the behavior of the rock structure, often best detected and measured by deformation.
In this work the relation of rock mass deformation and initiation of failure at the perimeter of an underground opening was studied. The base for this research comprised of information from; laboratory tests, underground rock facilities, and numerical methods. Field data from different failures in mines were collected from; spalling in the Garpenberg mine and Zinkgruvan, bending and shear failure in the Kristineberg mine, and shear failure in the Kiirunavaara mine.
This research work concluded differences in how the failure mechanisms develop. And finally, how to detect failure and monitor deformations for the different types of failure, i.e. spalling, bending, shear, and wedge.
This PhD work is a continuation of previous work that resulted in a licentiate exam. The research project is one out of three within the field "Design of composite structures", where one project studied rock characterization and reliability in investigations and the other block stability analysis using deterministic and probabilistic methods.
This PhD work was performed by Kelvis de Carmen Pérez Hidalgo at Luleå University of Technology under the supervision of Professor Erling Nordlund and Adjunct Professor Jonny Sjöberg. A reference group assisted the project and was composed of Beatrice Lindström (formerly Golder Associates now Trafikverket), Mats Holmberg (Tunnel Engineering), Rolf Christiansson (SKB), Anders Fredriksson (formerly Golder Associates now Sweco/independent consultant), Olle Olofsson and Thomas Dalmalm (Trafikverket), Jimmy Töyrä (formerly Trafikverket now LKAB), Mehdi Bagheri (formerly KTH now Golder Associates), Lars O Ericsson and Miriam Zetterlund (Chalmers University of Technology), and Tomas Franzén and Mikael Hellsten (BeFo). This PhD work was financially supported by the Rock Engineering Research Foundation, BeFo, together with Trafikverket (Swedish Transport Administration), SKB, Vinnova and CAMM (the Centre of Advanced Mining & Metallurgy at Luleå University of Technology).

Stockholm in December 2013
Per Tengborg

ACKNOWLEDGEMENT

iv

SAMMANFATTNING

I denna doktorsavhandling har relationen mellan bergmassans deformation och initieringen av brott på randen av en underjordsöppning studerats. Brottsobservationer och uppmätta deformationer har använts som indata. Arbetet har baserats på information från laboratorietester, bergkonstruktioner under jord och numeriska analyser. Fältdata har använts som indata till de numeriska analyserna.

De verkliga fall som studerats har bidragit med information som har gjort det möjligt att studera deformationerna under brottutvecklingen. Specifikt bidrog fallen med information om (i) Spjälkbrott genom numeriska analyser av ett schakt i Garpenbergsgruvan samt en undersökningsort i Zinkgruvan, (ii) Böj- respektive skjuvbrott genom utvärdering och analys av deformationer och brottsobservationer i ett brytningsrum i Kristinebergsgruvan och (iii) Kilbrott genom utvärdering och analys av en kils rörelser i Kiirunavaaragruvan.

Brotts- och deformationsprocessen analyserades för femton testade bergarter. Kornstorlekens och mineralinnehållets påverkan på ett antal olika töjningsstorheter i de testade provkopparna studerades. Studierna visade att kornstorleken hade en mycket stor inverkan på den laterala töjningens värde vid stadiet "crack damage" (ofta definierad som bergartens flytgräns). Mineralinnehållet hade en viss inverkan på de studerade töjningsstorheterna.

Jämförelser av töjningsstorheter beräknade för schaktet i Garpenbergsgruvan samt för undersökningsorten in Zinkgruvan med uppmätta och utvärderade data från laboratorietester (kalksten respektive kvartsit) ökade förståelsen och bidrog till att brottsprocessen i dessa båda fall kunde förklaras. De beräknade töjningskoncentrationerna som var närmast randen av öppningarna sammanföll ungefär med de observerade utfallens lägen.

Genom att studera väggarnas och takets deformationsmönster samt analyser av borrhålsinformation och skadekartering i ett brytningsrum i Kristinebergsgruvan kunde böj- och skjuvbrott identifieras i hängvägg respektive liggvägg. Skjuvbrottet observerades först i ett borrhål med hjälp av borrhålskamera. Senare kunde brottet även observeras på liggväggen. Brottet observerades efter att en konvergens på 56 mm uppmätts.

Inom ramen för ett bergförstärkningsprojekt som utfördes på 80-talet identifierades en stor bergkil som har analyserats med 2D- och 3D-analyser. Resultaten från dessa analyser visade på god överensstämmelse med det uppmätta beteendet. Modellerna kunde simulera kilens beteende och bekräfta att den var stabil. En annan observation från analyserna är att kilen troligen varit stabil utan de bultar den var förstärkt med.

De olika brottmekanismer som studerats i denna avhandling uppvisar skillnader i hur de utvecklas. Brottsprocessen som leder till spjälkbrott sker väldigt snabbt medan böj- och skjuvbrott utvecklas relativt långsamt. En kils beteende kan övervakas med rätt typ av instrumentering men deformationerna är små innan rörelser som leder till instabilitet sker. Data från extensometrar, totalstation, konvergensmätningar, borrhålsfilmning kombinerade med lämpliga numeriska analyser kan användas för att detektera brott och identifiera spjälk-, böj-, skjuv- och kilbrott.

SUMMARY

In this doctoral thesis work the relationship between the deformation and the initiation of failure around an underground excavation was studied. In this work data from observed failure and measured deformations was used.

This work is based on information obtained from laboratory test, underground field cases and numerical analysis. Field data from the underground cases was used as input data in the numerical analysis.

The underground field cases provided good information for analysis of failure and deformation. These cases provided valuable information due to the following characteristics: (i) spalling and deformation can be studied from the Garpenberg raise and Zinkgruvan exploration drift cases using numerical analysis, (ii) bending and shear can be studied from the Kristineberg mine since deformation measurements were conducted *in situ*, and (iii) wedge failure can be studied from the Kiirunavaara drift case since it was observed and deformation was measured *in situ*.

The failure-deformation process was analysed for fifteen tested rock types. Rock characteristics such as grain size and mineral compositions for these rock types were compared with a number of strain quantities. The comparison revealed that the crack damage lateral strain was strongly influenced by the grain size. Furthermore, the mineral composition slightly influenced the examined quantities. Both crack volumetric and volumetric strain quantities seems to be sensitive to grain size.

The comparison of the strain quantities, representing different deformation stages obtained from laboratory tests using information from limestone and quartzite, and calculated for the Garpenberg raise and the Zinkgruvan exploration drift cases using numerical analysis, helped to interpret the failure process around the opening in these two cases. The distances for strain concentration bands from the linear-elastic brittle and linear-elastic perfectly plastic analyses that were closest to the boundary were similar to the depth of the observed fallout for both cases.

The deformation pattern of a monitored stope in Kristineberg mine helped to determine that bending and shear failure took place in the HW and FW side of the stope. The shear failure was first observed by borehole camera surveys inside the walls, and then later daylighted on the surface of the stope. The onset of the shear failure was represented for a convergence of 56 mm.

In the Kiirunavaara drift case, the results from two local models (2D and 3D) showed qualitatively good agreement with the field observations. The models are able to simulate the wedge and determine the stability of the wedge. It can be inferred that the wedge did not fallout and remained stable. In fact the rock reinforcement installed in the field was not necessary to keep the wedge in place.

This work conclude that the failure process of each failure mechanism develop differently. The failure process due to spalling can occur very fast, while for bending and shear failure it is slow. The behaviour of wedges can be monitored as long as they are stable during the excavation process. Monitoring data from extensometers, total stations, convergence measurement, borehole camera surveys, combined with appropriate numerical analysis can be used for

estimating the failure and deformation of spalling, bending, shear and wedge failure. Deformation values were estimated for all failure mechanisms. Strain based failure criteria have to be developed and other input parameters have to be collected.

viii

TABLE OF CONTENTS

1   INTRODUCTION

1.1   Background

The design of underground excavations is dependent on the rock characteristics (i.e., properties, geology and discontinuities), the state of stress, and the imposed disturbance due to the excavation process. Failure developing in the rock mass near, or around the excavation, may lead to stability problems, which must be accounted for in the design. Stability problems caused by failure mechanisms such as spalling, bending, shear and wedge failure are typical in hard and weak rock masses around excavations, see Figure 1.

(a)

(b)

(c)

(d)
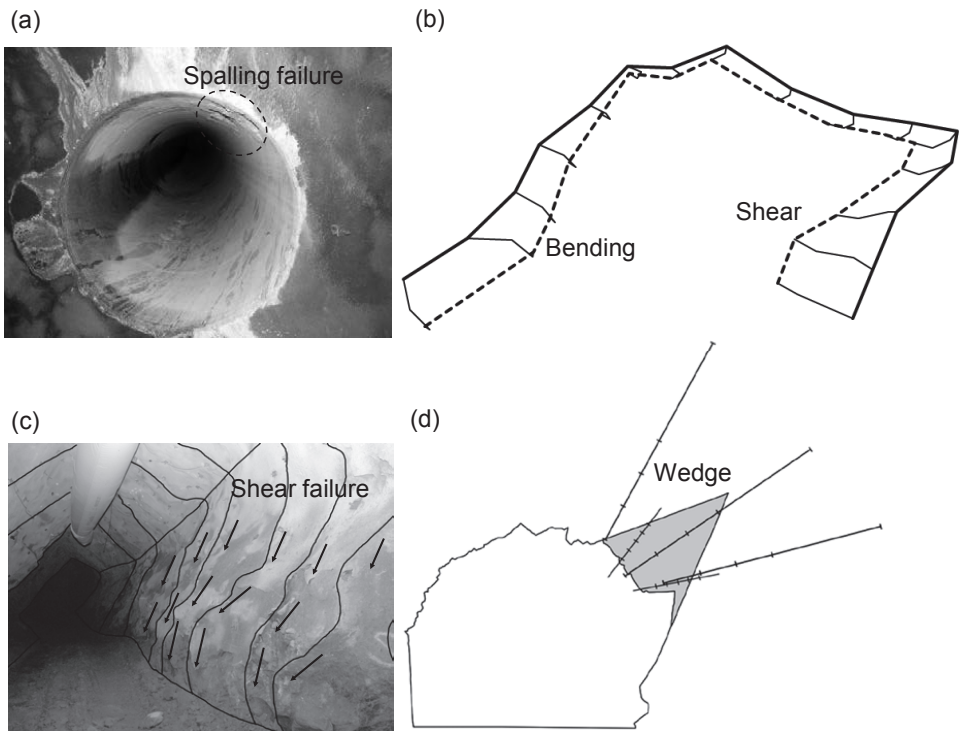
Figure 1 (a) Spalling failure observed in the Garpenberg mine, (b) bending indicated and shear failure observed in the Kristineberg mine, (c) shear failure observed in the Kristineberg mine, and (d) rock wedge formed in the Kiirunavaara mine.

Displacement of the rock mass commonly initiates near the excavation face due to the removal of the confinement from the excavated rock mass. If the induced stresses are high enough failure may be initiated and propagated. Thus, small or large volumes of rocks may slide, fall or

be ejected into the opening sometimes with the potential to injure people, cause property damage, and/or interrupt tunnelling and mining activities.

The failure process comprises the initiation and propagation of cracks and may lead to fallout and/or collapse of the excavation. Failure is manifested by an increase in deformation magnitude and maybe a change in the deformation pattern of the excavation. Therefore, it is important to assess the stage of the failure process in order to understand the stability of the excavation. This knowledge can be used to improve the design and performance of underground excavations in different rock masses and under different stress conditions. It is also important to assess the stage of the failure process in order to be able to decide on remedial measures to maintain a stable excavation.

1.2   Objectives

The objective of this thesis work was to improve the understanding of spalling, bending, shear and wedge failures in rock, and in particular how they develop under different loading and field conditions, how the effects of failure can be assess and how the deformations leading to failure and fallout can be evaluated.

1.3   Scope and limitations

Two main types of rock masses were studied in this work—hard-high strength crystalline rock (typical for the Fennoscandian rock shield) and weak-altered rock in a hard host rock mass. In this work the behaviour of some of the typical failure mechanisms developing in hard rock mass conditions such as spalling and wedge failure were investigated. Shear failure typical of weak rock masses and bending, which can occur in all types of rock masses, were also studied. Input data for the work was obtained from the following three sources:

i)   Laboratory tests: In the laboratory tests the behaviour of the rock mass in small scale was studied. Rock types from Swedish and Finnish sites including limestone, quartzite, diorite, norite, gabbro, diabases, syenite porphyry, mica gneiss, tonalite gneiss and a variety of granites were tested in uniaxial compression. No laboratory test was carried out as a part of the project, instead data from earlier tests, by other authors, were analysed.

ii)   Underground field cases with deformation measurements and damage mapping. The underground cases were selected on the basis that failure was observed and/or measurement of deformation was conducted in the field. Excavation types such as raises, stopes and drifts were studied which represented the behaviour of rock masses in macro scale. No field work was carried out as a part of the project. The majority of the cases are Swedish, and two are foreign (U.K. and Canada).

iii) Numerical analysis: The numerical analyses were used to simulate failure and calculate deformations due to failure.

1.4   Terms and conventions

According to Palmström and Stille (2007) terms such as failure, instability, behaviour types and failure modes are used inconsistently and differently in the literature, and often overlapping. Therefore, in this work the definition for failure and failure mechanisms from Bieniawski

(1967) was used, however, with some modifications. The failure mechanism (e.g., spalling, bending, shear and wedge) describes the non-elastic physical process taking place in the rock in the course of loading. A failure mechanism might result in fallouts. Fallout is a process when volumes of rock are detached from the host rock mass.

The failure-deformation behaviour is the response of the rock to formation, propagation and coalescence of cracks, in micro- as well as macro scale. This process is illustrated by typical stress-strain curves from laboratory tests and/or from field monitoring of progressing rock mass failure.

A geomechanical sign convention was used throughout this work for stress and strain, with compressive stresses and strains taken as positive. However, for the field measurements, as well as in the modelling using *UDEC* and *3DEC*, both stresses and strains are negative in compression and positive in tension. For the *Phase2* modelling the stresses are positive in compression.

2   FAILURE AND DEFORMATION

2.1 Failure mechanisms

2.1.1 General

A system is unstable if it does not return to its state of equilibrium after having been disturbed (Andreev, 1995). Hoek and Brown (1980) identified four principal sources of underground instability.

(i)   High rock stress failure associated with hard rock. This kind of failure can occur e.g., when mining at great depth or for large excavations at shallow depth. Stress conditions for tunnelling in steep mountain regions or in weak rock conditions can also result in stress-induced instability problems;

(ii)   Structurally controlled failure tends to occur in faulted and jointed hard rocks, in particular when several joint sets are steeply inclined;

(iii) Weathered and/or swelling rock failure often associated with relatively poor rock. This kind of failure may also occur in isolated seams within an otherwise sound hard rock; and

(iv)   Groundwater pressure or flow induced failure, which can occur in almost any rock mass. If this failure is combined with any of the other types of instability listed above, it could reach serious proportions.

According to Palmström and Stille (2007), more than one stability problem can occur simultaneously. This depends on factors such as the composition of the rock mass, stress, groundwater pressure, and size of the excavation.

Hoek et al., (1995) studied different types of failure and stability problems in underground excavations under high and low *in situ* stress condition and as a function of the jointing of the rock mass. Martin et al., (2001) incorporated the effect of the intermediate in-situ stress as presented in Figure 2. Spalling and slabbing are typical failure mechanisms in massive rock masses with few discontinuities and high level of stresses. In heavily jointed rock masses a more ductile type of failure can be expected. When the rock mass comprises many intersecting joints blocks can be formed which increases the likelihood of blocks sliding or falling into the opening. Plastic failure is typical for rock masses with joints with slickensided surfaces and clay mineral infillings. Buckling failure may occur in anisotropic/stratified rock masses. Table 1 shows the failure behaviour investigated in this doctoral work.
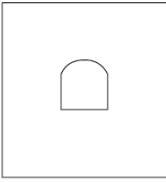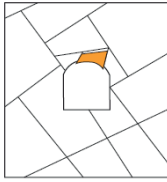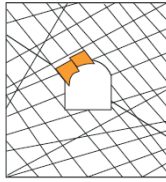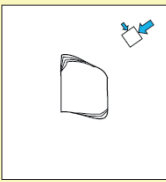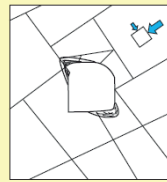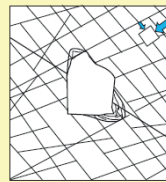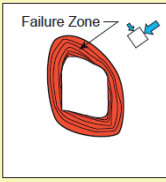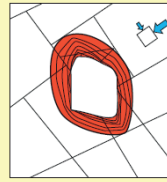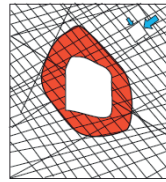
	Massive (GSI > 75)	Moderately Fractured (50 > GSI < 75)	Highly Fractured (GSI < 50)	
Low In-Situ Stress ($\sigma_1 / \sigma_c < 0.15$)	Linear elastic response.	Falling or sliding of blocks and wedges.	Unravelling of blocks from the excavation surface.	$Di < 0.4 (\pm0.1)$
Intermediate In-Situ Stress ($0.15 > \sigma_1 / \sigma_c < 0.4$)	Brittle failure adjacent to excavation boundary.	Localized brittle failure of intact rock and movement of blocks.	Localized brittle failure of intact rock and unravelling along discontinuities.	$0.4 (\pm0.1) > Di < 1.1 (\pm0.1)$
High In-Situ Stress ($\sigma_1 / \sigma_c > 0.4$)	Failure Zone. Brittle failure around the excavation.	Brittle failure of intact rock around the excavation and movement of blocks.	Squeezing and swelling rocks. Elastic/plastic continuum.	$Di > 1.1 (\pm0.1)$

Figure 2 Types of failure and instability problems in massive, moderately and highly fractured rock masses under low, intermediate and high in situ stresses (modified from Hoek et al., 1995 as referenced in by Martin et al., 2001).

Table 1 Failure behaviour investigated in this doctoral work.

Rock mass	Failure	Behaviour
Hard and brittle	Spalling	Sudden detachment of thin rock slabs
Anisotropic	Bending	Deflection of column and/or beam when it is subjected to a force that is applied axial and/or perpendicular to its axis.
Weak-altered	Shear	Shearing of the rock mass resulting in a shear surface and/or shearing along a pre-existing weakness zone/ discontinuity in the rock mass
Hard rock	Wedge	Falling or sliding of blocks formed by pre-existing discontinuities

2.1.2 Spalling failure

The understanding of spalling failure is important for analysis of stability in brittle and highly stressed rock masses. In this chapter, the mechanism of brittle rock fracture as referenced in by Bieniawski (1967) is presented.

Griffith's hypothesis for brittle fracture can be used as a criterion for fracture initiation (Hoek and Bieniawski, 1965). However, this criterion also needs to incorporate the fracture propagation to correctly predict the ultimate strength of a material (Barenblatt, 1966). The fracture initiation criterion considers the effect of stress conditions, which may influence the stabilization of fracture propagation. Griffith's criterion can be derived using (i) the stress field near the tip of a pre-existing (Griffith) crack, or (ii) the energy balance for a pre-existing (Griffith) crack. The fracture initiation criterion expressed in terms of the critical applied stress for uniaxial tension is expressed as follows.

$$\frac{(\sigma_1 - \sigma_3)^2}{\sigma_1 + \sigma_3} = -8\sigma_t \tag{1}$$

where σ_1 and σ_3 are the major and minor principal components of the applied stress, respectively, and σ_t is the uniaxial tensile strength of the material.

A modification of the Griffith's hypothesis was proposed by McClintock and Walsh (1963) since the original hypothesis did not consider the compressive applied stress. The modified criterion also account for crack closure under compression on the tensile stress at the crack tip since the original criterion by Griffith considered an open crack. The modified criterion is defined as

$$\sigma_1 = \frac{-4\sigma_t}{\left(1 - \frac{\sigma_3}{\sigma_1}\right)\sqrt{(1 + \mu^2)} - \mu\left(1 + \frac{\sigma_3}{\sigma_1}\right)} \tag{2}$$

The criterion can also be expressed in terms of the uniaxial compressive strength (σ_c).

$$\sigma_1 = \sigma_3 \left[\frac{\sqrt{1+\mu^2}+\mu}{\sqrt{1+\mu^2}-\mu} \right] + \sigma_c \tag{3}$$

where σ is the critical tensile stress at the crack tip, and μ is the coefficient of internal friction between crack surfaces.

The energy balance for a pre-existing (Griffith) crack based on the relation between the elastic strain energy stored in the structure, and the surface energy in the free faces of the pre-existing crack can be expressed as follows

$$W = W_e + W_s \tag{4}$$

where W is the applied energy, W_e is the elastic strain energy, and W_s is the crack surface energy.

The applied energy may be balanced either by increasing (i) the strain energy, or (ii) the crack surface energy, or (iii) partly the elastic strain energy and partly the crack surface energy. In the first case the crack does not extend, and in the other two cases if the crack extends, the crack surface energy increases. The crack extension onset condition is

$$\sigma = \sqrt{\frac{2\gamma E}{\pi c}} = \sigma_{IN} \tag{5}$$

where σ is the applied uniaxial tensile stress, σ_{IN} is the critical stress defining fracture initiation, E is the Young´s modulus, γ is the specific surface energy (i.e., surface energy per unit length of the crack surface), and $2c$ is the length of the pre-existing crack.

Fracturing is initiated when the applied stress reaches the critical value σ_{IN}. Two conditions exist (i) $\sigma < \sigma_{IN}$ for no fracture propagation, and (ii) $\sigma > \sigma_{IN}$ for stable fracture propagation. Irwin (1960) proposed two hypotheses defining the conditions for stable and unstable fracture propagation as expressed as

$$\sigma = \sqrt{\frac{GE}{\pi c}} \quad \text{and} \tag{6}$$

$$\sigma \geq \sqrt{\frac{G_c E}{\pi c}} = \sigma_{UFP}, \tag{7}$$

respectively, where G is the energy released per unit crack surface, G_c is the critical energy value and characteristic property of the material, and σ_{UFP} is the critical value of the applied stress defining the limit between stable and unstable crack growth. When the critical value at the applied stress is exceeded, the crack growth velocity and fracture propagation cannot be controlled anymore by the applied load.

2.1.3 Bending failure

Parallel lamination is a common structural control as stated by e.g., Diederichs (1999). Horizontally bedded and vertically jointed roofs are referred to in the literature as laminated

roof or stratified rock mass. According to Brady and Brown (2004), the detachment and deflection of the roof should be considered in excavation design. Diederichs (1999) used the Voussoir beam theory to explain the stability of laminated hangingwalls of two field cases where buckling was observed. Several other applications of the Voussoir beam theory to laminated roofs have been reported among others by Seedsman (1986) and Hatzor and Benary (1998).

The Voussoir beam theory uses the expressions for load carrying and deflection characteristics of beams from the Euler–Bernoulli beam theory. Beams are by definition long straight members that carry loads perpendicular to their longitudinal axes (Hibbeler, 2005). Beams subjected to a bending moment are deformed, hence deflecting along its longitudinal axis (Figure 3a). Deflection can also be experienced by long slender members like columns. According to Hibbeler (2005) columns are subjected to an axial compressive force and the lateral deflection that occurs is buckling or bending (Figure 3b).

Several studies on beam theory have been reported among others by Fayol (1885), Evans (1941), Sterling (1980) and Brady and Brown (1993, 2004), as referenced in by e.g., Seedsman (1986), Hatzor and Benary (1998), Diederichs (1999), and Brady and Brown (1993, 2004). A design procedure for the analysis of mine roof beams using the Voussoir beam theory was developed by Evans (1941) and modified by Beer and Meek (1982) as reported by Seedsman (1986) and Brady and Brown (1993, 2004). The design was modified and an iterative design procedure was proposed by Brady and Brown (1985), and revisited and extended by Brady and Brown (2004). A detailed description of the Voussoir beam mechanism for the design of underground mining in stratified rock mass can be found in Brady and Brown (1993, 2004).
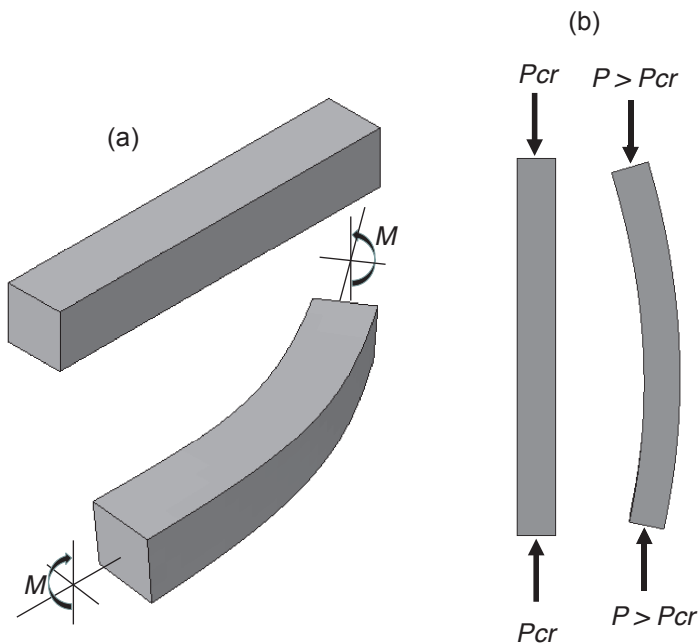
Figure 3 (a) Bending deformation of a long straight member, and (b) buckling of column (modified from Hibbeler, 2005). Bending moment (M), vertical force (P), critical load (Pcr).

Modes of failure of roof beds have been verified in experimental arrangements conducted by Sterling (1980) as referenced in by e.g., Brady and Brown (1993, 2004), Diederichs (1999). These modes of failure summarized by Diederichs (1999) are buckling or snap-through failure, lateral compressive failure (crushing) at the midspan and abutments, abutment slip, and diagonal fracturing as shown in Figure 4. According to Palmström and Stille (2007), buckling occurs due to deflection of the rock. Physical model tests using plasters and sand to simulate the rock, and mica powder to simulate the interlayer, conducted by Yun-mei et al., (1984) shows buckling failure in side walls as presented in Figure 5.
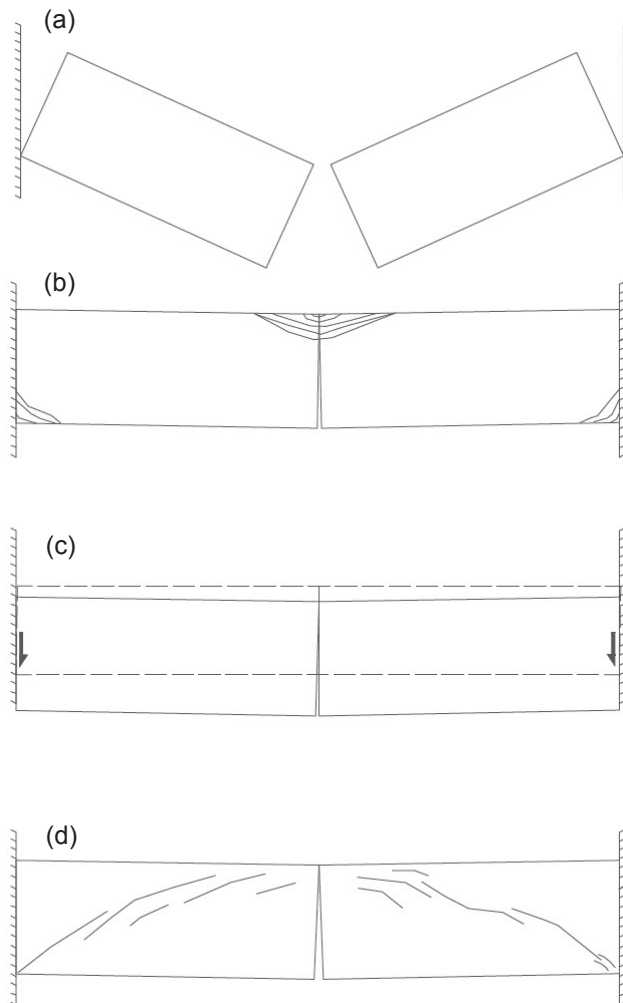
Figure 4 Voussoir beam failure mode verified in laboratory tests by Sterling (1980): (a) snap-through or buckling, (b) crushing, (c) sliding and/or shear failure, and (d) diagonal cracking (as referenced in by Diederichs, 1999).
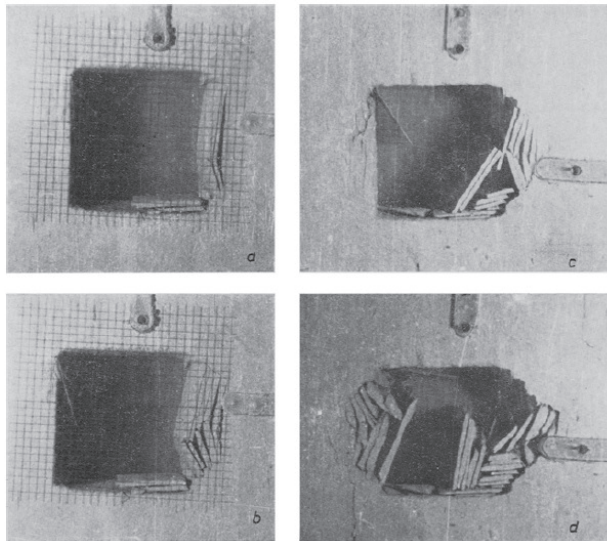
Figure 5 Model tests for buckling failure (Yun-mei et al., 1984).

2.1.4 Shear failure

The term shear failure in this thesis is defined in Table 1, i.e., shearing of the rock mass resulting in a shear surface and/or shearing along a pre-existing weakness in the rock mass. The slip along weakness planes is a problem in the design in stratified rock masses (Brady and Brown, 2004). Based on Sterling (1980), for a Voussoir beam with low/thickness ratio, the most likely failure mode is shear failure at the abutments as referenced in by Brady and Brown (2004). An example of shear failure in rock masses are the ground problems found in the Kristineberg mine (Sweden). These are traditionally been characterized by slip along the footwall contact as reported by Krauland et al., (2001) and result in the development of a shear failure daylighting in the stope. The failure is similar to a Prandtl wedge failure.

2.1.5 Wedge failure

Rock wedges are formed by discontinuities in a fractured/jointed rock mass and the free surface of the opening. They are volumes of rock that may fall from the roof or slide from the sidewalls into the opening. At least three intersecting joints are needed to form a wedge. Wedges are the most common structurally controlled failure in underground constructions (e.g., Diederichs, 1999). For low-stress conditions (i.e., when clamping stresses can be ignored), stereographic projection techniques can be used to analyse instability due to wedges. The stereographic techniques can be used manually using stereographic nets or with a software such as *Dips* (Rocscience, 2013). The reader is referred to Hoek and Brown (1980) for a detailed description of wedge stability analysis.

Factors that affect the stability of a wedge in underground excavations are for example *in situ* stress, size, shape and orientation of the excavation. The best orientation of the excavation is the one that gives the minimum volume of potential unstable wedge. The volume of a

potentially unstable wedge may increase with increasing span of the excavation, which consequently increases the cost for wedge support.

Wedge stability has been studied analytically by e.g., Elsworth (1986), Mauldon and Ureta (1996), Jian et al., (2013), Sofianos et al., (1999). Sofianos (1986) and more recently Nomikos et al., (2002) and Bagheri and Stille (2011, 2013) have investigated block stability using analytical solutions and numerical analysis. Bagheri (2011) explained that the natural support provided by the rock stress around a wedge can increase the stability of the wedge.

2.2 Deformation

2.2.1 Intact rock

Multiaxial compression experiments were used to study the mechanism of brittle fracture of rock by e.g., Bieniawski (1967), Eberhardt et al., (1998), Eberhardt et al., (1999), and Martin and Chandler (1994). Uniaxial and triaxial compressive tests in which axial and lateral strains are recorded make it possible to identify several characteristic stress levels of the intact rock which are important for the understanding of the damage process of brittle rock. The different stages of brittle fracturing are described below and shown in Figure 6. Table 2 defines all stress and strain quantities related to the failure-deformation process illustrated in the figure. The failure-deformation process of a number of rock types has also been studied by Eloranta and Hakala (1998, 1999a,b), Hakala and Heikkilä (1997a,b), Heikkilä and Hakala (1998a,b), Carlsson (2010), Carlsson and Nordlund (2013a,b), Carlsson et al., (1999).
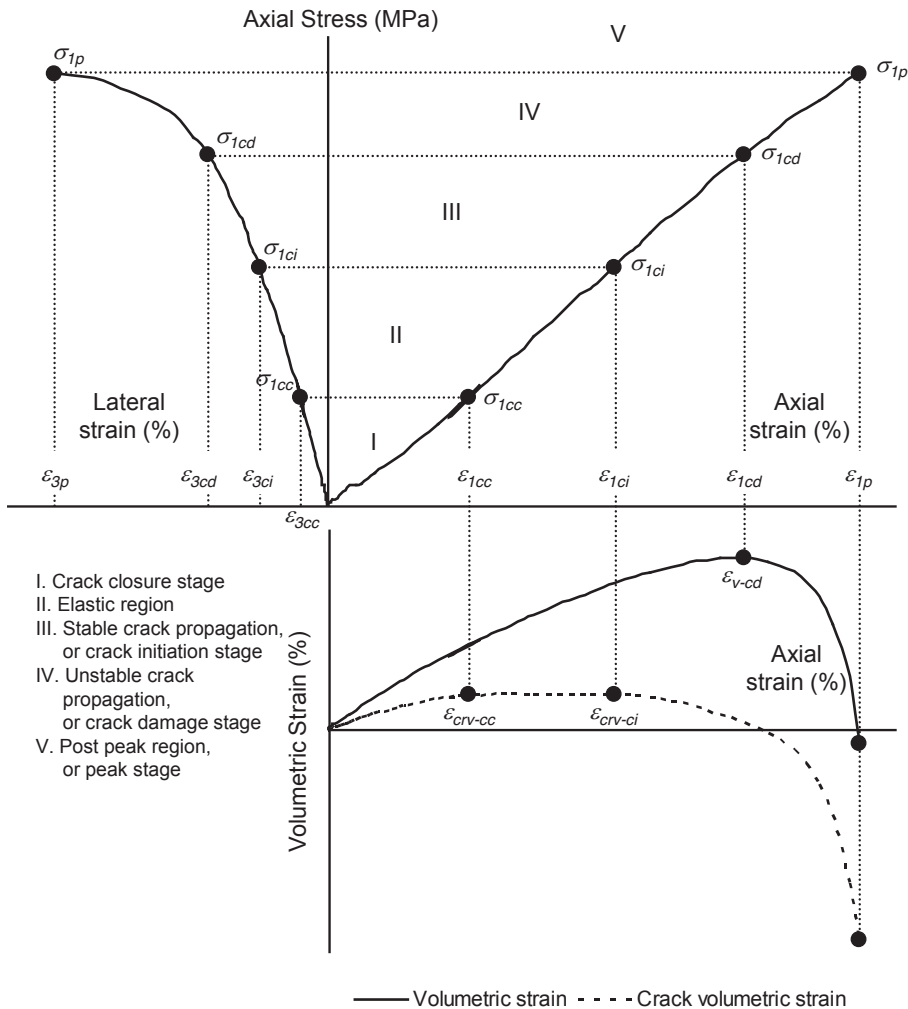
Figure 6 Failure-deformation process of the intact rock.

Stage I – Closure of microcracks (σ_{cc} is the stress at crack closure): Pre-existing cracks oriented at an angle to the applied load close. In this stage the relative movement of aligned crack walls is parallel to the direction of the applied load. The stress-strain response is non-linear, exhibiting an increase in axial stiffness.

Stage II – Linear elastic deformation: The behaviour of the rock is almost linear-elastic. Young's modulus and Poisson's ratio can be calculated from the part of the stress-strain curve representing this stage (since it is linear).

Stage III – Stable fracture propagation (σ_{ci} is the stress at crack initiation): Dilation (i.e., crack volume increase) begins and is only registered by the lateral strain gauges, thus reflecting the

development of cracks parallel to the direction of the applied load. This stage is difficult to identify from the stress-strain curve due to a high density of microcracks of the tested sample, hence a crack volumetric strain versus axial strain plot is recommended. Crack initiation can be defined as the point where the lateral strain curve departs from linearity. However, this method is very subjective when highly fractured samples are tested.

Stage IV – Unstable fracture propagation (σ_d is the stress at crack damage): Crack propagation in this stage is unstable. The unstable crack growth is associated with the point of reversal in the volumetric strain curve.

Stage V – Failure and postpeak behaviour: Coalescence of microcracks occurs and the rock cannot longer sustain more load. The peak strength (σ_{1p}) of the material marks the beginning of post-peak behaviour.

Table 2 Stress and strain quantities at each deformation stage.

Stress and strain quantity	Deformation stage			
	I	III	IV	V
	cc	ci	cd	p
Axial stress [MPa]	σ_{1cc}	σ_{1ci}	σ_{1cd}	σ_{1p}
Axial strain [%]	ε_{1cc}	ε_{1ci}	ε_{1cd}	ε_{1p}
Lateral strain [%]	ε_{3cc}	ε_{3ci}	ε_{3cd}	ε_{3p}
Crack volumetric strain [%]	$\varepsilon_{crv\text{-}cc}$	$\varepsilon_{crv\text{-}ci}$	-	-
Volumetric strain [%]	-	-	$\varepsilon_{v\text{-}cd}$	-

crv = crack volumetric, *v* = volumetric strain

2.2.2 Rock mass

Rock mass movement (i.e., deformation in terms of strain and/or displacement) as a result of failure cannot be avoided during the excavation process if the stress magnitudes are high enough to exceed the rock mass strength. Failure of the rock mass can be initiated ahead of, or behind, the advancing face depending on the stress magnitude. Since the excavation process removes rock, which acts as a support, the new face will become the remaining natural support together with the floor, roof and walls behind the face. Thus, extensive deformations with only limited fallout volumes and/or large fallout volumes from the roof and/or the sidewalls without extensive deformation may occur. Monitoring of deformations and damage mapping are important tools to assess the development of deformations, failure and fallout and as a basis for the design of rock support. Typical monitoring instruments and methods are convergence and total station measurements, extensometers and laser scanning. Since the deformations in the field are commonly measured behind the excavation face the total deformation is not recorded. Numerical analysis can be used as a complement to calculate the total displacements and for prediction.

Analysis of convergence in tunnels has been the subject of many publications e.g., Panet and Guenot (1982), Zhang et al., (2008), Vlachopoulos and Diederichs (2009). However, failure has not been linked to the measured deformation in those studies. A few examples of deformation monitoring of spalling failure are the Mine-by Experiment (MBE) as reported by e.g., Martin

(1997), Cai et al., (2001), Read (2004), and the Äspö Pillar Stability Experiment (APSE) by Andersson (2007). Studies on deformation related to buckling failure of real cases have been reported by Diederichs (1999).

The result of the monitoring can be used together with analyses of the interaction between the rock mass and the rock support, e.g., Ground Reaction Curve (GRC) – Support Reaction Curve (SRC) (Brown et al., 1983; Carranza Torres and Fairhurst, 2000; Alonso et al., 2003, among others) to study the behaviour of the ground and for principal design of rock support. The development of the deformation as a function of the face advance, i.e., Longitudinal Deformation Profile (LDP) (Carranza Torres and Fairhurst, 2000; Zhang et al., 2008; Vlachopoulos and Diederichs, 2009; Alejano et al., 2012) is another method that may give indication of changes in behaviour from stable to unstable.

The application of GRC is, e.g., illustrated and described by Hoek and Brown (1980) and Brady and Brown (1993). Figure 7a, shows a tunnel that is excavated with drilling-and-blasting. The tunnel is supported after each excavation cycle. At section X-X the radial displacement on the boundary of the opening develops as the face of the excavation advances, see Figure 7b.

In step 1, the tunnel face has not reached the section X-X, and the rock mass is in equilibrium. In step 2, the face has advanced beyond section X-X and the internal support pressure (p_i) previously provided by the rock mass dropped to zero (Hoek and Brown, 1980; Brady and Brown, 1993). The tunnel will not collapse because the radial displacement (u) is limited by the proximity of the tunnel face providing restraint. The zone of influence of the face is 2.25 times the tunnel radius from the excavation face (Brady and Brown, 1993). In step 3, the blasted rock is mucked out and steel sets installed close to the face. The supports carry no load and no further deformation takes places due to the support. In step 4, the face has advanced about 1½ diameters beyond section X-X and the restraints that was provided by the face is now negligible causing further radial deformation of the tunnel walls and roof. Finally in step 5, the face is advanced so far beyond section X-X that no restraint is provided by the face to the rock mass at section X-X.
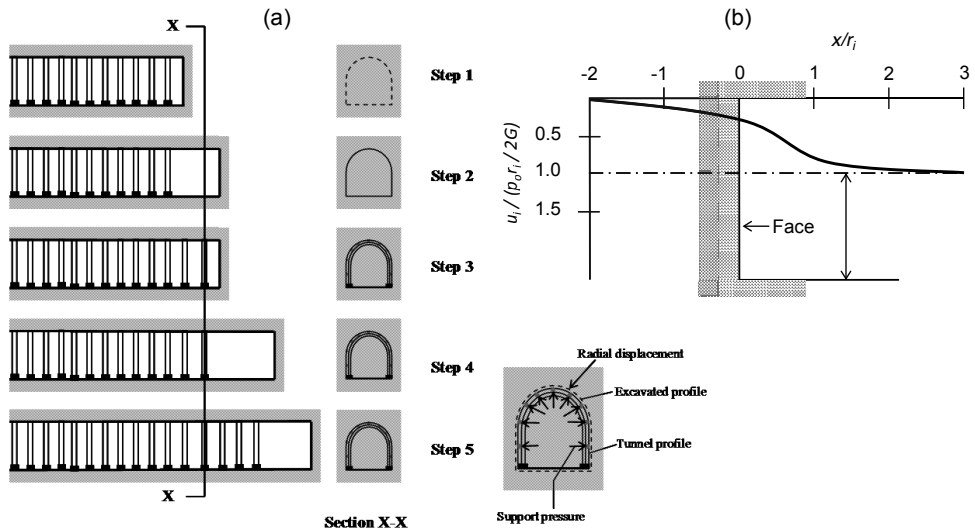
Figure 7 (a) Supported tunnel being excavated with drilling-and-blasting methods, and (b) radial displacement (u_i), of a circular tunnel of radius (r_i) in a hydrostatic field (p_o) normalized with respect to the plane strain displacement [u_i /($p_o r_i$/2G] (modified from Brady and Brown, 1993).

2.2.3 Deformation based failure criteria

The majority of the failure criteria reported in the literature are formulated in terms of stresses (Edelbro, 2003). Further investigation conducted in this doctoral work showed that there are, in fact, several failure criteria that use strain quantities to evaluate stability in underground excavation. These criteria are summarized as follows. Stacey and De Jongh, (1977) observed that fracture associated with tunnel boring in hard rock occurred at stress levels that were too low on the basis of the Mohr criterion. The fractures in the sidewalls and ahead of the face and their orientations were different from those predicted by the Mohr theory. Successful prediction of both orientation and extent of fracturing was achieved using an extension strain criterion (Stacey, 1981). This criterion states that fracturing occurs when the tensile strain exceeds a limiting value which is dependent on the properties of the rock. The criterion can be used in areas around underground excavation with low confinement stress and is expressed as:

$$\varepsilon_3 \le \varepsilon_{cr} < 0 \tag{8}$$

where ε_3 is the minor principal strain, and ε_{cr} is the critical extension strain.

Aydan et al., (1993) suggested a method to evaluate the squeezing potential of tunnels. The method was based on the analogy between the axial stress-strain response of rocks in laboratory tests and the tangential stress-strain response of rocks surrounding tunnels. A classification of the potential for squeezing was proposed: (i) No squeezing: $\varepsilon_\theta^a / \varepsilon_\theta^e \le 1$, (ii) light squeezing:

$1 < \varepsilon_\theta^a / \varepsilon_\theta^e \le \eta_p$, (iii) fair squeezing: $\eta_p < \varepsilon_\theta^a / \varepsilon_\theta^e \le \eta_s$, (iv) heavy squeezing: $\eta_s < \varepsilon_\theta^a / \varepsilon_\theta^e \le \eta_f$, and (v) very heavy squeezing: $\eta_f < \varepsilon_\theta^a / \varepsilon_\theta^e$, where

$$\eta_p = \frac{\varepsilon_p}{\varepsilon_e} \quad \eta_s = \frac{\varepsilon_s}{\varepsilon_e} \quad \eta_f = \frac{\varepsilon_f}{\varepsilon_e} \tag{9}$$

and ε_e, ε_p, ε_s and ε_f are the absolute strains during the elastic and peak stages, and during the weakening and flowing stages, respectively.

A uniaxial stress-strain relationship for rock and soil was proposed by Sakurai (1981) for assessing stability of underground openings

$$\sigma = \frac{\varepsilon E_i}{1 + a\varepsilon E_i} \tag{10}$$

where σ is the uniaxial stress, ε is the uniaxial strain, E_i is the initial modulus of elasticity, and $1/a$ is the asymptotic value of σ according to Equation (10). The critical strain and the failure strain were defined as

$$\varepsilon_0 = \frac{\sigma_c}{E_i} \quad \text{and} \quad \varepsilon_f = \frac{\varepsilon_0}{1 - R_f}, \text{ respectively,}$$

where R_f for a number of rocks and soils has values in the range 0.005 to 0.8 (Sakurai (1981). Sakurai et al., (1993) presented a new criterion expressed in terms of the shear strain

$$\gamma_0 = \frac{\tau_{max}}{G_{50}} \tag{11}$$

where τ_{max} is the maximum shear strength, and G_{50} is the shear modulus at 50% of τ_{max}. However, since the determination of the maximum shear strength required equipment for torsional shear testing and torsional shear tests are inapplicable to hard rocks the criterion was re-formulated as (for isotropic materials)

$$\gamma_0 = (1 + \nu)\varepsilon_0 \tag{12}$$

where ν is the Poisson's ratio, and ε_0 is the critical normal strain.

A strain-strength criterion for rock was suggested by Chang (2006).

$$\varphi(\varepsilon_{ij}) = \kappa\varepsilon_1 - \varepsilon_v - \varepsilon_c \tag{13}$$

where ε_v is the volumetric strain, ε_1 is the major principal strain, and κ and ε_c are parameter governing the hardening/softening behaviour. The parameters are constant for perfectly plastic material. Later, (Chang (2011), suggested a damage criterion expressed as

$$\varepsilon_v = \kappa\varepsilon_1 - \varepsilon_c \tag{14}$$

This criterion was based on results from a number of laboratory tests which indicated a linear correlation between the volumetric strain and the major principal strain at yield state.

The presented criteria are somewhat scattered with respect to usability, types of applications and rock conditions. The criterion by Stacey (1981) represents the onset of fracturing while the criteria by Sakurai (1981, 1993) and Chang (2011) are yielding/damage criteria.

3   UNDERGROUND CASE STUDIES

In this Chapter eight underground cases are presented, see Table 3. Failure was observed in seven cases and deformation measurement was conducted in six of them. The cases are presented in the order the failure mechanisms were studied in this doctoral work, i.e., Garpenberg raise and Zinkgruvan exploration drift first for spalling failure; Kristineberg stope second for bending and shear failure; and Kiirunavaara drift last for wedge failure. The other cases were studied through the literature but not analysed in detail in this doctoral work.

Table 3 Underground excavation cases.

Case	Excavation	Rock mass	Failure mechanism	Deformation measurement
Garpenberg raise	Underground mine	Hard	Spalling	No
Zinkgruvan exploration drift	Underground mine	Hard	Spalling	No
Kristineberg stope	Underground mine	Weak	Bending and shear	Yes
Kiirunavaara drift	Underground mine	Hard	Wedge	Yes
Arlandabanan	Tunnel	Hard	-	Yes
Heathrow tunnel collapse	Tunnel	Soil	Collapse	Yes
Äspö Pillar Stability Experiment (APSE)	Experiment	Hard	Spalling	Yes
Mine-by Experiment (MBE)	Experiment	Hard	Spalling	Yes

All cases are from Sweden (see Figure 8), except Heathrow tunnel collapse (U.K.) and Mine-by Experiment (Canada).
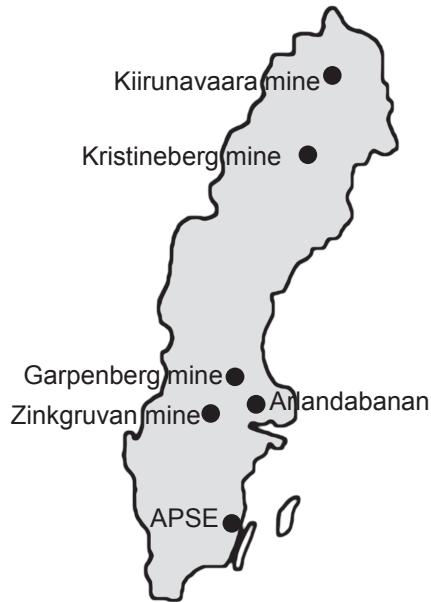
Figure 8 Location of the Swedish underground cases.

3.1 Garpenberg raise

The Garpenberg mine is owned and operated by Boliden Mineral AB. The mine is located approximately 177 km north-west of Stockholm. The extracted ore contains zinc, silver, lead, copper, and gold. Mining of the orebody is currently conducted at the 1080 m level. The diameter of the studied raise was 2.13 m and is situated at a depth of 830 to 880 m below the ground surface. The mining area was located 175 m from the raise, hence the raise was not influenced by the mining. The mining area was developed mainly in limestone, but some sections of the raise contained dolomite-limestone and breccia. According to Edelbro (2008) spalling failure on the surface of a vertical raise started immediately after raising, in the direction perpendicular to the measured major principal stress (Figure 9). The fallout due to spalling in the raise was small. The maximum depth of failure was 0.05 m. No deformation measurement was conducted. The raise was unsupported at the time that spalling failure occurred.
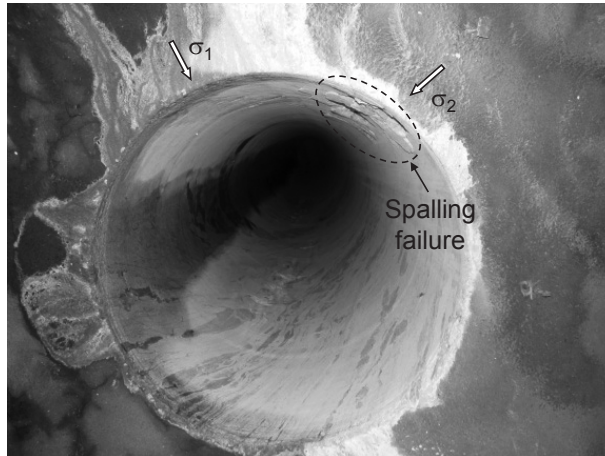
Figure 9 Garpenberg mine raise showing spalling failure and orientation of principal stresses (Edelbro, 2008).

3.2 Zinkgruvan exploration drift

The Zinkgruvan mine is owned and operated by Lundin Mining. The mine is located approximately 250 km south-west of Stockholm in south-central Sweden. The ore is extracted by either sublevel or longhole open stoping with subsequent paste filling of the stopes. The ore contains mainly zinc and lead, with silver as a by-product. Mining of the orebody is currently conducted at 1130 m depth. Spalling was observed in an exploration drift, see Figure 10 (Sjöberg, 2005). The exploration drift was excavated at the 965 m level (the ground surface is approximately at the 0 m level). The exploration drift is 4.7 m wide and 4.5 high. The failure was not influenced by the pre-existing structures. Fallout due to spalling was observed in the roof of the drift and the depth was estimated to between 0.1 and 0.2 m. The dominating rock type in the drift is brittle, quartz-feldspar leptite. Failure was not observed when the drift was parallel to the major horizontal stress (Figure 10). No deformation measurements were conducted.
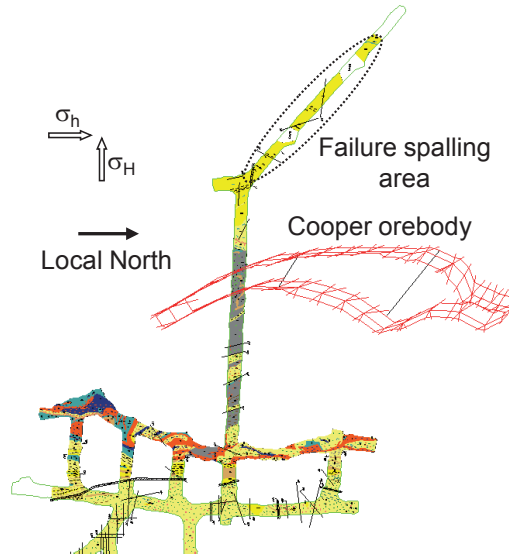
Figure 10 Exploration drift of Zinkgruvan mine (Sjöberg, 2005).

3.3 Kristineberg stope

The Kristineberg mine is located in the municipality of Lycksele, Västerbotten County, approximately 100 km west of the town of Boliden and 130 km west of the city of Skellefteå, see Figure 8. The mine is owned and operated by Boliden Mineral AB. Kristineberg is one of the deepest mines in Sweden, with operations on levels 850-1320 m below the ground surface. The mine comprises a polymetallic ore containing zinc, copper, lead, gold and silver, as well as copper ore and gold ore. The primary mining method used is overhand mechanized cut and fill. After a stope has been mined out, development rock (to the extent it is available) is placed in the stope, followed by backfilling of the remaining volume with hydraulic tailings. When the orebody is more than 8 m wide, a drift-and-fill method is used. Successful exploration programmes have discovered new mineralization at depths of 800 – 1300 m, some 500 m north of the orebodies currently mined. In 2009, the Kristineberg mine produced a total of 670,000 tonnes of ore (http://www.boliden.com; Krauland et al., 2001).

The general failure mechanisms experienced in the Kristineberg mine are shown in Figure 11, and described by Krauland et al., (2001). High horizontal stresses forces the roof to punch into the FW. The weak chlorite zone in the FW is then squeezed downward, and sliding occurs along the chlorite-country rock interface or along failure surfaces developed through the weak rock in the HW. The chlorite-country rock interface often consists of a clay seam. The high lateral stresses induce typical back-parallel fractures which often is a consequence of the squeezing. Because of frictional drag along the ore-footwall contact, the roof tends to pull apart and form roof parallel fractures. This results in propagation of roof falls that run up-dip. Chlorite zones within the ore have a similar effect on the adjacent ore. The failure in the roof progresses upward as the chlorite zone is squeezed out until equilibrium is achieved. The HW is somewhat stronger than the FW and tends to deform in a bending mode, with dilatational

separation occurring between the country rock and the schist or along the foliation of the schist itself.

A 50 m long area of a stope in the Kristineberg mine was monitored in 2010 as part of a field test on rock support conducted by Boliden Mineral AB. The stope was monitored with strain gauged D-bolts, extensometers, total stations and tape extensometers. The objective of the field test was to evaluate the D-bolt in the field and to study the interaction of rock mass and rock support. The field test also included borehole camera surveying and damage mapping of the whole stope. The field measurement was conducted at the mining depth Z1200 m, stope J10-3, cut #4. At cut #4, the stope was approximately 7 m wide and 6.25 m high. The measurement sections were located in the middle of each round.
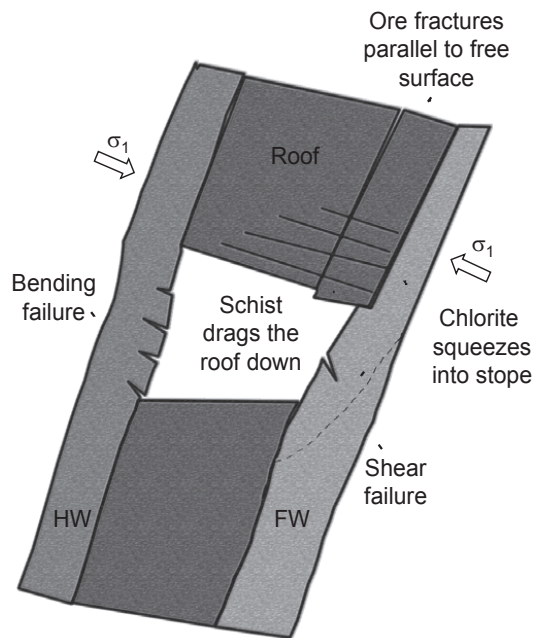
Figure 11 General failure mechanisms in Kristineberg mine (Board et al., 1992).

3.4   Kiirunavaara drift

The Kiirunavaara mine is located in the city of Kiruna in northern Sweden. The mine is owned and operated by the mining company Luossavaara Kiirunavaara AB (LKAB). The Kiirunavaara mine is currently the world's largest underground iron ore mine. Mining started as an open pit operation with a transition to underground mining in the early 1960s. Presently, underground mining is carried out using large-scale sublevel caving. About 28 million tonnes (Mton) of crude ore is currently mined annually. The magnetite orebody is about 4 kilometres long and 80 metres thick on average. The mineralisation has been demonstrated to a depth of at least 1,500 metres. It strikes north-south and dips 55°-60° eastwards. Mining of the orebody is currently

conducted between level 775 and 1045 m. The Kiirunavaara bedrock is volcanic precambrian hard rock. The major tectonic joint structures strike north-south and east-west. Both these joint sets dip steeply to the east. The footwall comprises trachyte, internally (within LKAB) designated as syenite porphyry. The hangingwall consists of rhyolite, internally designated as quartz porphyry. Contact zones of limited width are found in both the hangingwall (HW) and footwall (FW). The rock mass quality is generally good for most of the rock units, but, locally, rock conditions vary from high-strength, brittle rock to altered, slightly weathered rock with clay- and chlorite-filled discontinuities (Björnfot and Stephansson, 1984; Malmgren, 2005; Sjöberg and Malmgren, 2008; www.lkab.com).

According to Björnfot (1983d) a large rock wedge was observed in the FW side of the test drift at 514 m level (the ground surface is approximately at the 285 m level). The drift was approximately 7 m wide and 5.3 m high. The cross-section of the wedge in the monitoring sections R5 and R6 is shown in Figure 12. Several extensometers (EX) intersected the wedge. An upper and lower joint formed the wedge as illustrated in the same figure. The behaviour of the wedge was not described or studied in detail by Björnfot (1983a,b,c,d).
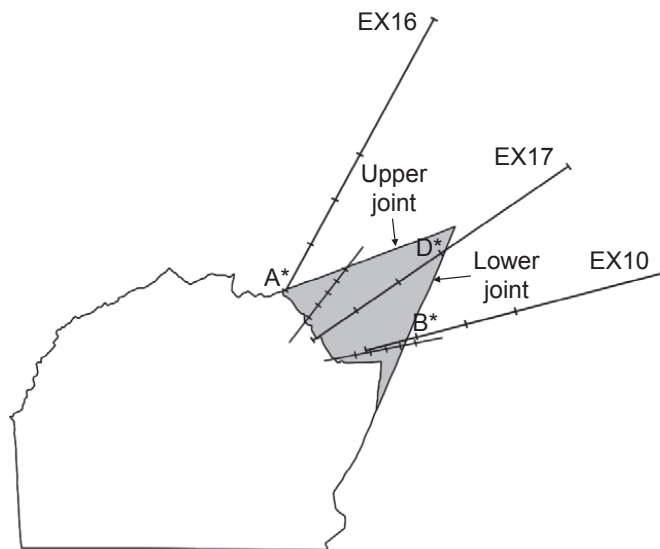
Figure 12 Cross sections R5 of the test drift showing a wedge in the footwall side of the drift. *Extensometer-anchor near intersected joint.

3.5 Arlandabanan

The Arlandabanan is a railroad connecting the Arlanda airport and the city of Stockholm. The Arlandabanan starts with a tunnel constructed beneath the Arlanda airport. The Arlandabanan tunnel consists of three underground stations: (i) two stations (Shuttle station), and (ii) one station (Intercity Station). The Shuttle station 2 was 155 m long and the span 23 m. The overburden was between 8 to 13 m. The excavation technique was drilling-and-blasting, and

shotcrete and bolts were used for rock reinforcement. The rock mass consists of mica schist and mica gneiss. Joint mapping was conducted, and deformations were measured. Two large structures were encountered (pegmatite dyke and clay gouge). The structures strike between 10° and 20° to the tunnel axis and dip about 70°. The Shuttle station was excavated in two stages (two pilot tunnels followed by pillar removal). The stress state in the Shuttle station was determined using three dimensional overcoring measurements. The rock properties as well as the field stresses for Shuttle station 2 are presented by Töyrä (2006). No major instability problems occurred during excavation (Töyrä, 2006).

3.6   Heathrow tunnel collapse

In October 1994 a section of the tunnel being constructed at Heathrow Airport collapsed. There were no injuries, but many people were put at risk and the consequential cost was significant. The tunnel was constructed using the New Austrian Tunnelling Method (NATM). It was the first time that the NATM was used in London clay, which is the principal clay layer in the London basin. The method involved the use of a sprayed concrete lining which was applied in stages. According to Lance (2008) there were no stress measurements carried out in the ground before construction and the *in situ* state of stress was modelled using ground strength parameters derived from sample testing and using ground models appropriate for London clay (i.e. Cam Clay model) and Finite Element Analysis (FEA). According to Anderson (2000) the collapse involved three surface craters and occurred over a number of days and the buildings over the tunnels slowly collapsed and were demolished. The Cambourne house suffered settlement by up to 3 m and the whole building had to be demolished. The last collapse was remote from the first collapse and at about chainage 54 m where the concourse tunnel had been repaired during August. There were two main monitoring stations (MMS) at CTA by the time of the collapse. The extensometer 6 on MMS II was placed close to the centre of the collapse.

The cause of the tunnel collapse as a chain of events, cited in the Health and Safety Executive (HSE) report (2000), involved "(i) substandard construction in the initial length of the Central Terminal Area (CTA) concourse tunnel, (ii) jack grouting that damaged the same length of the CTA tunnel plus inadequately executed repairs, (iii) construction of a parallel tunnel in failing ground, and (iv) major structural failure and progressive failure in the adjacent ground along with further badly executed repairs during October 1994".

3.7   Äspö Pillar Stability Experiment

The Äspö Hard Rock Laboratory is situated outside Oskarshamn in southern Sweden. The Swedish Nuclear Fuel and Waste Management Co (SKB) conducted the Äspö Pillar Stability Experiment (APSE) to examine the brittle failure process in a heterogeneous and fractured rock mass when subjected to excavation-induced and thermal-induced stresses. The APSE layout consisted of two large deposition holes (1.75 m diameter and 6.5 m high) and a 1 m wide pillar between these two boreholes. The test site was located beneath a tunnel excavated for the experiment. Acoustic emission (AE), displacement and thermal monitoring systems were used to follow the spalling failure of the pillar as the temperature was increased. Electrical heaters were used to induce spalling failure on the pillar wall of the second hole. The spalling failure propagated downward along the pillar wall and created a v-shaped notch. The first hole was pressurized with water before the beginning of the excavation of the second hole. Spalling failure initiated in the upper part of the second hole due to the excavation induced stresses.

The spalling surface propagated down the hole from 0.5 m to 2 m depth beneath the tunnel floor. The damaged rock was removed and the notch was studied (Andersson 2007).

Spalling occurred at the position of the highest tangential stress, i.e. close to the centre of the pillar. The effect of the confining pressure was obvious when the excavation of the second hole started. The AE events were recorded in the second hole, but not in the first hole. The spalling of the rock was monitored by the AE system as the v-shaped notch propagated down the second hole wall. AE provided a good approximation of the general spalling rate in the pillar, but could not be correlated to the amount of damage to the rock, nor to monitored displacements. At the end of the experiment, damaged rock was removed and the extent of the failure was studied. The majority of the fracturing was initiated and propagated in extension and some evidence of shearing was found at the deepest part of the notch. The temperature increase in the pillar was stopped and a steady state was reached when the notch had propagated close to the bottom of the second hole. The confining pressure was then gradually released. The previously confined hole was unaffected by the removal of the confinement pressure (Andersson 2007).

3.8 Mine-by Experiment

The Mine-by Experiment (MBE) was conducted at the Underground Research Laboratory (URL) of the Atomic Energy of Canada Limited's (AECL's). The MBE was carried out at the 420 m level in massive granite. It was conducted between 1989 and 1995 to study the failure processes due to excavation induced stresses and the progressive failure around an underground opening subjected to high stresses. The test tunnel in MBE was 3.5 m in diameter and 46 m long. The tunnel was excavated using a non-explosive hydraulic rock-splitting technique, and advanced in 1 m rounds sub-parallel to the intermediate principal stress direction to promote rock mass failure. The complete response of the rock mass and the effects ahead of the tunnel face were monitored with a large amount of instruments.

Installation of instrumentation before the excavation made it possible to monitor the complete excavation-induced mechanical response of the rock mass around the tunnel, i.e., including the deformation and failure process ahead of the advancing tunnel face. The instrumentation comprised extensometers and convergence arrays, triaxial strain cells, thermistors to measure temperature, and an acoustic emission/microseismic (AE/MS) technology to monitor the development of the damage zone around the Mine-by Experiment test tunnel. The spalling in the roof and floor of the test tunnel started immediately after each round was excavated. The spalling progressed as the tunnel face advanced. The spalling thickness varied between a few millimetres and 100 mm. The notch development involved four stages (i) damage initiation, (ii) dilation, (iii) spalling, and (iv) stabilization as shown in Figure 13. For more details of the development of the failure process in this case the reader is referred to among others Read (1994), Martin (1997) and Read (2004). Extensometers were installed prior to the start of the excavation, hence the response of the rock mass represents the total displacement induced by the excavation of MBE within the radial coverage area of the extensometers (Read, 2004).
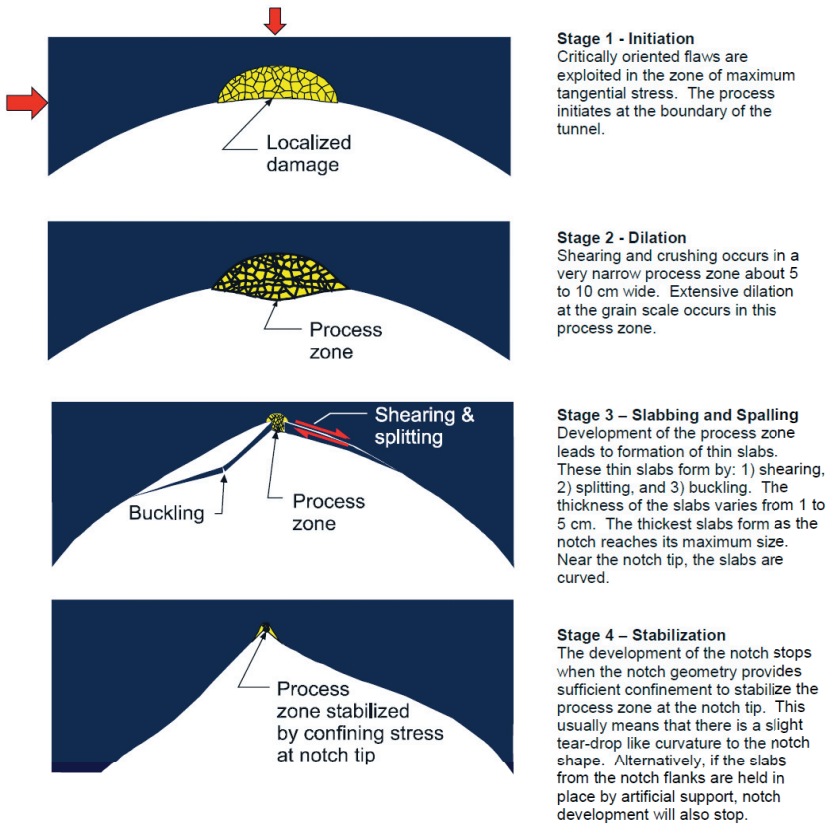
Figure 13 Progressive failure process observed in the MBE test tunnel (Read 2004).

3.9 Summary

The Garpenberg raise and Zinkgruvan exploration drift cases were used in this doctoral work to evaluate spalling failure using numerical analysis, see Pérez Hidalgo and Nordlund (2012) (Paper B). In the numerical analysis, deformation associated with the failure process around the opening of these excavations was also calculated. Bending and shear failure were evaluated using deformation measurement data from the Kristineberg stope as presented in Pérez Hidalgo and Nordlund (2013b) (Paper C). The Kiirunavaara drift case was used to study the stability of a wedge in 2D and 3D numerical analysis as presented in Pérez Hidalgo and Nordlund (2011, 2013c) (Paper D, Paper E), respectively. The Arlandabanan is a good case with monitoring of displacement in various sections along the station during the construction of the station, but failure did not occur; hence it was not studied further in this thesis. The Heathrow tunnel collapse is a good example of a collapse of an excavation with large dimensions and which caused severe economic consequences, but it was not considered for analysis since the tunnel was mainly constructed in soil. The APSE project provided valuable information about spalling failure and stress criterion for spalling since the experiment predicted where spalling occurred based on stress orientations, but this case was not used further in this doctoral work. The

spalling failure in MBE was not investigated further in this work because this case is very well known and it has been well investigated by many other researchers, e.g., Read (1994), Martin (1997), Cai et al., (2001), Read (2004).

The failure process of the spalling in MBE certainly provided a proper understanding of the response/movement (induced by the excavation of the test tunnel) of the rock around the tunnel, which was used to improve the understanding of the spalling failure of the Garpenberg raise and of the Zinkgruvan exploration drift. Simulation of the failure process of the spalling in MBE also gave some ideas on how to conduct numerical analysis of the failure occurring around the openings in the Garpenberg raise, in the Zinkgruvan exploration drift, and in the Kiirunavaara drift.

4   DEFORMATION DURING SPALLING FAILURE

In this chapter, spalling failure typical of hard rock mass is addressed. Failure and deformation data from several laboratory tested Fennoscandian rock types, and underground cases such as the Garpenberg raise and the Zinkgruvan exploration drift were used to evaluate the deformation behaviour of spalling failure.

4.1   Laboratory tests

Two groups of laboratory tests were evaluated. These tests were performed on hard Fennoscandian rock types. One group of laboratory tests was performed by the CompLab at LTU (Carlsson 2010; Carlsson and Nordlund 2013(a,b); Carlsson et al., 1999). The other group of laboratory tests was commissioned by Posiva Oy and performed by the Laboratory of Rock Engineering (LRE) at Helsinki University of Technology (HUT) (Eloranta and Hakala 1998, 1999a,b; Hakala and Heikkilä 1997a,b; Heikkilä and Hakala 1998a,b). No laboratory tests were carried out by the author of this thesis.

The tests carried out at LTU and at HUT followed the method suggested by the International Society for Rock Mechanics (ISRM) (Brown, 1981). Since the objective of the LTU tests was to compare the failure behaviour of different rock types of different origin, mineral content and texture, the specimens were collected from different sources (quarry blocks and investigation cores) and the tests were carried out under dry conditions. The tests were performed using a servo-hydraulic 4500 kN testing machine (Instron H0092 with a Dartec control system 9500 at Complab, LTU). The loading rate was 0.72 MPa/s. The Posiva Oy tests were intended to be carried out under conditions representative for the in situ conditions; hence, the specimens were handled to preserve the natural humidity. For these tests a MTS 815 rock mechanics testing system was used. The loading rate was 0.75 MPa/s.

For the rock types tested at LTU, Young´s modulus (E), and Poisson´s ratio (ν) were measured by using two diametrically opposite pairs of axial and tangential standard strain gauges. Young's modulus and Poisson's ratio were determined using the tangent method at 50% of the peak strength by evaluating the slopes of the stress-strain curves. In the tests carried out by Posiva Oy, the elastic properties were determined as the secant value from the range of -0.01% lateral strain (ε_3) to 50% of peak strength (σ_c). The volumetric strain (ε_v) and crack volumetric strains (ε_{crv}) were calculated in both groups of laboratory tests using the following equations:

$$\varepsilon_v = \varepsilon_1 + 2\varepsilon_3 \tag{15}$$

$$\varepsilon_{crv} = \varepsilon_v - \varepsilon_{ve} \tag{16}$$

$$\varepsilon_{ve} = \frac{1-2\nu}{E}\sigma_a \tag{17}$$

where, ε_v is the volumetric strain, ε_1 is the axial strain, ε_3 is the lateral strain, ε_{crv} is the crack volumetric strain, ε_{ve} is the elastic volumetric strain, ν is the Poisson's ratio, E is the Young's modulus, and σ_a is the axial stress.

According to Eloranta and Hakala (1998, 1999a,b), Hakala and Heikkilä (1997a,b), Heikkilä and Hakala (1998a,b) the crack initiation (*ci*), crack damage (*cd*) and peak strength (*cp*) stages were identified following the methodology suggested by Martin and Chandler (1994) for the tests carried out by Posiva Oy. The peak strength stage (i) is defined as the highest observed axial stress on the stress-strain curve, and the crack damage stage (ii) is defined as the reversal of the volumetric strain (ε_v) curve. The transition from stage (i) to stage (ii) represents the transition from compaction to dilation, whereas the crack initiation stage (iii) is defined as the stress level where the crack volumetric strain (ε_{crv}) deviates from zero. This doctoral work identified these stages for the LTU rock types following the same methodology. Eberhardt et al. (1998) used the normalized stress required to separate one stage of crack growth from another. Normalized quantities were also used in this study as shown in Table 4. The normalized quantity is calculated by dividing the absolute quantity value by its peak strength value.

Table 4 Failure-deformation process quantities, and normalized quantities evaluated in this paper.

Deformation stage	Absolute quantity			Normalized quantity	
	ci	*cd*	*p*	*ci*	*cd*
Axial stress [%]	σ_{1ci}	σ_{1cd}	σ_{1p}	σ_{1ci}/σ_{1p}	σ_{1cd}/σ_{1p}
Axial strain [%]	ε_{1ci}	ε_{1cd}	ε_{1p}	$\varepsilon_{1ci}/\varepsilon_{1p}$	$\varepsilon_{1cd}/\varepsilon_{1p}$
Lateral strain [%]	ε_{3ci}	ε_{3cd}	ε_{3p}	$\varepsilon_{3ci}/\varepsilon_{3p}$	$\varepsilon_{3cd}/\varepsilon_{3p}$
Crack volumetric strain [%]	$\varepsilon_{crv\text{-}ci}$	-	-	-	-
Volumetric strain [%]	-	$\varepsilon_{v\text{-}cd}$	-	-	-

4.1.1 Tested rock types

9 different types of rock (26 specimens in total) were tested at LTU as shown in Table 5. All specimens had a diameter of 42 mm and a length of 105 mm. The Posiva Oy rock types are shown in Table 5, including 6 types of rock (69 specimens in total). The diameter of these rock specimens was 62 mm and the length varied between 153 and 156 mm. 95 specimens were tested in total. The peak strength for these rock types is shown in Figure 14.

Table 5 Rocks tested at LTU (Carlsson and Nordlund 2013(a,b); Carlsson et al. 1999) and at HUT (commissioned by Posiva Oy) (Eloranta and Hakala 1998, 1999a,b; Hakala and Heikkilä 1997a,b; Heikkilä and Hakala 1998a,b).

Rocks tested at LTU	Site (Sweden)	26 Specimens
Limestone	Unknown	6
Quartzite[a]	Unknown	2
Diorite[b]	Äspö	3
Granite[a]	Kuru (Finland)	1
Norite[a]	Högsma-Skåne	4
Gabbro[a]	Kallax	3
Diabase[a]	Hägghult	2
Diabase[b]	Gudmundberget	3
Trachyte[b,c]	Kiirunavaara mine	2
Rocks tested at HUT	Site (Finland)	69 Specimens
Mica gneiss[b]	Olkiluoto	19
Tonalite gneiss[b]	Romuvaara	10
Granite[b]	Kivetty	10
Porphyritic granodiorite[b]	Kivetty	10
Pyterlite[b]	Hästholmen	10
Equigranular rapakivi granite[b]	Hästholmen	10

[a] These specimens were drilled from quarry blocks.

[b] These specimens were taken from investigation cores.

[c] Internally, within LKAB, designated as syenite porphyry. From now on it will be called syenite porphyry.
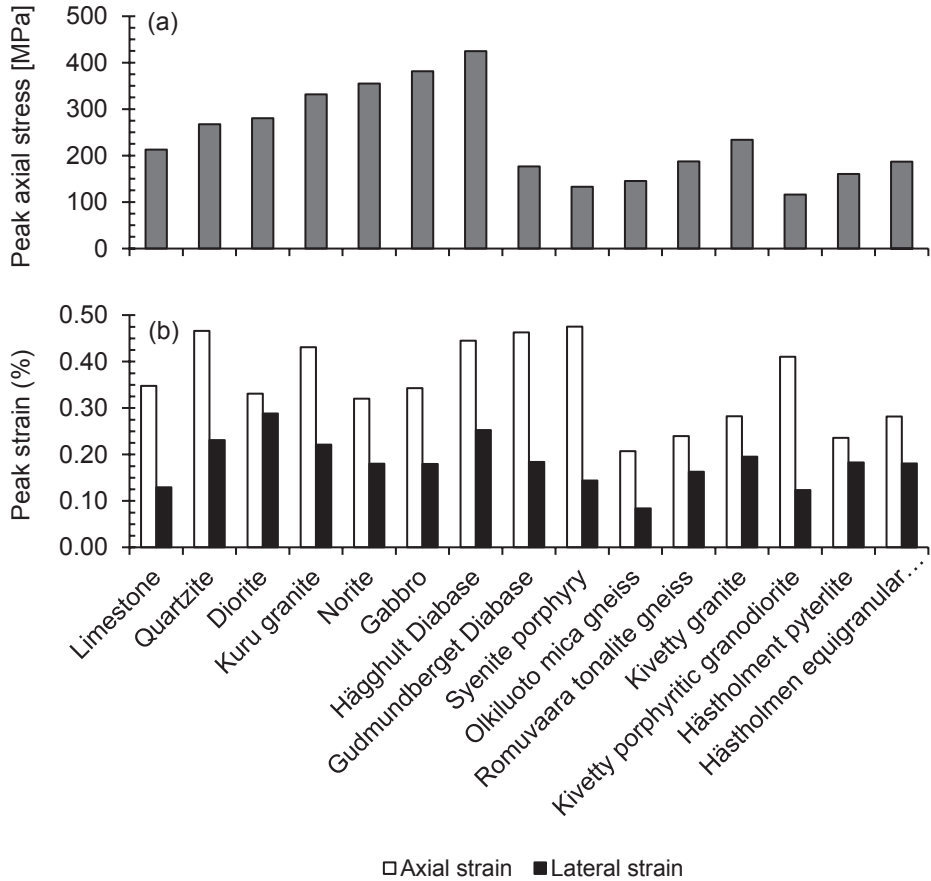
Figure 14 Peak for the (a) axial stress, and (b) axial and lateral strains.

4.1.2 Failure-deformation behaviour

The normalized stress and strain values with respect to their maximum values are presented in Figure 15. The displayed value on the *y-axis* is the mean of the normalized stress and strain quantities which was calculated from all single specimens of the same rock type. The absolute value for the volumetric strains is presented in Figure 16. The scatter for the various strain quantities differed; for example, 2/3 of the mean values of the $\varepsilon_{1cd}/\varepsilon_{1p}$ were within the interval 70-90% while the mean values of this quantity for all rock types were within the interval 60-100%. The scatter of $\varepsilon_{1ci}/\varepsilon_{1p}$ was similar to that of $\varepsilon_{1cd}/\varepsilon_{1p}$, whereas the scatter was considerably larger for the other strain quantities. The volumetric strain mean value is larger than the crack volumetric strain mean value.
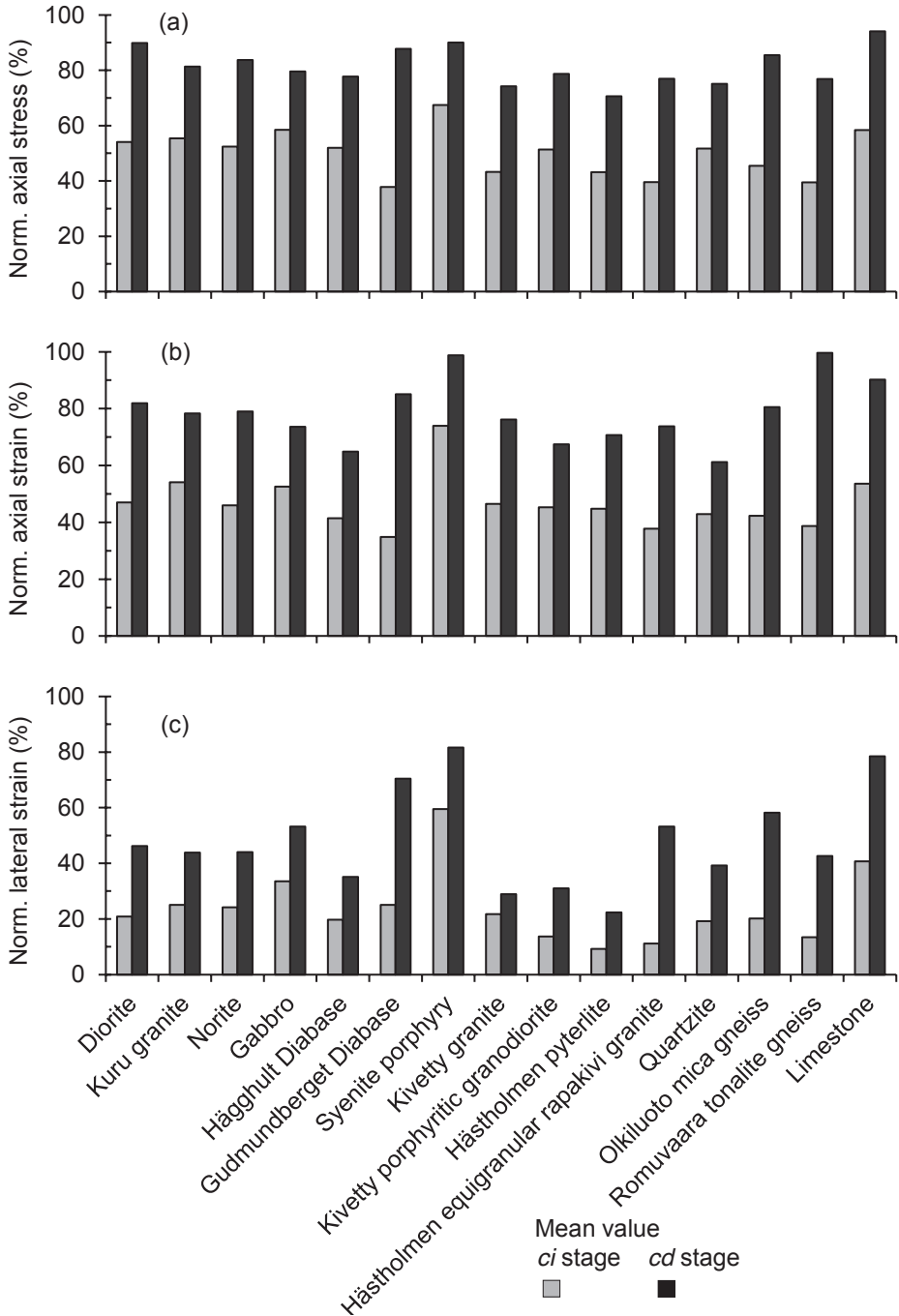
Figure 15 Normalized (a) axial stress, (b) axial strain, and (c) lateral strain mean values at crack initiation and crack damage stages for each rock type.
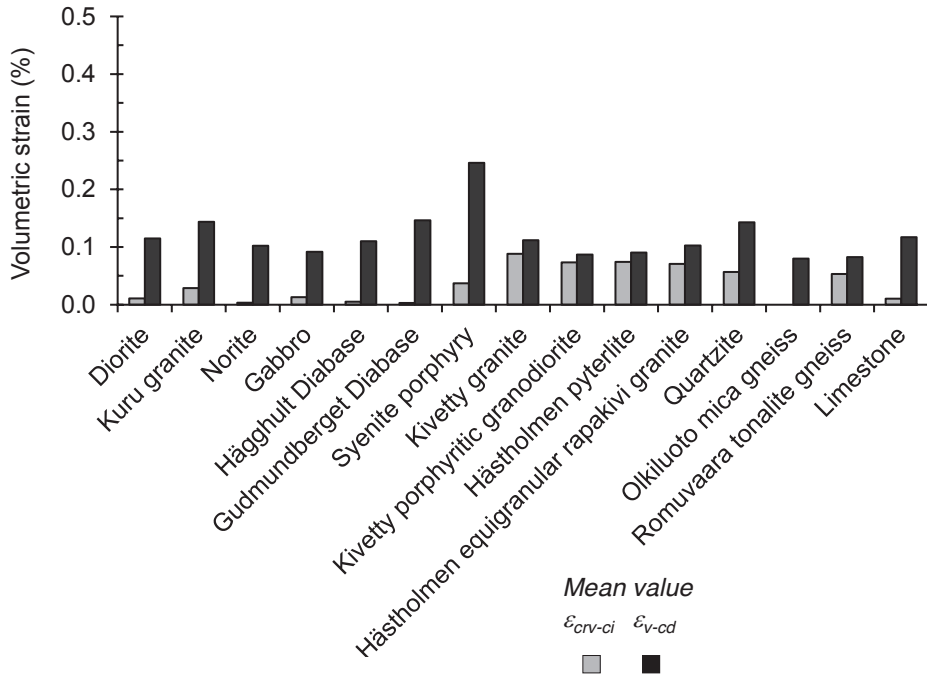
Figure 16 Crack volumetric and volumetric strain mean values.

4.1.3 Failure-deformation and rock characteristics behaviour

Press and Siever (2001) was used as a guide for grouping the specimens according to the grain size and mineral composition as presented in Table 6. According to Table 6, the majority of the tested rock types have medium grain size and contain quartz, mafic minerals and feldspar.

An evaluation of axial stress and strain quantities was performed by comparing the mean of the normalized quantities for each rock characteristic at crack initiation and crack damage stage. This is presented in Figure 17a. The displayed value on the *y-axis* is the mean of the quantity which was calculated from all single specimens of the same rock characteristic. Figure 17a shows that the mean value of the normalized crack damage lateral strain ($\varepsilon_{3cd}/\varepsilon_{3p}$) is strongly influenced by the grain size. This is in line with the findings by Eberhardt et al., (1999) who showed that the effect of grain size was most significant for the crack coalescence and crack damage thresholds. In the present work, the mean value of the examined quantities varies slightly with respect to the mineral composition of the rock. The specimens containing carbonates seems to behave somewhat differently compared to the other rock types.

The evaluation of the crack volumetric and volumetric strain data presented in Figure 17b showed that the mean versus rock characteristics is different for ε_{crv-ci} and for ε_{v-cd}. However, both ε_{crv-ci} and ε_{v-cd} seem to be sensitive to grain size. The variation with respect to the mineral content is more difficult to interpret. The highest values for ε_{crv-ci} were obtained for mafic minerals and feldspar while ε_{v-cd} showed the highest values for carbonates and pyrite.

Table 6 Rock type characteristics (grain size and mineral composition) using description data from Carlsson (2010), Carlsson and Nordlund (2013a,b), Carlsson et al., (1999), Eloranta and Hakala (1998,999a,b), Hakala and Heikkilä (1997a,b), Heikkilä and Hakala (1998a,b).

Rock type	Grain size			Mineral composition						
	1	2	3	4	5	6	7	8	9	10
Limestone	*			*						
Quartzite	*							*		*
Diorite		*						*		*
Kuru granite		*						*	*	*
Norite		*			*	*	*		*	*
Gabbro		*					*		*	*
Hägghult Diabase		*			*	*	*		*	*
Gudmundberget Diabase		*				*	*		*	*
Syenite porphyry			*					*[a]	*	*
Olkiluoto mica gneiss	*							*	*	*
Romuvaara tonalite gneiss		*						*	*	*
Kivetty granite			*					*	*	*
Kivetty porphyritic granodiorite			*					*	*	*
Hästholmen pyterlite		*						*		*
Hästholmen equigranular rapakivi granite		*						*	*	*

1-fine, 2-medium, 3-coarse, 4-carbonates, 5-apatite, 6-pyrite, 7-magnetite ilmenite, 8-quartz, 9-mafic minerals (mica, biotite, pyroxene+amphybole, phlogopite, and hornblende), 10-feldspar (K-feldspar and plagioclase).

[a] Minor content.
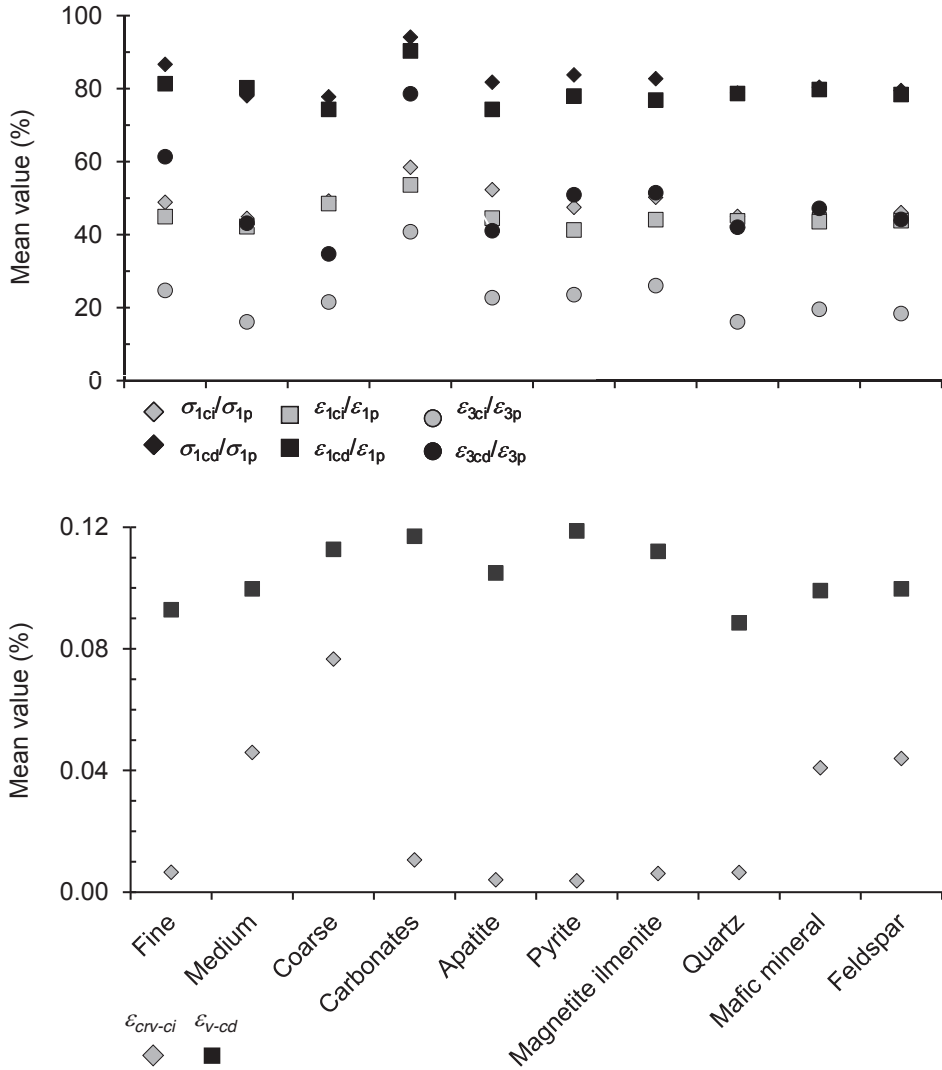
Figure 17 Mean value of the (a) normalized, and (b) volumetric strain quantities for each rock characteristic at crack initiation and crack damage stages.

4.2 Garpenberg raise and Zinkgruvan exploration drift models

In this sub-chapter the failure-deformation behaviour of spalling failure in the Garpenberg raise and the Zinkgruvan exploration drift are presented. Numerical analysis was used to model spalling failure and calculate deformation quantities in the zone of failure. The study first attempted to evaluate the spalling failure without the aid of the laboratory test data.

Subsequently, the failure was also evaluated by using the laboratory test data as a means to estimate the location of potential failure surfaces.

4.2.1 Model setup and input data

The analysis was conducted using *Phase2*, a two-dimensional finite element program (Rocscience, 2009). This program was chosen because it is easy to use and widely applied to mining and geotechnical problems. The two modelled cases were a raise in the Garpenberg mine, and an exploration drift at depth in the Zinkgruvan mine, both based on information provided in Edelbro (2008). The Garpenberg raise case was analysed using a linear-elastic and a linear-elastic brittle plastic material model. The Zinkgruvan drift case was analysed using a linear-elastic and a linear-elastic perfectly plastic material model. The Garpenberg raise model developed by Edelbro (2008) was used for this work but evaluated differently, focusing on the strain for the observed spalling failure. For the Zinkgruvan drift case, a new model was built.

The discretization used in the Garpenberg raise model is shown in Figure 18a, which includes an area with smaller zones in the region of expected failure, compared to the rest of the model. Input data for the model is presented in Table 7. This table shows that a Cohesion Softening Friction Hardening (CSFH) material model was used, which means that the initial (peak) friction angle is lower, and then undergoes hardening to the final (residual) and higher friction angle.

For the Zinkgruvan exploration drift model, the zone length adjacent to the test drift was smaller compared to the rest of the model as illustrated in Figure 18b. The virgin stress state and rock mass properties correspond to those presented by Edelbro, (2008). Two cases with different orientation of the virgin horizontal principal stresses were analysed for the Zinkgruvan case (Figure 19): (i) major horizontal stress perpendicular to the drift, and (ii) minor horizontal stress perpendicular to the drift.

In the Zinkgruvan drift model the program RocLab (Rocscience, 2007) was used to estimate the Mohr-Coulomb strength parameters cohesion (c=8.3 MPa), friction angle (ϕ=58.3°), and tensile strength (σ_t=1.4 MPa) using the Hoek-Brown parameters, intact uniaxial compressive strength (σ_{ci}), Geological Strength Index (*GSI*), intact rock parameter (*mi*), and disturbance factor (*D*) as input. The confining stress (σ_{3max}) was determined by conducting a linear elastic stress analysis of the drift. The corner effects were omitted. This analysis revealed that the maximum value of σ_3 within the area where spalling failure occurred was in the interval of 0-10 MPa. Therefore, σ_{3max} was selected to be 10 MPa. The value of (i) σ_{ci}=160-300 MPa,　(ii) *GSI*=70-82, (iii) *mi*=25, and (iv) Young's modulus, *E*=71 GPa were taken from Edelbro (2008). The *D* value corresponds to an excellent quality controlled blasting.

The dilation angle (ψ) is required as input to a plastic material model. The dilation angle was defined based on a preliminary analysis where it was varied between high and low values. A sensitivity study was carried out which showed that the depth of the potential boundary of the spalling zone in the roof was dependent on the magnitude of the dilation angle. When a high dilation angle (1/3 to 2/3 of the friction angle) as proposed by Rocscience (2009) was used, the spalling zone no longer formed – which did not agree with actual observations. However, for low dilation angles (around zero) the depth of this zone increased and it was more obvious and distinct. Therefore, a dilation angle of 0° (non-associative flow rule) was used. Similar findings were also stated by Edelbro (2008).
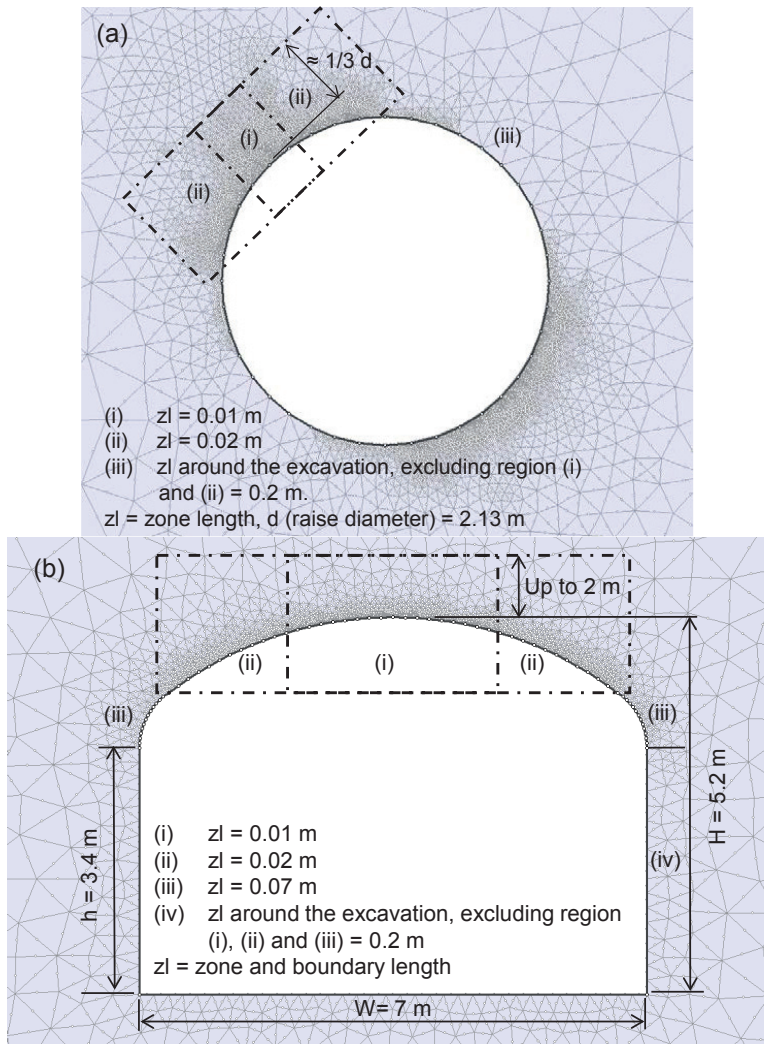
Figure 18 Close up model of the (a) raise of Garpenberg mine, and (b) Zinkgruvan drift showing zone lengths used in *Phase2*.

Table 7 Phase2 input data for the raise of Garpenberg mine model (Edelbro, 2008).

Property	Value
Cohesion peak, c_{peak}	20.7 MPa
Cohesion residual, c_{res}	2.88 MPa
Friction angle peak, ϕ_{peak}	10°
Friction angle residual, ϕ_{res}	46.9°
Tensile strength, σ_t	2.26 MPa
Dilation angle, ψ	0°

$\sigma_v = 28$ MPa

⇓

Not to scale

⇐ Case 1:$\sigma_H = 68$ MPa
Case 2: $\sigma_h = 47$ MPa

Out -of plane
Case 1: $\sigma_h = 47$ MPa
Case 2: $\sigma_H = 68$ MPa
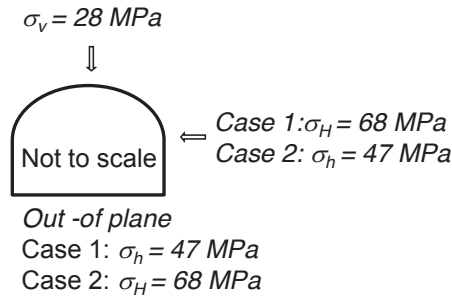
Figure 19 Stress state cases for the Zinkgruvan drift case model.

4.2.2 Spalling failure

In this work, both volumetric strain and maximum shear strain were used as indicators of a failure surface, i.e., spalling failure. The failure surface is formed when (i) two continuous strain bands intersect each other and the excavation boundary, or (ii) if one continuous shear band which starts and ends at the boundary is formed. The spalling failure of the rock is a progressive process that ends up in a final form that is most often notch shaped.

Strain bands are observed in the walls of the raise using both indicators, thus showing the potential boundary of the calculated spalling failure formed in the wall of the raise. Volumetric strain bands are distinguished, but they are discontinuous. For the maximum shear strain, several distinguished and continuous bands intersect and form triangular failure zones as shown in Figure 20a for the Garpenberg raise model. A line perpendicular to the boundary was defined within the failure zone in order to collect data of volumetric strain and maximum shear strain and thus to calculate the major and minor principal strains. This line was assumed to intersect the failure zone from the excavation boundary to a point far away from the zone.

For the Zinkgruvan exploration drift model, bands of volumetric strain and maximum shear strain concentration were modelled for each stress case ($\sigma_\perp = \sigma_H$ and $\sigma_\perp = \sigma_h$). Figure 20b shows the strain bands for the worst stress case scenario, $\sigma_\perp = \sigma_H$. The indicated failure in the roof is a large and wide arch that covers almost the entire width of the roof region. For the linear-elastic perfectly plastic model the residual strength parameters (cohesion and friction angle) are equal to the peak parameters. This plasticity formulation cannot simulate the effect of slabs

developing parallel to the boundary (Diederichs, 1999). Therefore, the arched failure shape in the Zinkgruvan case is different compared to the notch shape that the brittle material model showed in the Garpenberg raise. There are strain bands intersecting and forming small zones inside the large arched zone of failure. The depth of the observed failure in the roof centre is indicated in every figure, as well as the predicted depth of failure.

(a)

#18   #12
       #6   #4
             #2

— Observed failure depth at:
point #4 = 0.05 m
······· Predicted failure depth at:
Point #2 = 0.02 m
Point #6 = 0.10 m
Point #12 = 0.22 m

(b)

$\sigma_{\perp} = \sigma_H$

(b)
(a)

(a)   Observed failure depth: 0.1-0.2 m
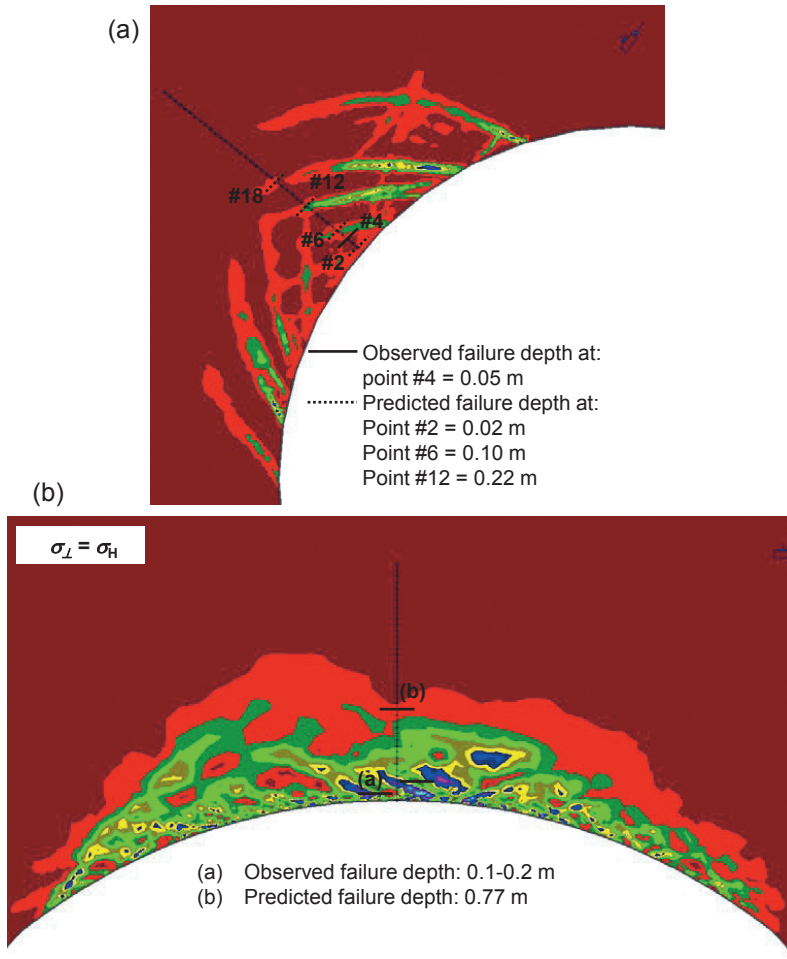(b)   Predicted failure depth: 0.77 m

Figure 20 (a) Maximum shear strain bands in the wall of the Garpenberg raise calculated using a linear-elastic brittle plastic material model, and (b) maximum shear strain bands in the roof of the Zinkgruvan drift calculated using a linear-elastic perfectly plastic material model for stress case $\sigma_{\perp} = \sigma_H$.

4.2.3 Failure-deformation behaviour

For the Garpenberg raise model, the major and minor principal strains, volumetric strain and maximum shear strain were calculated. These quantities were plotted versus the distance from the raise boundary as shown in Figure 21 for the elastic brittle material model. For the linear-elastic material model the quantities decay smoothly with increasing distance from the raise boundary. The linear-elastic material model plots and other details can be found in Pérez Hidalgo and Nordlund (2012) (Paper B). For the linear-elastic brittle plastic material models, localized failure occurs at different distances from the boundary. The major principal strain and the maximum shear strain had local maxima while the minor principal strain had local minima at the mentioned depths. The volumetric strain reached a local maximum at the mentioned depths, except at 0.02 m and 0.33 m from the boundary. The location of the calculated extreme values of the strain quantities do to, some extent, correspond to the observed spalling failure depth as indicated in Figure 20a. The strain magnitudes are lower immediately after 0.22 m distance from the boundary. This corresponds to a discontinuous strain band located at point #18 as shown in Figure 20a.

Figure 21 Major and minor principal strain, volumetric strain and maximum shear strain calculated using a linear-elastic brittle plastic material model for the Garpenberg raise case.

For the Zinkgruvan exploration drift the same quantities were calculated. For the linear-elastic material model the calculated quantities were plotted as functions of the distance from the drift boundary, see Pérez Hidalgo and Nordlund (2012) (Paper B). These strain quantities have large absolute values at the drift boundary, and decrease with the distance. For the linear-elastic perfectly plastic material model the failure development is illustrated in Figure 22. The strains have small absolute values at the boundary and reach their maxima and minima between 0.1 m and 0.2 m depth. Moreover, local maxima are also observed (i) in the interval 0.31-0.36 m and 0.6-0.7 m in Figure 22 for $\sigma_\perp = \sigma_H$, and (ii) at 0.05 m (for $\sigma_\perp = \sigma_h$), from the boundary. These local maxima and minima occurred at discontinuous strain bands as shown in Figure 20b. The strain magnitudes decreased immediately after this region and became constant after approximately 0.8 m depth. The largest strain magnitudes were calculated for the case when the major horizontal stress is perpendicular to the raise ($\sigma_\perp = \sigma_H$).

Although these findings give information about the magnitude of the stress and strain quantities in the zone of spalling failure and the shape of the spalling, they cannot help to describe the failure process of the spalling, i.e., where/when crack initiates and propagates. The modelled results should be compared with the laboratory test data results. This is conducted in the sub-chapter 4.2.4.
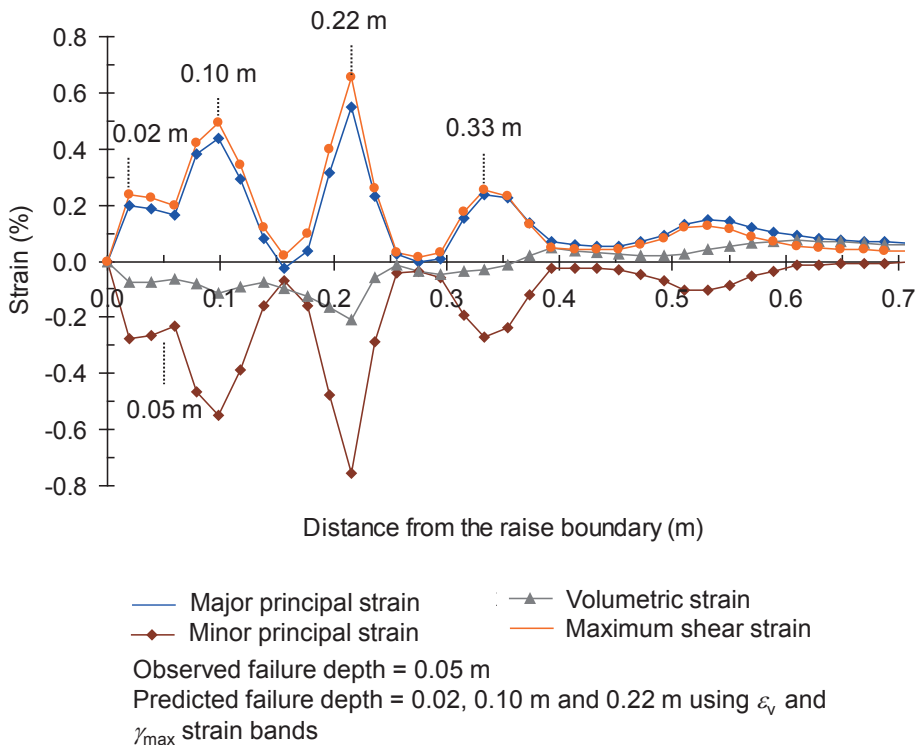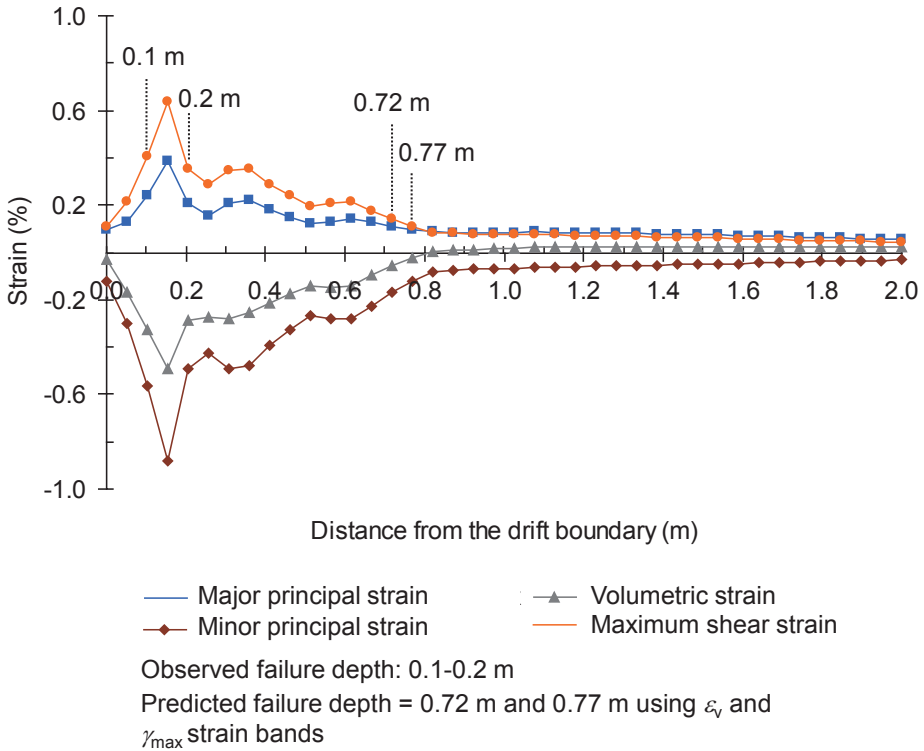
Figure 22 Major and minor principal strain, volumetric strain and maximum shear strain calculated using a linear-elastic perfectly plastic material model for stress case $\sigma_\perp = \sigma_H$ for the Zinkgruvan drift case.

4.2.4 Evaluation of spalling using laboratory tests data

The results from the numerical analysis have been compared to the laboratory test data described in the sub-chapter 4.1, for rock types that are judged to have properties and behaviour similar to those in the modelled cases. The predicted quantities from the modelling were the major principal strain (ε_1), and minor principal strain (ε_3). The measured quantities from the laboratory tests were the axial strains (ε_{1ci}, ε_{1cd}, ε_{1p}), and lateral strains (ε_{3ci}, ε_{3cd}, ε_{3p}). The calculated strains developing around the studied openings are in this section compared with the failure-deformation stages of rocks tested in the laboratory.

From the group of tested rocks, limestone was chosen to represent the rock mass of the Garpenberg raise. However, the behaviour of the tested and the real case limestone may be different. For the linear-elastic material model (see Pérez Hidalgo and Nordlund (2012) (Paper B)) the major principal strain, at the raise boundary and along the whole distance from the boundary, is less than the axial crack initiation strain. Moreover, the minor principal strain at the raise boundary is less than the lateral crack initiation strain. The comparison indicates onset

of stable cracking at the boundary of the raise. The crack damage and peak strength stages were not reached at the raise boundary.

The major and minor principal strains from the numerical analysis with the linear-elastic brittle plastic material model are shown versus distance from the raise boundary in Figure 23. In this figure the axial strain and the lateral strain of the limestone at the crack initiation, crack damage and peak strength stages are also plotted. In this model the major principal strain is greater than, and the minor principal strain is less than, their respective strains within several distances from the boundary around maxima and minima. These distances are shown in Table 8 (column LE-B). This indicates that unstable cracking has developed and fallout volumes can be formed at two or three locations outside the boundary of the opening, corresponding to the maxima and minima identified from Figure 23.

Figure 23 Comparison between the major principal strain and axial strain, and minor principal strain and lateral strain in the Garpenberg raise case using a linear-elastic brittle plastic material model and limestone through laboratory tests at each deformation stage.

Quartz-feldspar leptite is the dominant rock type in the Zinkgruvan exploration drift. Among the rock types in the laboratory tests, quartzite is probably what best matches the rock of the Zinkgruvan drift. Therefore, quartzite was chosen from the laboratory testing to represent the

rock mass of this case. The comparison is presented in Figure 24 for the linear-elastic perfectly plastic material model.

For the linear-elastic material model (see Pérez Hidalgo and Nordlund (2012) (Paper B)) the calculated major principal strain is clearly smaller than the axial strain from the laboratory tests. This indicates that cracking has not yet started. The comparison between the calculated minor principal strain and the lateral strain from laboratory tests shows different results. (i) Unstable cracking is indicated between the boundary and the observed failure depth at 0.02 m, and (ii) stable cracking is inferred from the observed failure depth at 0.02 m to approximately 0.82 m depth. The peak strength stage was not exceeded. For the linear-elastic perfectly plastic material model the calculated major principal strain is greater than, and the minor principal strain is less than their respective axial and lateral strains within several distance intervals from the boundary around maxima and minima as presented in Table 8 (column LE-PP). This indicates that unstable cracking has developed and volumes of rock fallout can develop at two or three different locations, corresponding to the maxima and minima identified from Figure 24. Based on the minor principal strain the peak strength stage is reached at a distance of 0.05 m from the boundary, which is similar to the observed fallout depth at 0.1 m.

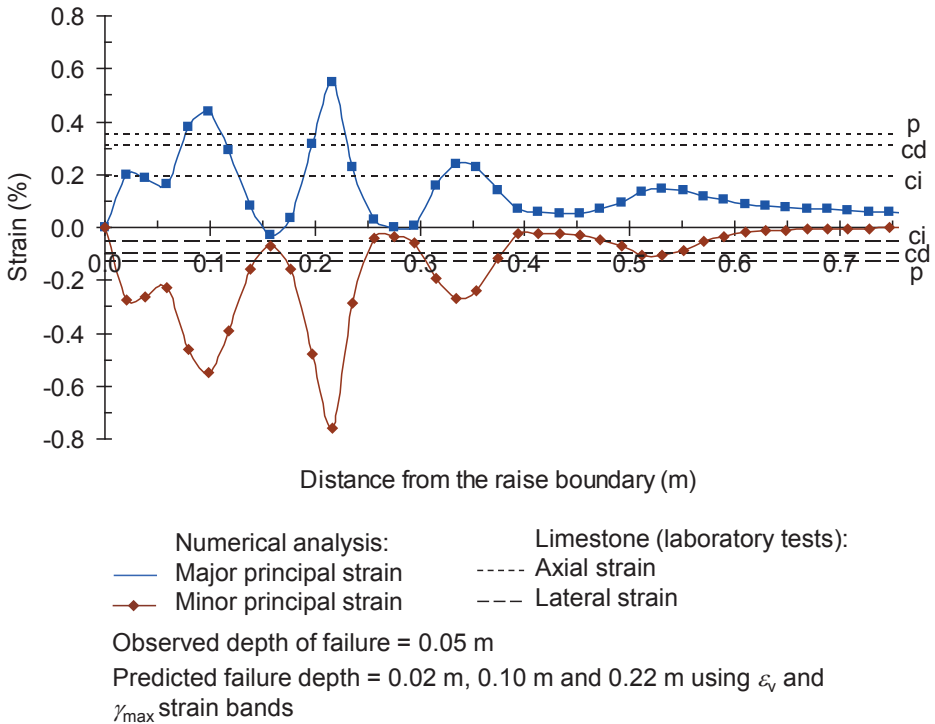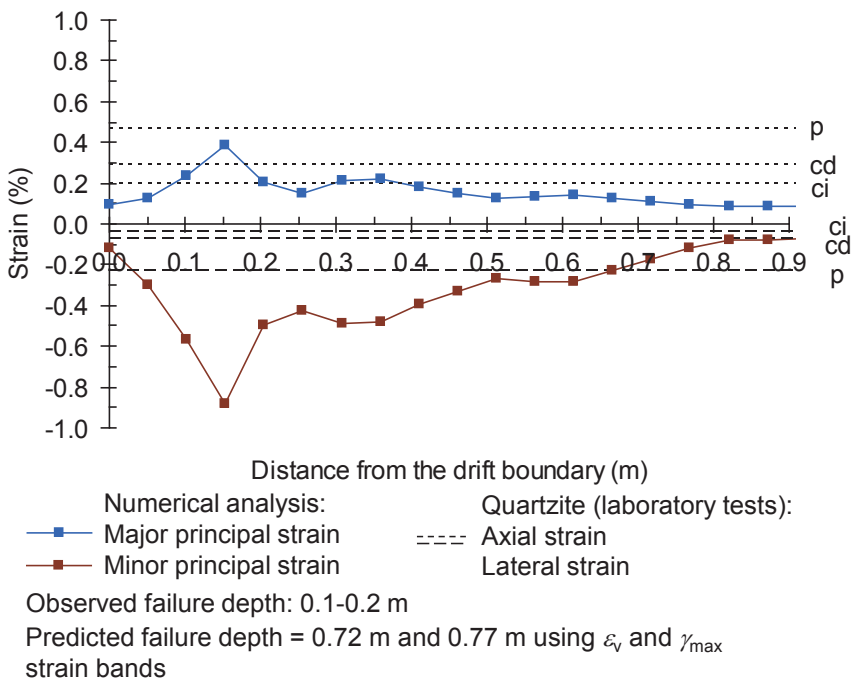
Figure 24 Comparison between the major principal strain and axial strain, and minor principal strain and lateral strain in the Zinkgruvan drift case calculated using a linear-elastic perfectly plastic material model and quartzite through laboratory tests at each deformation stage for stress case $\sigma_\perp = \sigma_H$.

The observed fallout depths for the two cases as well as the calculated distances where the calculated strains (i.e., at crack initiation, crack damage and peak strength stages) became critical are presented in Table 8. This table shows that the major principal strain (ε_1) and the minor principal strain (ε_3) exceeds and is less, respectively, than some of the critical strain levels representing different stages of the failure process (crack initiation, crack damage and peak strength), at several distances from the boundary of the opening. The distances for the strain concentration bands which are closest to the boundary in the plastic analyses (linear-elastic brittle and linear-elastic perfectly plastic material models) are similar to the depth of the observed fallout for both cases. Furthermore, the minor principal strain (ε_3) is less than the lateral critical strain at crack initiation ($\varepsilon_{3ci}/\varepsilon_{3p}$) for the linear elastic model at a distance from the boundary of the opening which is similar to the observed depth of the fallouts in both cases.

Table 8 The observed fallout depths and the distances at which the calculated major and minor principal strains of the rock mass exceed and are less than the critical axial and lateral strains of the intact rock.

Strain comparison	Limestone-Garpenberg raise			Quartzite-Zinkgruvan exploration drift		
	Observed fallout depth [m]	Distance [m]		Observed fallout depth [m]	Distance [m]	
		LE	LE-B		LE	LE-PP
	0.05	-	-	0.10-0.20	-	-
$\varepsilon_1 > \varepsilon_{1ci}$		-	0.02-0.04 0.08-0.12 0.20-0.24 0.33-0.35		-	0.10-0.21 0.31-0.36
$\varepsilon_1 > \varepsilon_{1cd}$		-	0.08-0.10 0.20-0.22		-	0.15
$\varepsilon_1 > \varepsilon_{1p}$		-	0.08-0.10 0.22		-	-
$\varepsilon_3 < \varepsilon_{3ci}$		0-0.04	0.02-0.24 0.30-0.37 0.47-0.57		0-0.87	0-1.90
$\varepsilon_3 < \varepsilon_{3cd}$		-	0.02-0.14 0.18-0.24 0.32-0.37 0.51-0.53		0-0.21	0-1.03
$\varepsilon_3 < \varepsilon_{3p}$		-	0.02-0.14 0.18-0.24 0.32-0.35		-	0.05-0.67

LE = linear-elastic material model, LE-B = linear-elastic brittle plastic material model, LE-PP = linear-elastic perfectly plastic material model.

5 DEFORMATION DURING BENDING AND SHEAR FAILURE

In this chapter, bending and shear failure typical of hard and weak-altered rock mass are studied. Failure and deformation data from a monitored stope in the Kristineberg mine were used to evaluate the failure-deformation behaviour of these failures.

5.1 Deformation monitoring

A schematic view of the conducted deformation monitoring is shown in Figure 25. No measurement was performed for the first two to three rounds closest to the drift entrance. The measurement sections (S1-S10) were located in the middle of each round, and comprised (i) borehole extensometers in the roof and both walls at S3:4 and S6:7, (ii) total station measurements along the stope surface at S3, S3:4, S4, S6, S6:7, and S7, and (iii) tape extensometers between walls at each section. For practical reasons, the tape extensometers were not installed at the same location as the borehole extensometers.

The accumulated deformation of the walls and roof in the monitored stope was increasing with time. Measurements with total stations were recorded in Feb. 17, Feb. 20, Feb. 25, March 01, March 11 and March 25, 2010 for most of the instrumented sections as shown in Table 9. The deformation pattern of the stope is shown in Figure 26 and Figure 27. There are up to sixteen measurement points around the boundary of the stope as illustrated for S3. The direction of the movement as a function of time is indicated with vectors for the measurement point 14 at S3. The vector represents the deformation between two measurement dates, as referred in Table 9. The number of vectors (v_1, v_2, v_3...v_n) vary at each instrumented section. In general, the HW is moving downwards into the opening and the FW is displaying a rotational behaviour. The accumulated convergence measured with tape extensometers between walls increased with time.

Table 9 Time [days][a] when total station measurements started and vectors at each instrumented section.

Monitoring date, year 2010	S3		S3:4		S4		S6		S6:7		S7	
February 17	6		-	-	-	-	-	-	-	-	-	-
February 20	9	v_1	9	-	9	-	-	-	-	-	-	-
February 25	14	v_2	14	v_1	14	v_1	14	-	-	-	-	-
March 01	18	v_3	18	v_2	18	v_2	18	v_1	18	-	18	-
March 11	28	v_4	28	v_3	28	v_3	28	v_2	28	v_1	28	v_1
March 25	42	v_5	42	v_4	42	v_4	42	v_3	42	v_2	42	v_2
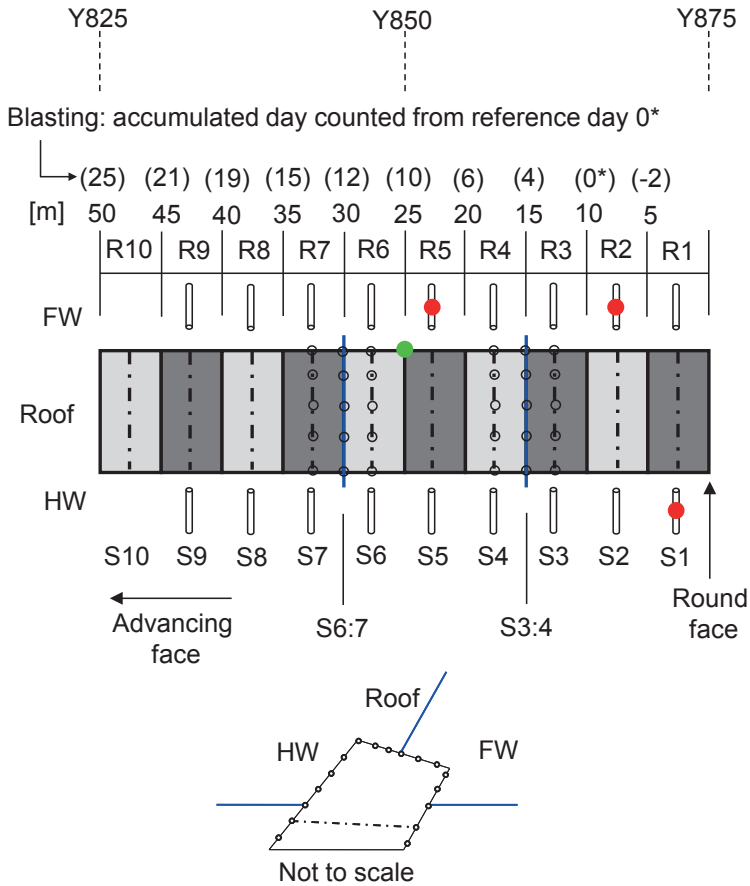
[a] Counted from reference day 0.

Figure 25 Horizontal overview of the monitoring area showing instrumented sections (S1-S10) and instrumentation installation. Note: Blasting day per round is indicated; Reference day 0 (February 11, 2010) is indicated; Day 0 from now on is the reference day for most of the plots presented in this work.
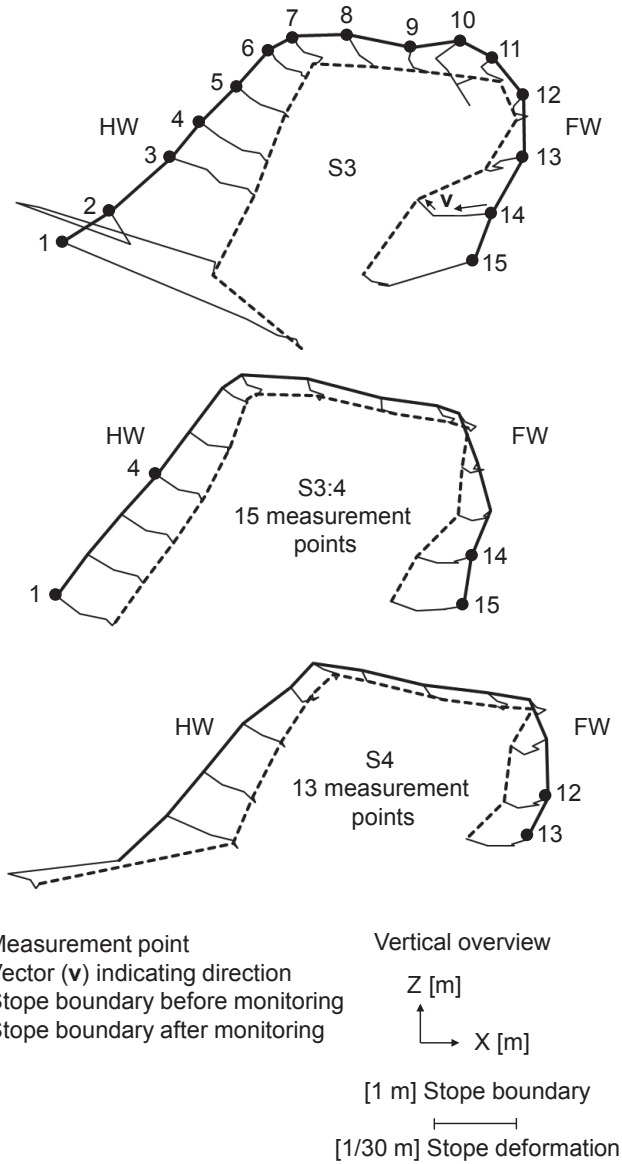
Figure 26 Deformation pattern of the stope at S3, S3:4 and S4 by means of total station measurements. Vectors are illustrated for measurement point 14 at S3.
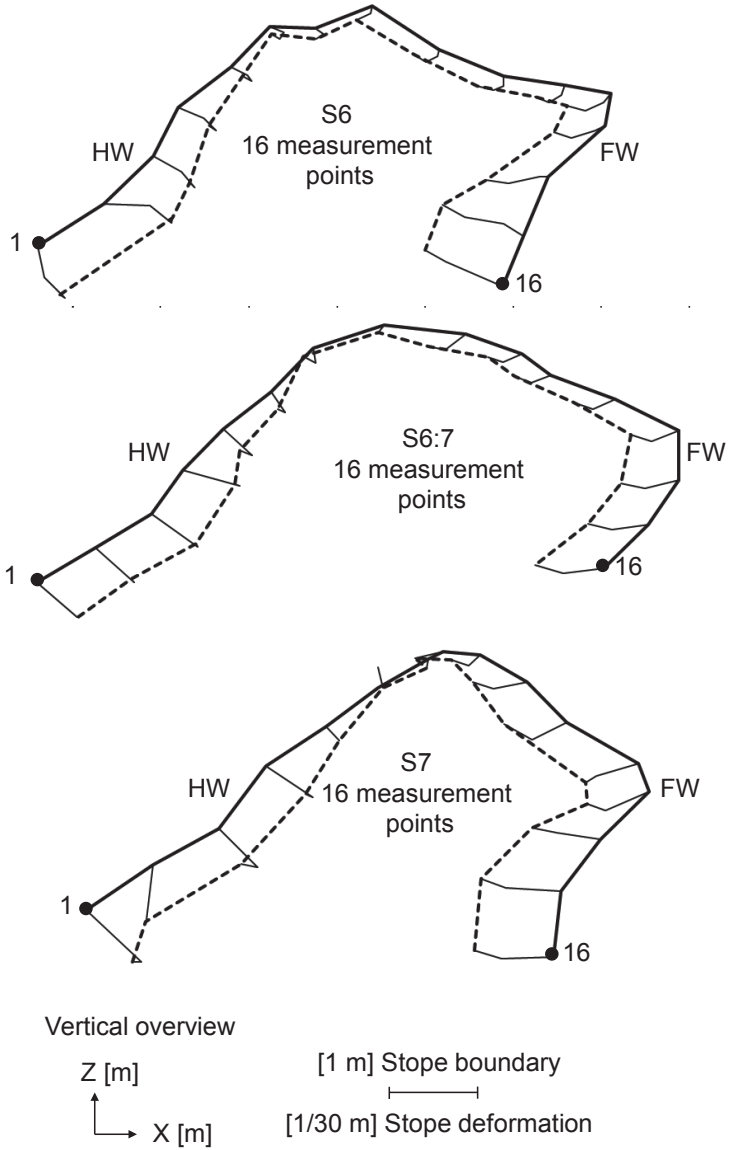
Figure 27 Deformation pattern of the stope at S6, S6:7 and S7 by means of total station measurements.

5.2 Field observations

Borehole camera surveying and surface damage mapping were used to describe the failure of the stope at cut #4. Boreholes of approximately 2.7 m length and 38 mm diameter measured from

the stope boundary were surveyed in 9 sections (BH1-BH9) of the HW and FW, Figure 25. The boreholes were surveyed on February 11, 15, 20, and March 11, 25, 2010 (Table 10). For analysis purposes, February 11 was chosen as a reference day and it was set as equal to Day 0, see Figure 25.

Table 10 Monitoring information related to observed shear failure.

Surveying date [year 2010]	Surveying time [day][a]	BH1-HW	BH2-FW	BH5-FW
February 11	0	Good quality	[b]	-
February 15	4	Good quality	[b]	-
February 20	9	Shear failure	Shear failure[c]	-
March 11	28	Shear failure	Shear failure	Shear failure[d]
March 25	42	Shear failure	Shear failure	Shear failure

[a] Counted from reference day 0, as referred in Figure 25.
[b] Monitoring with tape extensometer starts on day 5.
[c] Borehole camera surveying started this day for BH2-FW.
[d] Borehole camera surveying started this day for BH5-HW.

In the HW side of the stope the quality of the surveyed boreholes was generally good, except for the first 0.75 m of BH1 and BH2, which were fractured and pieces of rocks were found to obstruct the boreholes. Sliding had occurred in BH1 indicating a failure surface (Figure 28a). The shear failure BH1-HW was observed on day 9 as presented in Table 10. In the FW the first seven boreholes (BH1-BH7) were characterized by fracturing with pieces of rock nearly blocking the boreholes. Shear failure was observed in BH2-FW and BH5-FW, see Figure 28b and Figure 28c. The shear failures BH2-FW and BH5-FW were observed on day 9 and day 28, respectively. The quality of BH8 and BH9 was good. The shear displacement was estimated for the three occurrences of shear failure as shown in Figure 28a,b,c. Damage mapping of the FW surface showed that it was characterized by fracturing of the shotcrete. The FW was sliding into the opening between S5 and S6 (Figure 29). The sliding is similar with respect to pattern and shape to the general failure mechanisms of the FW illustrated in Figure 11.

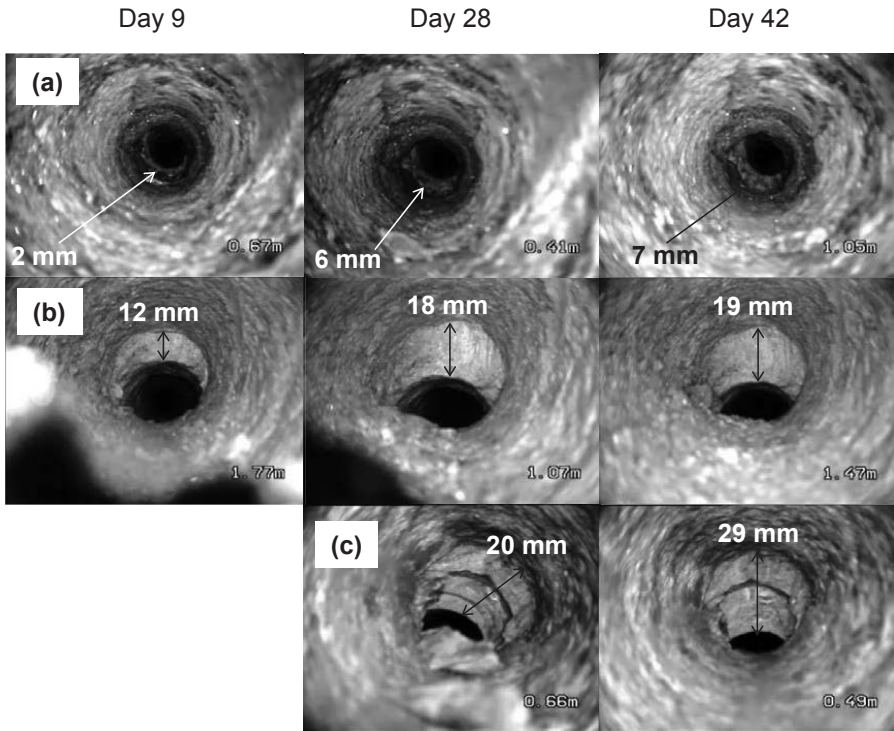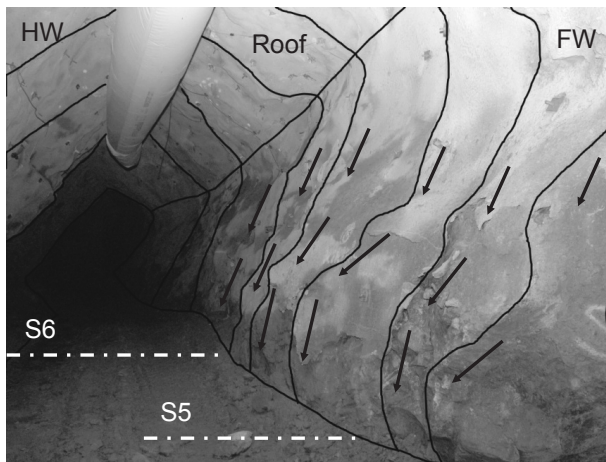Day 9   Day 28   Day 42

Figure 28 Borehole shear failure (a) BH1-HW, (b) BH2-FW, and (c) BH5-FW.

Day 35

Figure 29 Surface shear failure S5:S6-FW.

The convergence between the HW and FW calculated from the tape extensometers at S1, S2 and S5 was used to evaluate the deformation related to the shear failure observed in the boreholes BH1-HW, BH2-FW and BH5-FW, respectively. The convergences at S5 and S6 were used to evaluate the shear failure S5:S6-FW observed on the FW surface between S5 and S6. The convergence related to shear failure is summarized in Table 11.

Table 11 Tape extensometer convergence related to shear failure observed in the boreholes BH1-HW, BH2-FW and BH5-FW, and shear failure S5:S6-FW observed in the FW surface.

Shear failure location	Instrumented section	Shear failure observed [day]	Convergence related shear failure [mm]
BH1-HW	S1	9	44-48
BH2-FW	S2	9	45
BH5-FW	S5	28	56
S5:S6-FW	S5	35	62
S5:S6-FW	S6	35	53

The convergence with respect to time (i.e., the time when each shear failure was observed in the borehole) (see Pérez Hidalgo and Nordlund 2013b (Paper C)) for the shear failure observed in BH1-HW and BH2-FW was similar. It was not possible to see any trend for BH5-FW since the number of measurements was too small. The correlation between the convergences and the onset and subsequent development of the shear failure observed in the borehole BH5-FW and the shear failure S5:S6-FW presented in Table 11 were compared. The convergences for S5 (day 28) and S6 (day 35) were similar. Moreover, the convergence for S5 is greater than that of S6. Hence, it might be assumed that the convergence (62 mm) at S5 was highly influenced by the shear failure, first observed in the borehole BH5-FW and later on the surface of the FW (S5:S6-FW) when the shear surface daylighted. It is therefore assumed in the present work that the shear failure observed in the borehole BH5-FW is the same shear failure as that observed in the FW surface (S5:S6-FW). Further evaluation of the data showed that the shear failure in the boreholes BH2-FW and BH5-FW persisted through time, i.e., sliding continued and the hole was sheared. The shear displacement was larger for BH5-FW than for BH2-FW. Moreover, evaluation of the convergence showed that the convergence was increasing throughout the whole monitoring time.

5.3   Bending and shear failure

Analysis of deformation using total station measurements data was conducted to interpret failure in the HW, FW and roof of the stope.

On the HW side of the stope the failure was not clear from deformation-time plots. To improve the understanding of the behaviour of the HW, plots of deformation versus measurement points from the floor to the abutment of the HW were evaluated. Bending was observed in the instrumented sections S3:4-HW, S6-HW and S6:7-HW. Measurement point 2 in S3 behaved in an unexpected way, cf. Figure 26. This was because it was damaged between measurements no. 1 and 2. The typical bending failure behaviour in the HW is represented by S3:4-HW in Figure 30. Bending took place at S3:4-HW, but the onset was not possible to detect since the time

between two subsequent measurements were too long. For S6-HW and S6:7-HW, the bending behaviour was similar in pattern and deformation magnitude. Measurement points located in the central part of the HW, between the abutment and the floor, showed the largest movement.
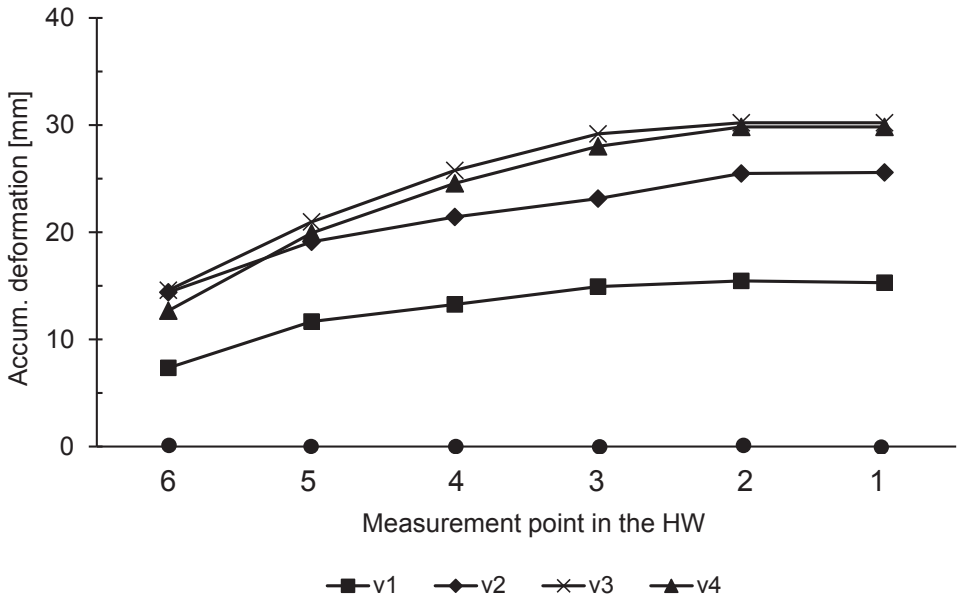
Figure 30 Total station deformations with respect to measurement points from the abutment to the floor for S3:4-HW.

Deformation versus time plots clearly indicated shear failure in the instrumented sections S3-FW, S3:4-FW, S4-FW and S6-FW, i.e., the footwall was sliding into the opening along a shear surface. The deformation versus time behaviour in the FW is illustrated by S3-FW, see Figure 31. For S3-FW, a deformation of 38 mm was registered very early (around day 9, vector v_1) at measurement point 15. The deformation versus time plots for S3:4-FW and S4-FW were similar. The shear failure in both sections developed almost immediately. The deformation for S6-FW continuously developed during the whole monitoring campaign. The deformation related to the shear failure is presented in Table 12.
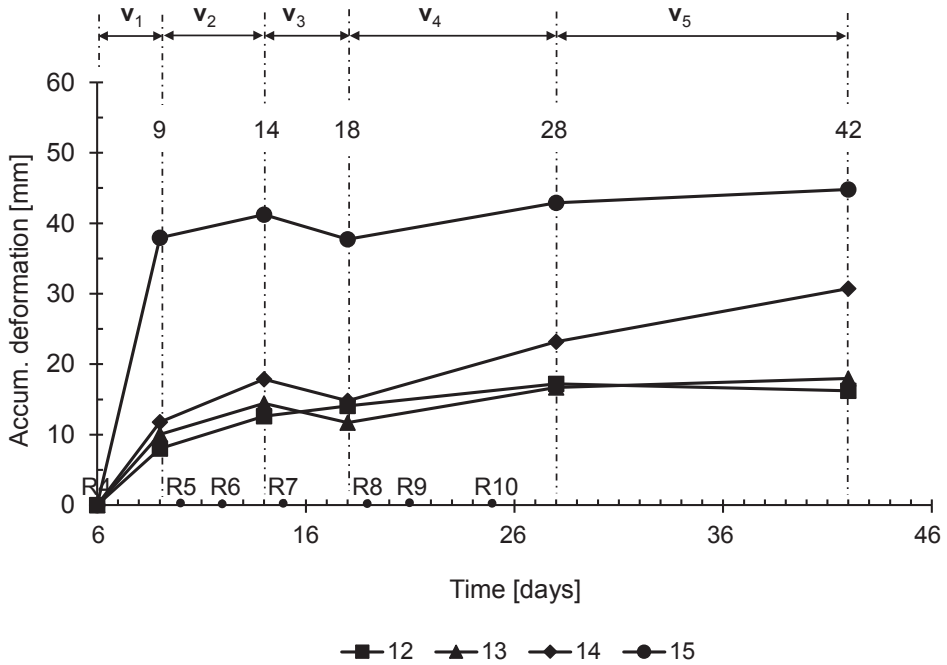
Figure 31 Total station deformations with respect to time for S3-FW. Note: Reference day 0 applies to this figure

Table 12 Information related to shear failure in the FW of the stope.

Instrumented section	Monitoring time [days][a]	Deformation[b] [mm]	Measurement point[b]	Vector[b]
S3-FW	6-9	38	15	v_1
S3:4-FW	9-14	8.0	14, 15	v_1
S4-FW	9-14	7.0	11,12	v_1
S6-FW	-	-	15	-

[a] Day when total station measurement started-Day when the shear failure was detected.
[b] With respect to time when shear failure was detected.

The behaviour of the roof was analysed by plotting the deformation versus measurement points in the roof. Two example plots are shown for S3-roof and S7-roof in Figure 32 and Figure 33, respectively. The deformations in the roof were increasing toward the FW side of the stope. This behaviour was observed in the roof for all sections, except for S3:4 and S4. The largest deformations (44 mm, vector v_3) in S3-roof was registered at measurement point 10 (Figure 32a). These findings are summarized in Table 13. The deformations in S6-roof also increased toward the FW. Previous analysis of the HW and FW showed that bending of the HW and shear failure in the FW occurred at S6. It might indicate that, due to the bending in the HW and shear failure in the FW, the roof is moving more in the proximity of the FW at S6. The

observed deformation pattern indicates that the roof is being punched into the FW, as illustrated in Figure 32b. This is in line with the general roof behaviour described by Krauland et al., (2001). Though shear failure was not observed in S6:7-FW and S7-FW the increase of deformation toward the FW was similar and noticeable for both S6:7-roof and S7-roof as shown in Figure 33. The maximum displacements were registered by measurement points 11 and 12. The fact that the largest movement occurred in measurement points close to the FW could indicate that parallel fractures in the roof were activated due to shear failure in the FW.
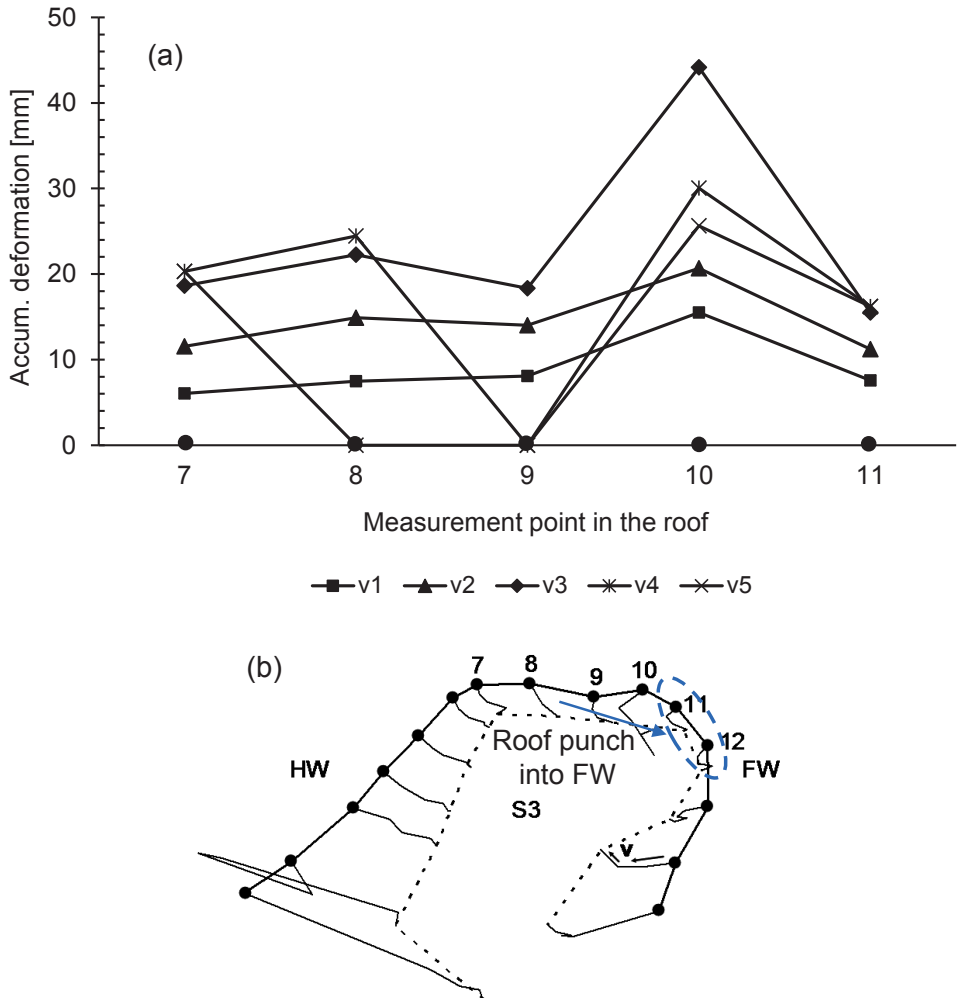
Figure 32 (a) Total station deformations with respect to measurement points in the roof for S3-roof, and (b) roof punching into FW side of the stope.

Table 13 Deformations related to movement and punching of the roof.

Instrumented section	Largest deformation [mm]	Measurement point	Vector
S3-roof	44	10	v_3
S6-roof	13	11	v_5
S6:7-roof	15	12	v_5
S7-roof	23	11	v_5
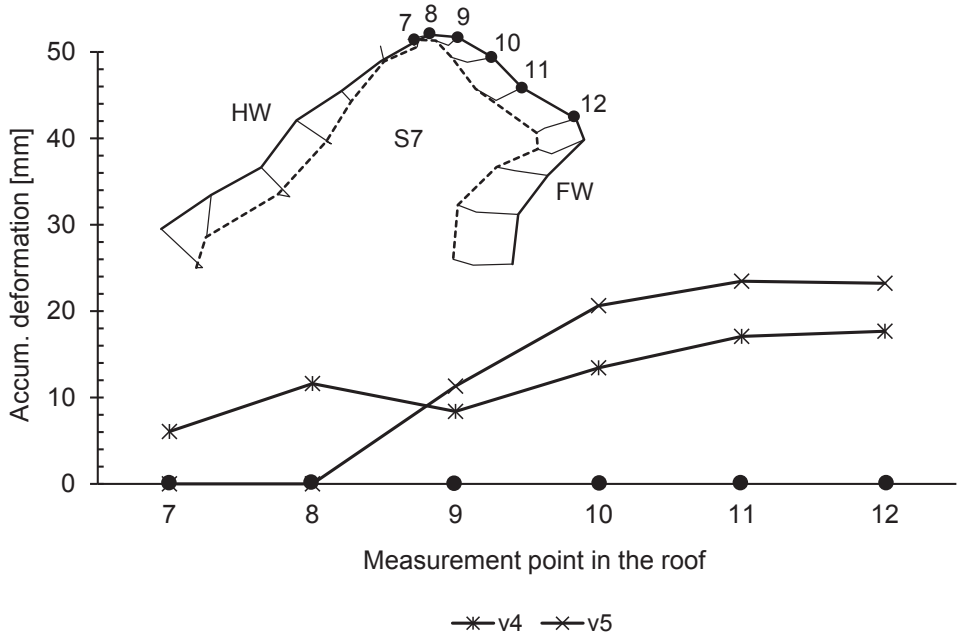
Figure 33 Total station deformations with respect to measurement points in the roof for S7-roof.

6   DEFORMATION DURING WEDGE FAILURE

In this chapter, failures typical of a hard, jointed rock mass are presented. Failure and deformation data from a historical case involving a monitored drift in the Kiirunavaara mine were used to evaluate the failure-deformation behaviour of a rock wedge.

6.1   Field observations

According to Björnfot (1983d) a large rock wedge was observed in the FW side of the test drift between measurement profile R4 and R7. The wedge at measurement profile R5 is shown in Figure 34. An upper and lower joint formed the wedge as illustrated in the same figure. The behaviour of the wedge was not described or studied in detail by Björnfot (1983a,b,c,d). Joint mapping of the FW side of the drift detected three sets of natural joints forming the wedge (Björnfot, 1983a). The orientations of these joints are presented in Table 14.
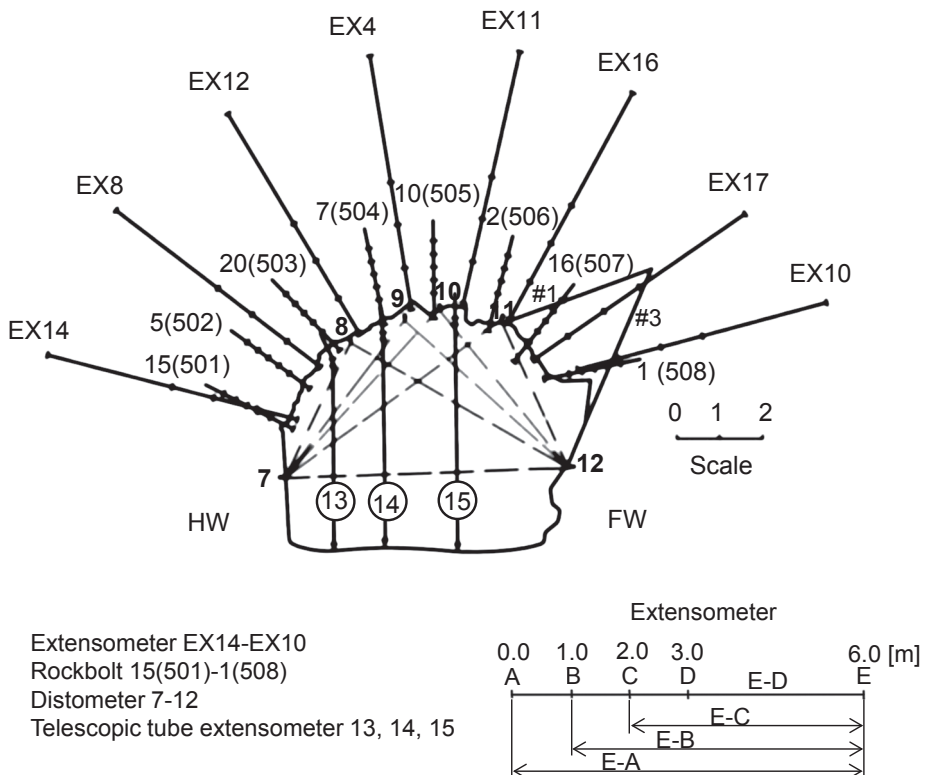
Figure 34 Measurement profile R5 of the test drift showing a wedge in the footwall side of the drift. The upper and lower joints are the #1 and #3, respectively.

Table 14 Orientation (relative to the mine north) and coordinate for the natural joints (Björnfot, 1983a) forming the block.

Natural joints	Strike	Dip
#1-upper joint	160°	30°
#2	150°	85°
#3-lower joint	50°	90°
Drift orientation relative to the mine North: trend = 12°, plunge = 0°		

6.2 Deformation monitoring

A 20 m long section of the test drift was monitored using extensometers, distometers, telescopic tube extensometers, and instrumented rockbolts, cf. Figure 34. The instrumentation was installed in "rows" with a spacing of 1.5 m between rows as shown in Figure 35. The extensometers were installed in 10 rows, termed "measurement profiles" in this work (R1 through R10). Measurement profile R5 was the most instrumented profile along the test drift. The majority of the extensometers were installed before September 1980. Monitoring was conducted over a period of 20 months (Björnfot and Stephansson, 1984). Extensometers were used to record the effect of mining on the rock mass in terms of displacement along the extensometer length. Only extensometers EX16, EX17, EX10 and EX-x intersected the wedge at measurement profiles R5 and R6. EX16 intersected the upper joint and EX17, EX10 and EX-x the lower joint. Each extensometer comprised five anchors (A, B, C, D and E) located at the drift boundary (anchor A) and along the extensometer length at distances of 1 m (anchor B), 2 m (anchor C), 3 m (anchor D), and 6 m (anchor E), cf. Figure 34. A few rockbolts also intersected the wedge, but the effect of these bolts on the wedge stability is not known and was not concluded by Björnfot (1983d).
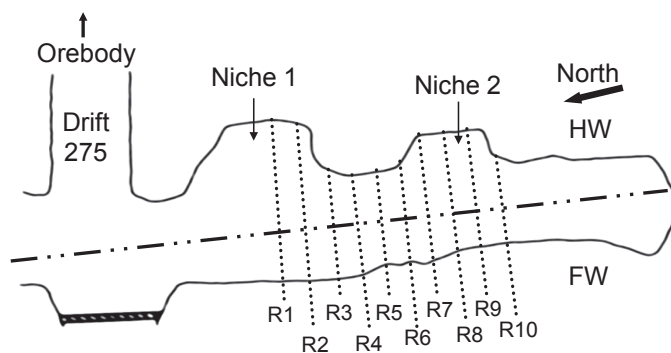

Figure 35 Plan view of instrumentation installation on level 514 m. Modified after Björnfot (1983b).

From displacement versus time plots reported by Björnfot (1983c) the displacement was recorded at five times or mining production stages (ST1-2 to ST5). These five stages corresponded to a summary of the mining activities between levels 478 m and 526 m. Larsson (1983) summarized ST1 and ST2 as one mining stage only, i.e., ST1-2. Björnfot (1983c) showed the displacement between anchors (i.e., A-B, B-C, C-D and D-E). However, in this paper the accumulated displacement relative to the anchor E, located 6 m from the drift boundary, (i.e., E-A, E-B, E-C and E-D) was used as reference.

In the present work, displacements are positive during extension (or elongation) and negative for compression (or shortening) along the extensometer. In extension the wedge thus moves toward the boundary of the drift. The accumulated displacement is presented in Figure 36 for extensometers EX16, EX17 and EX10 located at measurement profile R5. Two things are completely unclear from the drawings and from the interpretations by Björnfot (1983c): (i) whether EX16 intersects the upper joint, and (ii) the exact location of the extensometer head with respect to the upper joint.

All displacements were positive indicating that the wedge moves toward the boundary of the drift. The displacement of the rock mass is a decaying function of the distance, i.e., the largest deformations occurred at the drift boundary, as expected. The largest displacement (around 8 mm) was measured by EX16 (the extensometer with its collar closest to the upper joint) during mining stages ST4 and ST5. It is possible that this extensometer actually intersected the upper joint. There may also be small joints in the rock mass that influence the measured deformations. For EX17, the displacements at the boundary (anchor A) relative to anchor E increased from 1.0 mm (ST1-2) to 3.8 mm (ST5), while the relative displacement E-A along EX10 increased from 0.1 mm (ST1-2) to 5 mm (ST5).
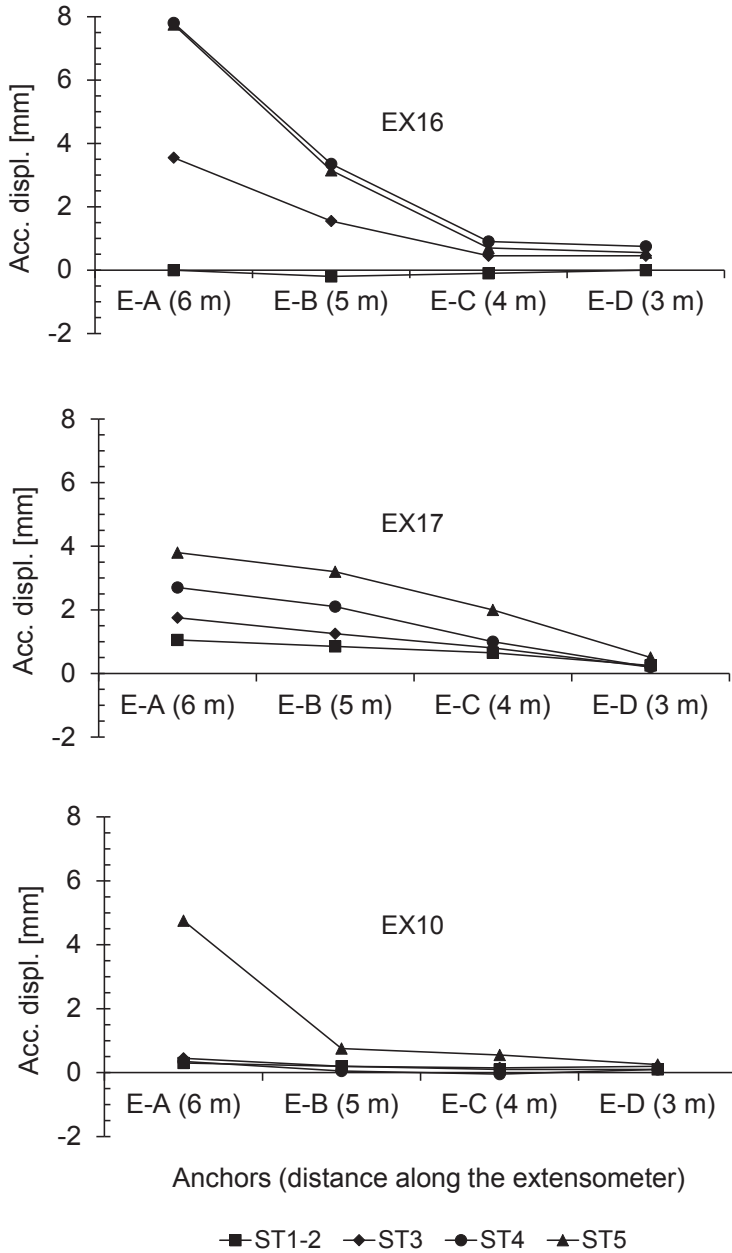
Figure 36 Accumulated displacement with respect to mining stages for EX16, EX17 and EX10.

6.3 Numerical modelling

Numerical modelling was conducted to analyse the behaviour of the rock mass and the wedge.
A global model of the Kiirunavaara mine was used to calculate the stresses induced by the

sublevel caving. The model was analysed using the two-dimensional finite element program *Phase2* (Rocscience Inc., 2009). The stresses in the global model at the position of the studied drift were applied to a local model. Five mining stages were modelled for the 3D model (ST1-ST5), as illustrated in Figure 37. Only one stage was modelled in the 2D model, corresponding to mining from the surface to mining stage ST5. A homogenous, isotropic continuous and linear-elastic rock mass was assumed for this model. The virgin stresses used as input to the global model were given by Sandström (2003). The rock properties presented by Malmgren and Sjöberg (2006) were used as input for the ore and rock mass in the model. Smaller elements were used around the orebody and near the test drift, compared to the rest of the model, see Figure 37.

Figure 37 Global model of the Kiirunavaara mine as modelled using *Phase2*, and with mining stages (ST1-ST5) shown.

6.3.1 2D model

The local model of the discontinuous rock mass surrounding the test drift at the 514 m level was analysed using the Universal Distinct Element Code (*UDEC*), a two-dimensional numerical program based on the distinct element method for discontinuum modelling (Itasca Consulting Group, Inc., 2004). The stresses calculated from the global model at the 514 m level were applied 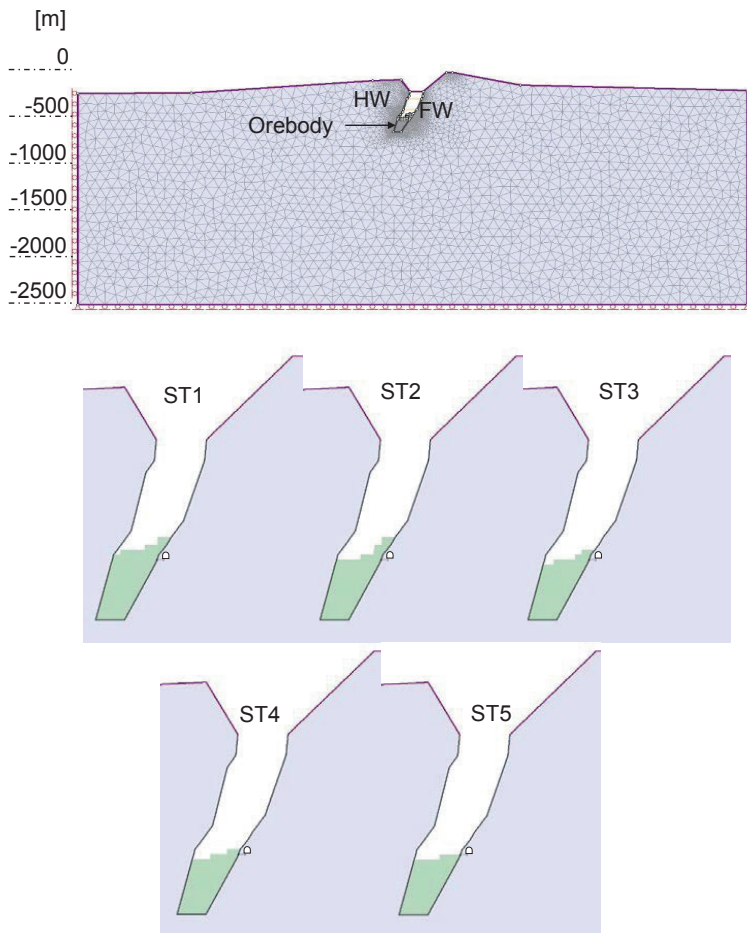to this model. For this model an isotropic linear-elastic rock mass was assumed. The rock properties of the footwall (Malmgren and Sjöberg 2006) were used as input parameters for the rock mass in the model. The joints in the model were analysed using a linear-elastic perfectly plastic material model. For the "construction joints" in the model, fictitious joint properties were estimated according to Kulatilake et al., (1995). Only the upper and lower joints were modelled. Properties for the natural (pre-existing) joints in the model were taken from Malmgren and Nordlund (2006). The zone length adjacent to the test drift was smaller compared to that in the rest of the model. The model is shown in Figure 38a.
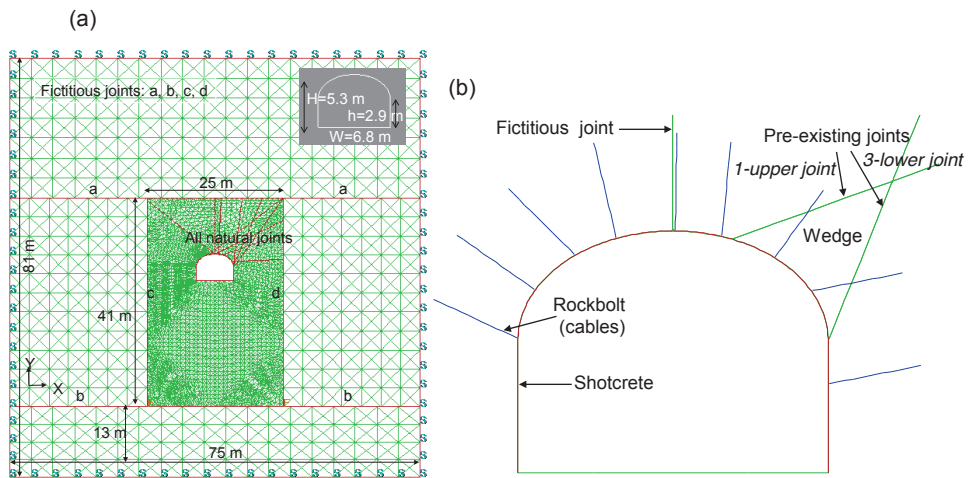
Figure 38 (a) local 2D model of the test drift located at the 514 m level using a linear-elastic perfectly plastic material model in *UDEC*, and (b) Pattern for reinforcement of the test drift at measurement profile R5 used in the local model. The geological structures forming the large wedge are shown. S = stress boundaries, F = fixed velocities.

In the local 2D model shotcrete and rockbolts were modelled since the area surrounding the test drift was reinforced with rockbolts, cable bolts and shotcrete as stated in Björnfot and Stephansson (1984), see Figure 38b. In the test drift all bolts were grouted with cement. The shotcrete was modelled with a linear-elastic perfectly plastic material model. Properties for the reinforcement are according to Malmgren (2008). The rockbolts in the model were installed at the same location as in the field, cf. Figure 34. A joint friction angle (*jϕ*) of 35° was used in this model for the natural joints.

In this model slip (meaning that the shear strength of the joint is reached) occurred along the lower joint as shown in Figure 39a, but the displacement along this joint is small (Figure 39b), and the slip area is isolated and does not reach the boundary of the opening. The displacements are parallel to the upper joint, and shear has taken place along this joint (Figure 39c). There is separation of the lower joint near the opening of the drift as shown in Figure 39d. These findings indicate that (i) shear deformations developed along the upper joint and the wedge is rotating, (ii) the movement of the wedge is characterized by mainly elastic deformations, and (iii) the wedge is stable.
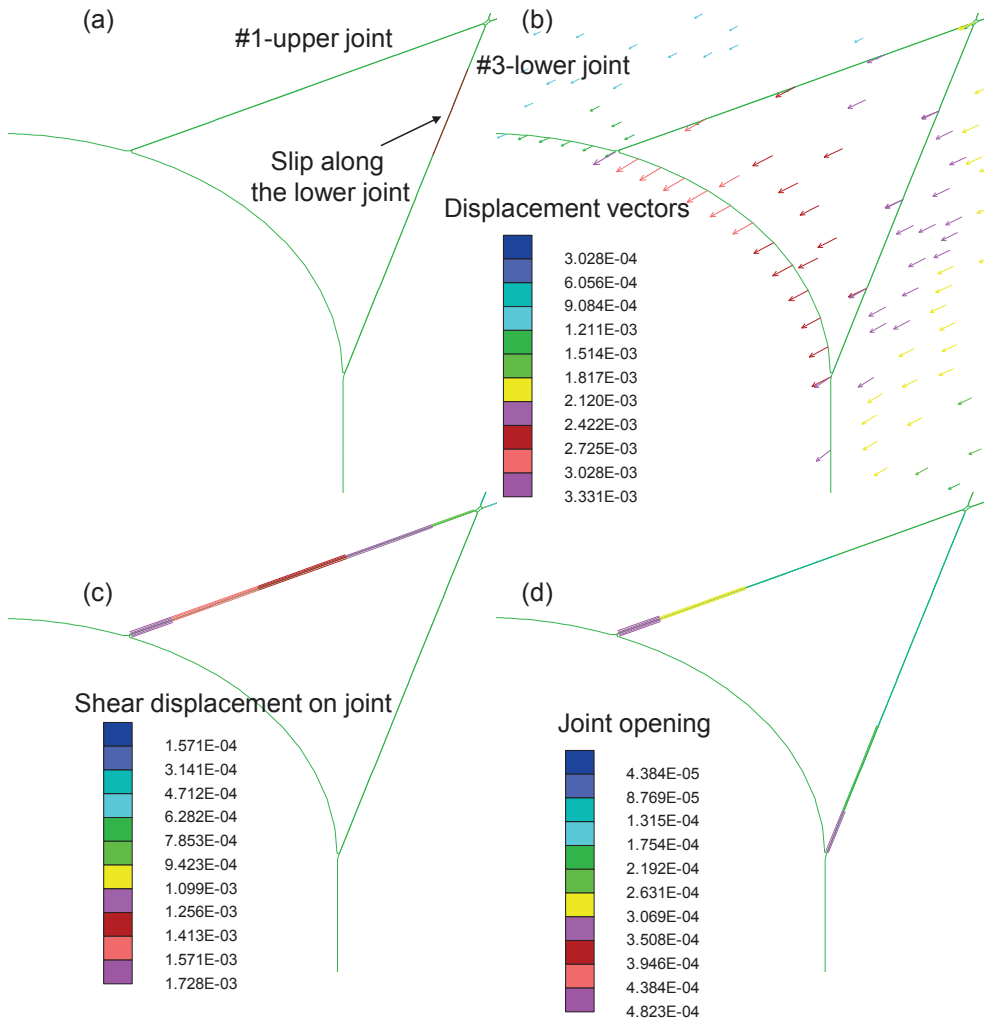
Figure 39 Stability indicator of the joint in the local 2D model using a $j\phi = 35°$.

Some additional results are shown in Figure 40 (major and minor principal stresses and calculated displacements) for the 2D model, but without installed rockbolts. Two cases were modelled – one with the pre-existing joints (discontinuum), and one in which the rock mass was modelled as a continuum (no joints). As evident, there are no major differences between the two models, and the stress state around the drift is, in general, similar in the two models. However, for the continuum case, the displacements are more evenly distributed than in the discontinuum model, i.e., also in the rock surrounding the wedge. These findings indicate that the position of the wedge in the studied case made it behave in another way than if it had been located elsewhere, which is due to the inclination of the stress field caused by the stress re-distribution caused by mining.
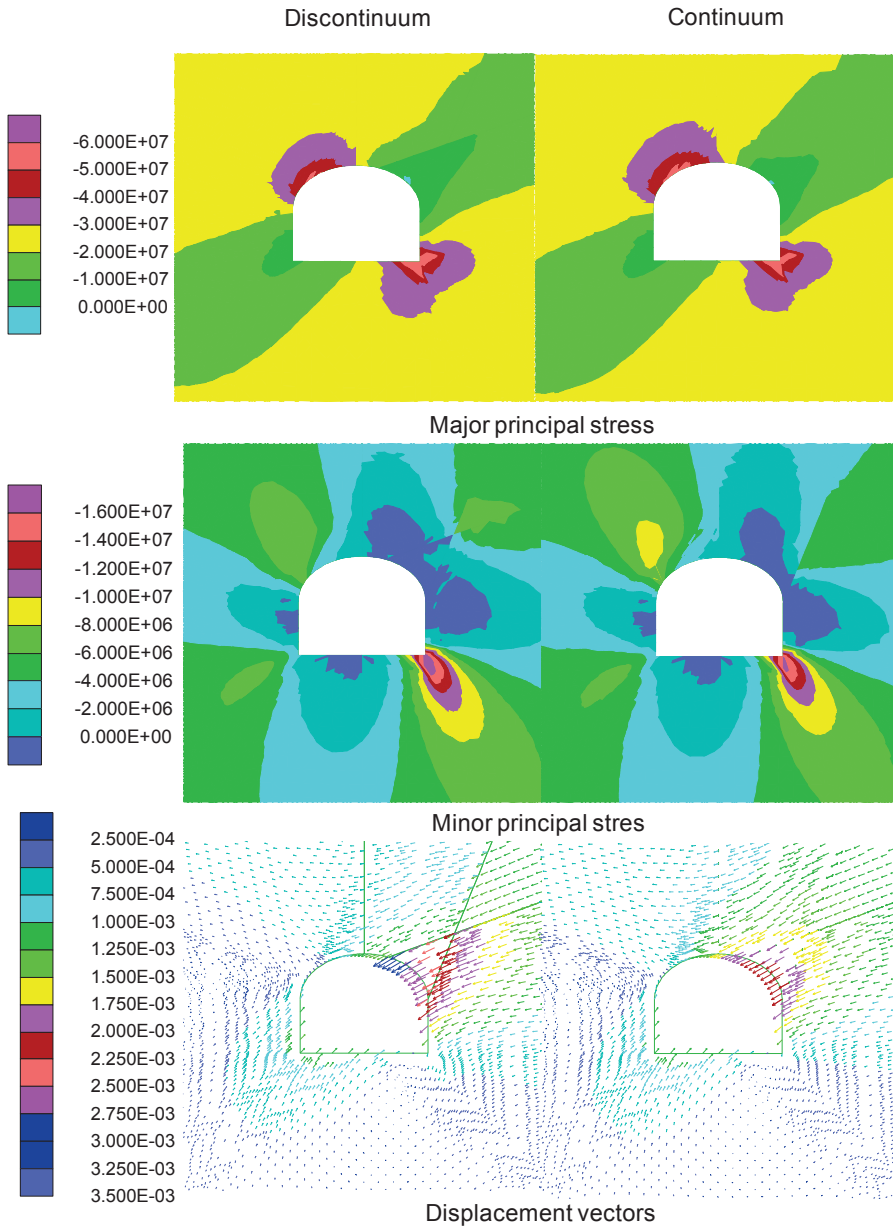
Figure 40 Major and minor principal stress, and displacement vectors in the local 2D model.

6.3.2 3D model

A 3D analysis of the wedge and drift was also conducted. A local model of the discontinuous rock mass surrounding the test drift at the 514 m level was set up using the Three Dimensional Distinct Element Code (*3DEC*). *3DEC* is a numerical code based on the distinct element

method for discontinuum modelling (Itasca Consulting Group, Inc., 2007). The local model was analysed using a linear-elastic material model for the blocks. The model is shown in Figure 41. Three regions (i.e., fine A, medium B, and coarse C length zone) were created. The rock properties of the footwall (Malmgren and Sjöberg 2006) were used as input parameters for the rock mass in this model.

Zone	Region length		
	X [m]	Y [m]	Z [m]
(A)	25.0	35.0	18.3
(B)	38.0	45.0	31.3
(C)	75.0	75.0	48.3
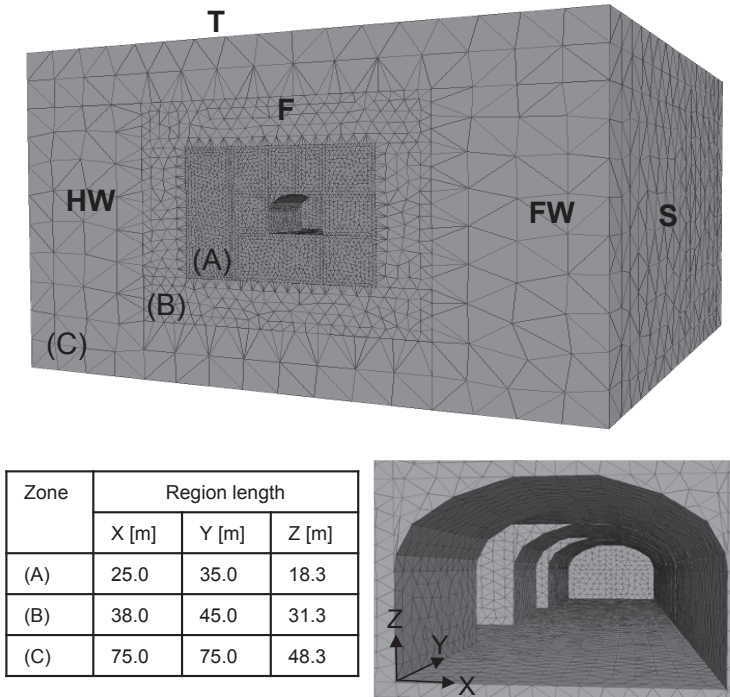
Figure 41 Local 3D model of the test drift located at the 514 m level using a linear-elastic material model for the block, and a Coulomb slip model for the natural joints simulated in *3DEC*.

The three joints forming the wedge were modelled in the local 3D model. Since it was not possible to determine the natural joint characteristics from the documentation an assumption was made that all joints were continuous and persistent beyond the joint traces found from mapping. The joints in the model were modelled using a Coulomb slip model with equal peak and residual shear strengths. For the "construction joints" in the model, fictitious joint properties were estimated according to Kulatilake et al., (1995). Properties for the natural joints in the model were taken from Malmgren and Nordlund (2006) and Malmgren (2008). The values for the joint friction angle of the natural joints were varied and three cases were modelled, i.e., $j\phi$ = 15, 31 and 38°.

Slip occurred for all three modelled cases. The largest area of slip occurred for case 3 (with the lowest joint friction angle $j\phi = 15°$), which was as expected. Slip did not occur along the lower joint in case 1 and 2, and in case 3 this joint showed the smallest slip area (Figure 42) among the three joints.

Accumulated displacements were further calculated for case 3 at the same position as the installed field extensometers in measurement profile R5. For EX17 and EX10 the calculated displacements with respect to all mining stages are shown in Figure 43. However, since the exact position of the upper joint, in relation to EX16, is not known, the deformations measured by EX16 were not used in the comparison of monitored and numerical modelling results. The displacements were positive, thus indicating that the wedge moved toward the drift boundary. The deformations are plastic (non-elastic), but very small and the wedge is stable (no fallout).

#1-upper joint
#3-lower joint

Slipping now
Slipped (past)
Tensile failure
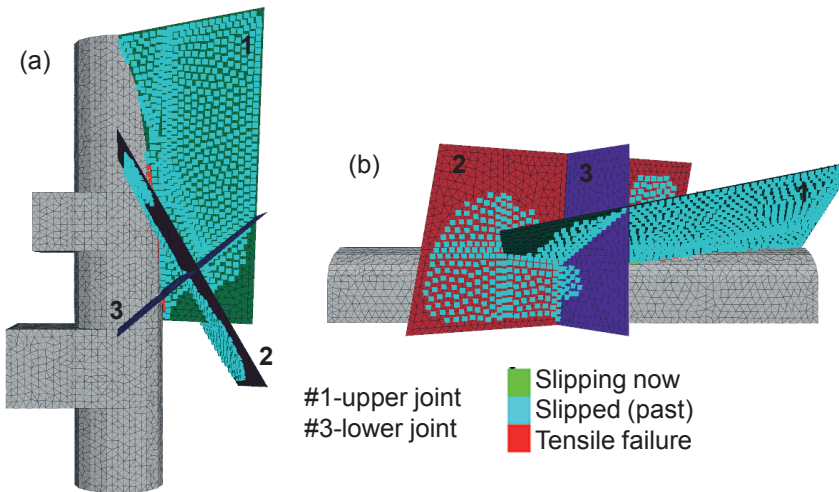
Figure 42 Slip joint indicator in the local 3D model using $j\phi = 15°$. (a) Horizontal view, and (b) vertical view from FW side.
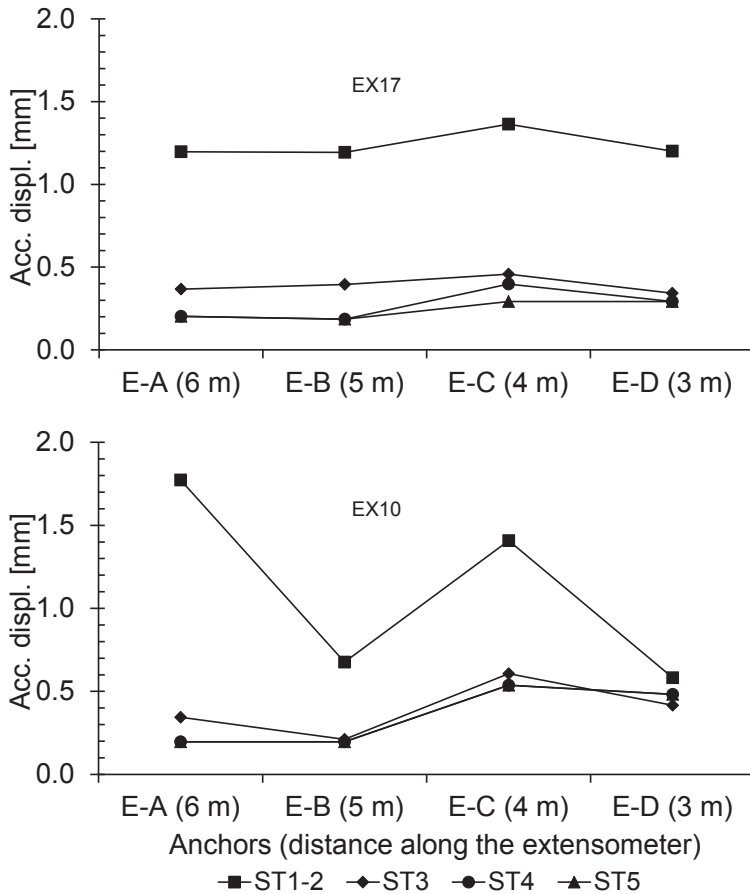
Figure 43 Displacement calculated in the local 3D model for EX17 and EX10 using $j\phi$ = 15°.

6.3.3 Field and model comparison

In Sections 6.2, 6.3.1 and 6.3.2 deformation data from measurement in the field and local 2D and 3D model were presented. Table 15 shows a comparison for the field (Figure 36) and local 2D (Figure 39) and 3D models (Figure 42 and Figure 43). Joint #2 does not exist at measurement profile R5.

The field data showed that the wedge was sliding along both the upper and lower joints. The upper joint showed the largest displacement among the three joints. The local 2D model showed that shear deformation takes place along the upper joint and the wedge is stable. In the local 3D model, slip of the three joints was indicated. The area of slip was small for the lower joint. The deformation data from the 3D model also showed that the wedge was sliding along the lower joint and toward the boundary of the opening. These findings indicate that both the upper and lower joint experience slip. It is also likely that the wedge slip along joint #2 as

shown by the slip indicator plot in Figure 42. The displacements associated with the wedge in the two local models were non-elastic, but not large enough to cause the wedge to fall out; hence the wedge is interpreted as being stable.

Table 15 Field and local 3D model comparison.

Joint	Field	Local 2D model ($j\phi$ = 35°)	Local 3D model ($j\phi$ = 15°)	
	Extensometer	Shear deformation and slip indicator	Slip indicator	Extensometer
	Figure 36	Figure 39	Figure 42	Figure 43
#1-upper joint	Slide++	Shear deformation++	Slip++	NA[b]
#2	NA[a]	-	Slip++	NA[a]
#3-lower joint	Slide+	Slip+	Slip+	Slip

[a] Joint #2 does not exist at measurement profile R5.
[b] Deformations were not recorded along EX16 in the local model.
The plus symbol indicate the magnitude of the shear displacements and the slip area.

The field measurement plots showed that the displacements were a decaying function of the distance, cf. Figure 36. This was not observed in the 3D model (see Figure 43) and the pattern presented in this figure was difficult to interpret. There are at least two explanations to the difference between the monitored deformations and those obtained from numerical analyses: (i) the exact shape of the wedge was not known and it was assumed that all joints were continuous and persistent beyond the joint traces found from mapping, which could not be verified from the documentation, and (ii) the joint stiffnesses were also assumed, as no information was available about the real values. This is a common problem for most numerical analyses and not unique for the model in this thesis. The small displacements found from the numerical model further showed that the rockbolts may not have been required for keeping the stability of the wedge.

7   DISCUSSION

The thesis work has comprised analyses of measured data from laboratory tests and monitoring results from field cases as well as numerical analyses. Large efforts were spent on trying to find cases exhibiting one or several failure mechanisms and in which deformation monitoring of the failure process had been carried out. A limited number of cases with good information about the failure behaviour some of them with good monitoring data and some with no measurements but with good failure observations were used in the doctoral work. Moreover the cases studied in detail in this thesis were all from Swedish mines. The obtained information was, nevertheless, valuable for the improvement of the understanding of the deformation during the development of failure in laboratory and field scale.

The study of the failure-deformation process of fifteen tested rock types showed that the mean values of the normalized strain quantities and the volumetric strains at crack initiation and crack damage stages varied among the studied rock types. The scatter was different for the different strain quantities. E.g., 2/3 of the means of $\varepsilon_{Icd}/\varepsilon_{1p}$ were within the interval 70-90% and the means for all rock types were within the interval 60-100%. The scatter for $\varepsilon_{Ici}/\varepsilon_{1p}$ as similar, but for the other quantities it was considerably greater.

The correlation of the rock characteristics of the studied rock types and the means of the studied strain quantities revealed that $\varepsilon_{3cd}/\varepsilon_{3p}$ was strongly influenced by the grain size. Eberhardt et al., (1999) showed similar results, i.e., that the onset of crack coalescence and crack damage depended on the grain size of the rock. From the modelled spalling failures of the Garpenberg raise and Zinkgruvan exploration drift cases it was observed that (i) the volumetric and maximum shear strains indicated the position of localized macroscopic failure surfaces, in this thesis called strain concentration bands, and (ii) the distances from the boundary to the strain concentration bands which are closest to the boundary in the plastic analyses (linear-elastic brittle (LE-B), and linear-elastic perfectly plastic (LE-PP)) were similar to the depth of the observed fallouts in both modelled cases. These findings indicate that both material models and the used rock properties satisfactorily predicted the depth of failure. However, the linear-elastic and the LE-PP material models could not simulate the notch failure shape typical of spalling failure in the Zinkgruvan exploration drift model case.

The comparison of the strain quantities from laboratory tests with the corresponding values from the numerical analysis helped to identify the stages of the failure-deformation process and the location of potential failure surfaces in the two modelled cases. It would not have been possible to identify the different failure stages of these cases without the information provided by the laboratory test results.

The use of laboratory data as input for prediction of failure around underground excavations may be questionable, due to the possible scale effect between the intact rock and the rock mass as well as differences in kinematics. However, it seems to be possible to use laboratory strength and strain data to predict spalling failure, since spalling occurs through intact rock, whereas the use of laboratory data is less likely to work satisfactorily for prediction in cases of large volumes of a fractured rock mass. According to Diederichs (1999) in certain situations both the sample size and the flaw size are important and related, but in others the flaw size is limited by the grain size. Larger specimens contain a greater quantity of weak flaws with respect to smaller specimens, i.e., the number of microcracks depends on the size of the rock specimen.

Furthermore, the larger samples can also contain flaws of greater size than smaller samples. It is therefore an increased number of potentially critical cracks in large specimens due to the greater number of and possible size of microcracks. However, as reported by Diederichs (1999), the crack initiation beyond the grain scale is not dependent on the specimen size. Therefore, the method used in this doctoral work to evaluate the failure process around an underground excavation by using strains calculated from laboratory tests should be carefully implemented for evaluation of failure process of the rock mass.

Furthermore, the strain comparison showed that the minor principal strain (ε_3) in the linear-elastic model was less than the lateral critical strain at crack initiation ($\varepsilon_{3ci}/\varepsilon_{3p}$) at a distance from the boundary of the opening, which is similar to the observed depth of the fallouts in the field. This finding seems to be in line with Diederichs (1999) who states that the *in situ* yield limit is related to the damage initiation thresholds obtained from laboratory experiments or from microseismic monitoring in the field. However, the relation between the yield limit *in situ* and the deformation stage representing fallout is yet to be determined.

A number of factors which probably explain the difference in behaviour of the rock in the numerical model and in the real case are as follows:

(i)   The observed fallout may be the result of a progressive failure process consisting of multiple fallouts. Since the observation is done by mapping at a certain time no one knows exactly how the failure and fallout developed before the first failure observation. The numerical method used in the present study cannot mimic the real behaviour including multiple fallouts.

(ii)   The constitutive models available are not specifically designed for spalling failure. The Mohr-Coulomb failure criterion is a linear shear failure criterion. However, according to Diederichs (1999) "If appropriately applied, with unconventional selection of key parameters (e.g., very low *m* or slope parameter), the Hoek-Brown criterion can be used effectively to predict *in situ* damage (Martin et al., 1996, 1997; Pelli et al., 1991). Criteria such as Mohr-Coulomb (Coulomb, 1773; Jaeger and Cook, 1971; Paul, 1961) and Modified Griffith (McClintock and Walsh, 1963) are similar in form and all assume varying degrees of dominance and continuity of transition between tensile rupture and shear failure." With an unconventional selection of Mohr-Coulomb parameters the criterion can probably mimic the spalling behaviour with an accuracy which is acceptable from an engineering point of view.

(iii)   The strain values used as "critical" values to identify potential fallouts were not obtained from tests of the host rock of the analysed openings. Values from tests of rock types with similar characteristics were used instead. Since the scatter in properties and/or behaviour might be significant, this may have affected the comparison of calculated (using *Phase2*) and measured critical strains.

In the studies of shear and bending failure, the monitoring of the stope in the Kristineberg mine provided data, which have contributed to the understanding of such failures. There was clear evidence that bending took place in the HW. However tensile failure caused by bending (e.g., fractures) was not observed on the HW surface. Hence, it was assumed in this doctoral work that bending was indicated in the HW after evaluation of the deformation pattern by means of total station measurement. Moreover, the observed shear deformation in BH1-HW

shown in Figure 27a could indicate that a layer of the HW is detached from the host rock mass. This layer is later the part of the HW that deforms in a bending manner, hence suggesting that bending took place in the HW of the stope. The onset of tensile failure due to bending could not, however, be determined from the field data.

It was difficult to judge whether or not bending and shear failure occurred inside all the surveyed boreholes due to lack of visibility and obstructions along the boreholes. However, shear failure was observed in three (out of nineteen) boreholes. The information from the borehole surveys was very important for the interpretation of the stope behaviour. Since the borehole surveys and the deformation readings were not done daily, the onset of shear failure could not be detected.

The monitored stope in the Kristineberg mine was also studied using numerical analyses (Saiang and Nordlund, 2013). The results from these analyses confirmed the observed behaviour described in this doctoral work.

Finally, regarding the studied wedge failure, the use of deformation data from the extensometer in the field again proved to be valuable for the understanding of the behaviour and stability of the wedge. However, the lack of information could in certain situations affect the interpretation of the results as was the case for one of the extensometers installed in the field. The exact location of the extensometer in the wedge related to the upper joint was not well known, hence the behaviour of the wedge with respect to the upper joint was presumed. The wedge and the drift are three dimensional. However, the results from the local 2D and 3D models showed similar conceptual behaviour. These results also showed qualitatively good agreement with the field observations.

8   CONCLUSIONS

Based on the conducted work the following conclusions can be drawn:

–   The failure-deformation process of the intact rock can be linked to the geological characteristics of the intact rock such as grain size and mineral composition.

–   The volumetric strain and maximum shear strain as well as the major and minor principal strains can be used to describe the behaviour of the spalling, i.e., identify the crack initiation, crack damage and peak strength, and location of potential failure surfaces in the boundary of an opening and in the rock mass. Thus, the location of a future spalling failure may be estimated based on numerical analysis.

–   The linear-elastic brittle material model using CSFH (Cohesion Softening Friction Hardening) simulated the spalling around the boundary of the Garpenberg raise as the observed failure in the field, and consequently enabled the estimation of localized failure surfaces. The linear-elastic perfectly plastic material model of the Zinkgruvan case enabled the estimation of localized failure surfaces.

–   Bending and shear are examples of failure mechanisms that display a progressive behaviour, which make them suitable for deformation monitoring.

–   The failure process (onset and development) could be determined in some detail through analysis of the deformation pattern of the excavation.

This work has also helped to improve the understanding of the failure process and associated deformations, as follows:

–   The failure process of each failure mechanism develops differently.

–   The failure process due to spalling can occur very fast and the response of the rock mass is limited before fallout occurs, i.e., spalling failure cannot be detected until it is observed on the surface of the opening. Numerical modelling, however, can be used to simulate the progressive failure and fallout of spalling.

–   Bending and shear failure progress in a slow manner and the deformation pattern can be monitored before any failure is observed on the boundary of an opening. Deformation monitoring can therefore simultaneously give information as the failure progresses.

–   The movement of wedges can be monitored as long as they are stable beyond the excavation process. However, in many cases the wedges became unstable already during blasting and scaling and have been removed at the time when any instrumentation can be installed.

–   For spalling failure onset of cracking and propagation was identified using the intact rock information. For the other failure mechanisms the failure process could not be determined as was done for spalling. Deformation values were estimated for all failure mechanisms. Furthermore, if strains are used to predict failure and fallout, failure criteria

and complete constitutive models based on strain have to be developed and other input parameters have to be collected.

9 SUGGESTIONS FOR FUTURE RESEARCH

Further studies would improve the understanding of deformation and failure of hard rock:

– The effect of rock characteristics (grain size and mineral composition) on the failure process of the rock needs further investigation. The investigation should focus on investigating why the lateral strain at the crack damage stage of the failure process is highly influenced by these rock characteristics.

– Numerical analysis of the spalling failure around the Zinkgruvan exploration drift should be carried out with other constitutive models, e.g., a strain softening model, which can better capture brittle failure.

– More underground cases with failure and deformation measurement should be studied by combining field monitoring data and numerical analyses. This work can also be extended by studying other failure mechanisms encountered in other rock conditions, e.g., squeezing, rockburst, swelling, etc.

– A failure criterion based on the deformation quantities should be developed. Such a failure criterion could be used to predict failure and fallout, and the progressive behaviour of failure. A different failure criterion is likely required for each failure mechanisms, since the deformational behaviour is very different for different types of failure, as showed in this thesis work.

REFERENCES

Alejano, L.R., Rodríguez-Dono, A. and Veiga, M. (2012). **Plastic radii and longitudinal deformation profiles of tunnels excavated in strain-softening rock masses**. Tunnelling and Underground Space Technology, **30**: 169–182.

Alonso, E., Alejano, L.R., Varas, F., Fdez-Manín, G. and Carranza-Torres, C. (2003). **Ground response curves for rock masses exhibiting strain-softening behaviour**. International Journal for Numerical and Analytical Methods in Geomechanics, **27**(13): 1153-1185.

Anderson, J. (2000). **Underground movement**. Tunnels and Tunnelling International, 33(8): 20-22.

Andersson, J.C. (2007). **Rock mass response to coupled mechanical thermal loading: Äspo pillar stability experiment, Sweden**. Doctoral thesis, Royal Institute of Technology, 179 p.

Andreev, G.E. (1995). **Brittle failure of rock materials: test results and constitutive models**. A.A. Balkema, Rotterdam, 446 p.

Aydan, Ö., Akagi, T. and Kawamoto, T. (1993). **The Squeezing potential of rocks around tunnels – theory and prediction.** Rock Mechanics and Rock Engineering, **26**(2): 137-163.

Bagheri, M. (2011). **Block stability analysis using deterministic and probalistic methods**. Doctoral thesis, Royal Institute of Technology, 73 p.

Bagheri, M. and Stille, H. (2011). **Investigation of model uncertainty for block stability analysis**. International Journal for Numerical and Analytical Methods in Geomechanics, **35**(7): 824-836.

Bagheri, M. and Stille, H. (2013). **A new analytical solution based on joint relaxation for analysing symmetrical block stability**. International Journal for Numerical and analytical Methods in Geomechanics, **37**(8): 771-786.

Bieniawski, Z.T. (1967). **Mechanism of brittle rock fracture. Part I. Theory of the fracture proces**s. International Journal of Rock Mechanics and Mining Sciences and Geomechanical Abstracts, **4**(4): 395-406.

Björnfot, F. (1983a). **Bultförstärkning av blockig bergmassa i ett föränderligt spänningsfält. Resultat från försöksort i Kiirunavaaragruvan. Delrapport 2: Bakgrund, forskningsprogram och försöksplats**. Högskolan i Luleå, 1983:42T. (*in Swedish*).

Björnfot, F. (1983b). **Bultförstärkning av blockig bergmassa i ett föränderligt spänningsfält. Resultat från försöksort i Kiirunavaaragruvan. Delrapport 3: Instrumentering och mätprogram**. Högskolan i Luleå, 1983:43T. (*in Swedish*).

Björnfot, F. (1983c). **Bultförstärkning av blockig bergmassa i ett föränderligt spänningsfält. Resultat från försöksort i Kiirunavaaragruvan. Delrapport 4: Resultat från fältmätningar**. Högskolan i Luleå, 1983:44T. (*in Swedish*).

Björnfot, F. (1983d). **Bultförstärkning av blockig bergmassa i ett föränderligt spänningsfält. Resultat från försöksort i Kiirunavaaragruvan. Delrapport 6: Analys och utvärdering**. Högskolan i Luleå, 1983:46T. (*in Swedish*).

Björnfot, F. and Stephansson, O. (1984). **Mechanics of grouted rock bolts-field testing in hard rock mining**. BeFo 53:1/84 report, 77 p.

Board, M., Krauland, N., Sandström, S. and Rosengren, L. (1992). **Analysis of ground support methods at the Kristineberg Mine in Sweden**. In: *Kaiser, P.K. and McCreath, D.R. (Eds.): Rock Support in Mining and Underground Construction, Balkema, Rotterdam, pp.499-506.*

Brady, B.H.G. and Brown, E.T. (1993). **Rock mechanics for underground mining**. Chapman and Hall, 2nd edition, London, 571 p.

Brady, B.H.G. and Brown, E.T. (2004). **Rock mechanics for underground mining**. Springer, 3rd edition, The Netherlands, 628 p.

Brown, E.T. (1981). **Rock characterization testing and monitoring**. ISRM Suggested Methods, Pergamon Press, Oxford, 211 p.

Brown, E., Bray, J., Landayi, B. and Hoek, E. (1983). **Ground response curves for rock tunnels**. Journal of Geotechnical Engineering, **109**(1): 15-39.

Cai, M., Kaiser, P.K. and Martin C.D. (2001). **Quantification of rock mass damage in underground excavations from microseismic event monitoring**. International Journal of Rock Mechanics and Mining Sciences and Geomechanical Abstracts, **38**(8): 1135-1145.

Carlsson, B. (2010). Personal communication.

Carlsson, B. and Nordlund, E. (2013a). **The failure process of brittle rock under different loading conditions**. Work in progress.

Carlsson, B. and Nordlund, E. (2013b). **Influence of micro cracks and fabric on the failure process of rock**. Work in progress.

Carlsson, B., Nordlund, E., Andersson, Y. and Lindfors, U. (1999). **The failure process and the acoustic emission of brittle rock under compression**. In: *Vouille, G. (Ed.): 9th International conference on rock mechanics, Balkema, Taylor and Francis The Netherlands, Paris, August 1999, pp. 569-572.*

Carranza-Torres, C. and Fairhurst, C. (2000). **Application of the convergence-confinement method of tunnel design to rock masses that satisfy the Hoek-Brown failure criterion**. Tunnelling and Underground Space Technology, **15**(2): 187-213.

Chang, Y. (2006). **Rock strain-strength criterion and its application**. In: *Leung, C.F. and Zhou, Y.X. (Eds.): 4th Asian Rock Mechanics Symposium, ISRM International Symposium on Rock*

Mechanics in Underground Constructions, World Scientific Publishing Co. Pte. Ltd., Singapore, November 8-11 2006, ISBN 981-270-437-X.

Chang, Y. (2011). **Applications of strain based damage criterion in geotechnical engineering**. In: *Qian, Q. and Zhou, Y. (Eds.): 12th ISRM International Congress on Rock Mechanics. Harmonising Rock Engineering and the Environment, Taylor & Francis Group, Beijing, China, October 16-21 2012, ISBN 978-0-415-80444-8.*

Diederichs, M. (1999). **Instability of hard rock masses: the role of tensile damage and relaxation**. Doctoral thesis, University of Waterloo, 567 p.

Eberhardt, E., Stead, D. and Stimpson, B. (1999). **Quantifying progressive pre-peak brittle fracture damage in rock during uniaxial compression**. International Journal of Rock Mechanics and Mining Sciences and Geomechanical Abstracts, **36**(3): 361-380.

Eberhardt, E., Stead, D., Stimpson, B. and Read, R.S. (1998). **Identifying crack initiation and propagation thresholds in brittle rock**. Canadian Geotechnical Journal, **35**(2): 222-233.

Edelbro, C. (2003). **Rock mass strength: a review**. Technical report 2003:16, Luleå University of Technology, 92 p.

Edelbro, C. (2008). **Strength, fallouts and numerical modelling of hard rock masses**. Doctoral thesis 2008:56, Luleå University of Technology, 80 p.

Eloranta, P. and Hakala, M. (1998). **Laboratory testing of Kivetty porphyritic granodiorite in borehole KI-KR10**. Working Report Posiva 98-49.

Eloranta, P. and Hakala, M. (1999a). **Laboratory testing of Hästholmen pyterlite in borehole HH-KR6**. Working Report Posiva 98-26.

Eloranta, P. and Hakala, M. (1999a). **Laboratory testing of Hästholmen equigranular rapakivi granite in borehole HH-KR6**. Working Report Posiva 98-47.

Elsworth, D. (1986). **Technical Note Wedge Stability in the Roof of a Circular Tunnel: Plane Strain Condition**. International Journal of Rock Mechanics and Mining Sciences and Geomechanical Abstracts, **23**(2): 177-181.

Hakala, M. and Heikkilä, E. (1997a). **Laboratory testing of Olkiluoto mica gneiss in borehole OL-KR10**. Work report POSIVA-97-07e.

Hakala, M. and Heikkilä, E. (1997b). **Summary report – Development of laboratory tests and the stress-strain behaviour of Olkiluoto mica gneiss**. POSIVA-97-04.

Hatzor, Y.H. and Benary R. (1998). **The stability of a laminated vousooir beam: back analysis of a historic roof collapse using DDA**. International Journal of Rock Mechanics and Mining Sciences, **35**(2): 165-181.

Health and Safety Executive (HSE). (2000). **The collapse of a NATM tunnels at Heathrow airport – a report of the investigation by the Health and Safety Executive**. HSE books, Sudbury Suffolk, 108 p.

Heikkilä, E. and Hakala, M. (1998a). **Laboratory testing of Kivetty granite in borehole KI-KR10**. Work report POSIVA-98-21e.

Heikkilä, E. and Hakala, M. (1998b). **Laboratory testing of Romuvaara tonalite gneiss in borehole RO-KR10**. Work report POSIVA-98-06e.

Hibbeler, R.C. (2005). **Mechanics of materials**. Persson Prentice Hall, Sixth edition in SI units, Singapore, 870 p.

Hoek, E. and Brown, E.T. (1980). **Underground Excavations in Rock**. Institution of Mining and Metallurgy, London, 527 p.

Hoek, E., Kaiser, P.K. and Bawden, W.F. (1995). **Support of Underground Excavations in Hard Rock**. A.A. Balkema, Rotterdam, 215 p.

Itasca Consulting Group, Inc. (2004). *UDEC Version 4.00.134 DP-Universal Distinct Element Code*. www.itascacg.com, Minneapolis, Minnesota, USA.

Itasca Consulting Group, Inc. (2007). *3DEC Version 4.10-3 Dimensional Distinct Element Code*. www.itascacg.com, Minneapolis, Minnesota, USA.

Jiang, Q., Liu, X., Wei, W. and Zhou, C. (2013). **A new method for analysing the stability of rock wedges**. International Journal of Rock Mechanics and Mining Sciences, **60**: 413-422.

Krauland, N., Marklund, P.I. and Board, M. (2001). **Rock support in cut-and-fill mining at the Kristineberg mine.** In: *Hustrulid, W.A. and Bullock, R.L. (Eds.): Underground Mining Method-Engineering Fundamentals and International Case Studies. Society for Mining, Metallurgy, and Exploration, Inc., Littleton, Colorado, USA, pp.325-324.*

Kulatilake, P.H.S.W., Wang, S., Ucpirti, H. and Stephansson, O. (1995). **Effects of joints on the strength and deformability of rock masses**. In: *Proceedings of the Conference on Fractured and Jointed Rock Masses, Balkema, Rotterdam, Lake Tahoe, California, June 3–5 1991, pp. 81-287.*

Lance, G. (2008). Personal communication.

Larsson, H. (1983). **Bultförstärkning av blockig bergmassa i ett föränderligt spänningsfält. Resultat från försöksort i Kiirunavaaragruvan. Delrapport 5: FEM-analys av försöksområdets spänningar och deformationer**. Högskolan i Luleå, 1983:45T.

Malmgren, L. (2005). **Interaction between shotcrete and rock – experimental and numerical analysis**. Doctoral thesis 2005:48, Luleå University of Technology, 24 p.

Malmgren, L. (2008). **Interaction of shotcrete with rock and rock bolts – a numerical study**. International Journal of Rock Mechanics and Mining Sciences, **45**(4): 538-553.

Malmgren, L. and Nordlund, E. (2006). **Behaviour of shotcrete supported rock wedges subjected to blast-induced vibrations**. International Journal of Rock Mechanics and Mining Sciences, **43**(4): 593-615.

Malmgren, L. and Sjöberg, J. (2006). Bergmekaniska analyser för ny huvudnivå i KUJ (avv 1365). LKAB Utredning 06-797, 2006-12-12, 131 p (*in Swedish*).

Martin, C.D. (1997). **Seventeenth Canadian geotechnical colloquium: the effect of cohesion loss and stress path on brittle rock strength**. Canadian Geotechnical Journal, **34**(5): 698-725.

Martin, C.D. and Chandler, N.A. (1994). **The progressive fracture of Lac du Bonnet granite**. International Journal of Rock Mechanics and Mining Sciences and Geomechanical Abstracts, **31**(6): 643-659.

Martin, C.D., Christiansson, R. and Söderhäll, J. (2001). **Rock stability considerations for siting and constructing a KBS-3 repository**. Based on Experiences from Äspö, HRL, AECL's URL, Tunneling and Mining. Svensk Kärnbränslehantering AB report TR-01-38.

Mauldon, M. and Ureta, J. (1996). **Stability analysis of rock wedges with multiple sliding surfaces**. Geotechnical and Geological Engineering, **14**(1): 51-66.

Nomikos, P.P., Sofianos, A.I. and Tsoutrelis, C.E. (2002). **Symmetric wedge in the roof of a tunnel excavated in an inclined stress field**. International Journal of Rock Mechanics & Mining Sciences, **39**(1): 59-67.

Palmstrom, A. and Stille, H, (2007). **Ground behaviour and rock engineering tools for underground excavations**. Tunnelling and Underground Space Technology, **22**(4): 363-376.

Panet, M. and Guenot, A. (1982). **Analysis of convergence behind the face of a tunnel**. In: *Tunnelling 82, proceedings of the 3rd international symposium, Publ. London: IMM, Brighton, June 7–11 1982, pp. 197-204.*

Pérez Hidalgo, K. and Nordlund, E. (2011). **Failure process analysis of a wedge in a drift at the Kiirunavaara mine.** In: *45th U.S. Rock Mechanics / Geomechanics Symposium, ARMA, SFO, June 26-29 2011, paper 11 -225.*

Pérez Hidalgo, K. and Nordlund, E. (2012). **Failure process analysis of spalling failure — comparison of laboratory test and numerical modelling data**. Tunnelling and Underground Space Technology, **32**: 66-77.

Pérez Hidalgo, K. and Nordlund, E. (2013a). **Comparison between stress and strain quantities of the failure-deformation process of Fennoscandian hard rocks using geological information**. Rock Mechanics and Rock Engineering, **46**(1): 41-51.

Pérez Hidalgo, K. and Nordlund, E. (2013b). **Deformation analysis in connection with bending and shear failure of a monitored stope in the Kristineberg mine in Sweden**. Accepted for publication in International Journal of Mining and Mineral Engineering.

Pérez Hidalgo, K. and Nordlund, E. (2013c). **3D numerical modelling of a wedge failure in a drift at the Kiirunavaara mine**. To be submitted to an international journal.

Press F, and Siever, R. (2001).**Understanding earth**. W.H. Freeman and Company, New York, 620 p.

Read, R. S. (1994). **Interpreting excavation – induced displacements around a tunnel in highly stressed granite**. Doctoral thesis, University of Manitoba, pp. 41-52, 25-145.

Read, R.S. (2004). **20 years of excavation response studies at AECL's underground research laboratory**. International Journal of Rock Mechanics and Mining Sciences and Geomechanical Abstracts, **41**(8): 1251-1275.

Rocscience Inc. (2007). *RocLab* Version 1.031 – Rock mass strength analysis using the Hoek-Brown failure criterion. www.rocscience.com, Toronto, Ontario, Canada.

Rocscience Inc. (2009). *Phase2* Version 1.031 – Finite Element Analysis for Excavations and Slopes. www.rocscience.com, Toronto, Ontario, Canada.

Rocscience Inc. (2013). *Dips* Version 6.0 – Graphical and Statistical Analysis of Orientation Data. www.rocscience.com, Toronto, Ontario, Canada.

Saiang, D. and Nordlund, E. (2013). **Numerical analysis of large ground deformation and rock support interaction at Kristineberg Mine, Sweden.** Technical Report, Luleå University of Technology.

Sakurai S. (1981). **Direct strain evaluation technique in construction of underground opening**. In: *The 22nd U.S. Symposium on Rock Mechanics, USRMS, Cambridge, MA, June 29-July 2 1981, Paper 81-0278.*

Sakurai, S., Kawashima, I. and Otani, T. (1993). **A criterion for assessing the stability of tunnels**. In: Ribeiro, L., Sousa, E. and Grossmann, N.F. (Eds.): ISRM International Symposium, EUROCK 1993, Balkema, Rotterdam, June 21-24 1993, Lisboa, Portugal, pp. 969-973.

Sandström, D. (2003). **Analysis of the virgin state of stress at the Kiirunavaara mine**. Licentiate thesis 2003:02, Luleå University of Technology, 159 p.

Seedsman, R. (1986). **Back-analysis of roof conditions in the Great Northern Seam, Newcastle Coal Measures, Australia, using voussoir beam theory**. International Journal of Mining and Geological Engineering, **5**(1): 15-27.

Sjöberg, J. (2005). **Rock mechanics analysis of the copper orebody**. SwedPower Report 2050700-01 (confidential).

Sjöberg, J. and Malmgren, L. (2008). **Application of global-local modelling to mining rock mechanics problems**. In: *Proc. First International FLAC/DEM Symposium on Numerical Modeling, Minneapolis, August 25-27 2008.*

Sofianos, A.I. (1986). **Stability of rock wedges in tunnel roofs**. International Journal of Rock Mechanics and Mining Sciences, **23**(2): 119-130.

Sofianos, A.I., Nomikos, P. and Tsoutrelis, C.E. (1999). **Technical Note – Stability of symmetric wedge formed in the roof of a circular tunnel: nonhydrostatic natural stress field**. International Journal of Rock Mechanics and Mining Sciences, **36**(5): 687-691.

Stacey, T.R. (1981). **A simple extension strain criterion for fracture of brittle rock**. International Journal of Rock Mechanics and Mining Sciences and Geomechanics Abstracts, **18**(6): 469-474.

Stacey, T.R. and De Jongh, C.L. (1977). **Stress fracturing around a deep-level bored tunnel**. Journal of the South African Institute of Mining and Metallurgy, **78**(5): 124-133.

Töyrä, J. (2006). **Behaviour and stability of shallow underground constructions**. Licentiate thesis 2006:76, Luleå University of Technology, 135 p.

URL: http://www.lkab.com

URL: http://www.boliden.com/

Vlachopoulos, N. and Diederichs, M.S. (2009). **Improved longitudinal displacement profiles for convergence confinement analysis of deep tunnels**. Rock Mechanics and Rock Engineering, **42**(2): 131-146.

Yun-mei, L., Yuan-zhen, H., Shu-gen, Z. and Ying, Z. (1984). **Technical Note – Failure Modes of Openings in a Steeply Bedded Rock Mass**. Rock Mechanics and Rock Engineering, **17**(2): 113-119.

Zhang, P., Yin, J.J., Nordlund, E. and Li, N. (2008). **Determination and verification of the longitudinal deformation profile in a horse-shoe shaped tunnel using two-stage excavation**. In: *5th international conference and exhibition on mass mining, Luleå, Sweden, June 9-11 2008.*

BeFo